FACHBEREICH MATHEMATIK UND NATURWISSENSCHAFTEN
FACHGRUPPE PHYSIK
BERGISCHE UNIVERSITÄT WUPPERTAL

Measurement of t-channel single top-quark production in proton-proton collisions at a center-of-mass energy of 13 TeV using the full ATLAS Run 2 dataset

Dissertation

Joshua Reidelstürz

February 2024

Erstgutachter: Prof. Dr. Wolfgang Wagner

Zweitgutachter: Prof. Dr. Ian Brock

Abgabedatum: 08.02.2024

Prüfungsdatum: 22.05.2024

Abstract

This dissertation presents the measurement of the t-channel production of single top quarks and antiquarks using the complete Run 2 dataset recorded by the ATLAS detector. The cross-section of the process is measured separately for top quark and top antiquark production. Additionally, the ratio of these cross-sections, denoted as R_t, is also determined. The methodology involves a cut-based selection, a neural network for signal separation, and a binned maximum likelihood fit. The full Run 2 dataset from the ATLAS detector encompasses an integrated luminosity of $\mathcal{L}_{\text{int}} = 140\,\text{fb}^{-1}$ from proton-proton collisions at a center-of-mass energy of $\sqrt{s} = 13\,\text{TeV}$. The total cross-sections are measured to be $\sigma(tq) = 137^{+8}_{-8}\,\text{pb}$ for top-quark production and $\sigma(\bar{t}q) = 84^{+6}_{-5}\,\text{pb}$ for top-antiquark production. The combined cross-section is determined to be $\sigma(tq + \bar{t}q) = 221^{+13}_{-13}\,\text{pb}$, and the cross-section ratio is $R_t = \sigma(tq)/\sigma(\bar{t}q) = 1.636^{+0.036}_{-0.034}$. The measured cross-sections align well with the predictions made at the next-to-next-to-leading order in quantum chromodynamics. The measured total cross-section is further used to derive a constraint on the CKM matrix element $|V_{tb}| > 0.95$ at the 95% confidence level.

Contents

Introduction

The essence of the scientific method lies in conducting experiments to test various hypotheses. In the realm of particle physics, the Standard Model (SM) stands as a robustly established theory, describing the interactions of elementary particles up to high energies. This model facilitates a plethora of predictions, rigorously tested through sophisticated experiments. A prime example of such an experimental setup is the ATLAS detector, situated at the Large Hadron Collider (LHC) at CERN. Here, protons are brought to collision at extraordinarily high energies, allowing for the exploration of intricate particle processes.

This thesis describes an analysis of data amassed during the LHC's 2015–2018 operation period, known as Run 2, comprised of proton-proton collisions, corresponding to an integrated luminosity of $140\,\text{fb}^{-1}$, at a center-of-mass energy of $13\,\text{TeV}$. The SM forecasts an array of phenomena, including specific process cross-sections occurring in these high-energy proton-proton collisions. To scrutinize these SM predictions, the data recorded by the ATLAS detector undergoes extensive analysis, each segment concentrating on different predictive aspects.

The research presented here, while examining just a fragment of these expansive predictions, is one component in constructing a comprehensive understanding of particle physics. Central to this analysis is the investigation of single top-quark production via weak charged-current interactions in the t-channel, which is the predominant single top-quark production mechanism at the LHC. This thesis details the measurements of t-channel top-quark and top-antiquark production cross-sections, and importantly, their ratio, denoted as R_t. The measurement of R_t is especially significant, as it benefits from enhanced precision owing to the cancellation of uncertainties in the ratio.

This study represents a significant advancement over previous ATLAS measurements of t-channel single top quark production, benefiting from a larger dataset that reduces statistical uncertainties, improved detector calibration, and more sophisticated theoretical predictions. The statistical analysis of the data employs a maximum likelihood fit, which effectively minimizes the impact of systematic uncertainties by refining auxiliary measurements within the selected dataset. The measurement is interpreted in terms of the strength of the Wtq vertex, placing a constraint on the absolute value of the CKM matrix element V_{tb}.

The event selection in this analysis is specifically tailored to target tq and $\bar{t}q$ events where W Bosons decay leptonically. The selection criteria include the presence of one isolated electron or muon, significant missing transverse momentum, and exactly two hadronic jets with high transverse momentum, one of which is identified as b-quark-originated. Key efforts are made to minimize the main backgrounds, namely $t\bar{t}$ and W+jets production, through cut based event selection. Special attention is given to mitigating the multijet background, which poses challenges in simulation. The single top background processes are the s-channel and tW channel production channels.

A neural network, utilizing kinematic variables as inputs, is deployed to enhance the separation of signal from background events. The output distribution of this neural network is then integrated into a binned maximum likelihood fit to ascertain the cross-sections. This analysis encompasses a comprehensive range of systematic uncertainties, including those arising from detector sources and Monte Carlo modeling, thereby ensuring a thorough and robust statistical analysis.

The first chapter provides a theoretical foundation for the dissertation, offering an overview of the SM, the simulation of proton-proton collisions, and the particle processes pertinent to this measurement. Chapter 2 details the LHC and the ATLAS detector. The production of Monte Carlo samples is outlined in Chapter 3, while Chapter 4 specifically addresses the estimation of the multijet background. Chapter 5 discusses the event reconstruction and overlap removal. Following this, Chapter 6 describes the cut-based event selection and region definition. Chapter 7 explores the further separation of events using a neural network. The uncertainties impacting the measurement are discussed in Chapter 8. Chapter 9 delves into the statistical analysis using the maximum likelihood fit and presents the results of the measurement, analyzing the influence of systematic uncertainties, correlations, and fit stability. It also examines the dependency of the results on the assumed top quark mass and interprets the total cross-section as a direct measurement of the CKM matrix element V_{tb}.

1. Theory

The Standard Model (SM) is a quantum field theory that describes the interactions of elementary particles. In the SM, these particles are characterized by quantized fields. It stands as the most successful framework in particle physics, encompassing three of the four fundamental forces: electromagnetism, weak nuclear force, and strong nuclear force, but notably, it does not include gravity. The fundamental particles of the SM are divided into fermions, which are matter particles like quarks and leptons, and gauge bosons, which are force-carrying particles like photons and gluons.

The SM was developed during the 20th century, with significant contributions [1–4] from several notable physicists such as Sheldon Glashow, Abdus Salam, and Steven Weinberg, who formulated the electroweak theory in the 1970s. The theory also integrates the strong nuclear force, as described by Quantum Chromodynamics (QCD), a framework established through the work of Murray Gell-Mann [5], George Zweig, and others in the 1960s. The integration of the electroweak and strong interactions in the 1970s and 1980s completed the SM as a comprehensive theory of particle interactions. Since then, it has been extensively tested and validated through numerous experiments and observations.

This chapter introduces the fundamental concepts of the SM. A more comprehensive account, can be found in text books such as [6–8].

1.1. Quantum field theory

Quantum field theory is the result of merging quantum mechanics and special relativity, providing a framework to describe elementary particles at high energies where relativistic effects are significant. It addresses the creation and annihilation of particles, integral to a relativistic understanding of quantum mechanics. In quantum field theory, fundamental particles are described using fields, and forces are characterized by the quantum interactions of these particles. The theory plays a crucial role in modern physics, offering a comprehensive approach to describing the behavior and interactions of the most basic constituents of the universe.

There are several approaches to formulating quantum field theory. One is the canonical quantization approach, where classical fields are promoted to operators obeying certain commutation or anti-commutation relations. Another approach is the path integral formulation, where the theory is defined in terms of path integrals of classical fields.

In the path integral formulation of quantum field theory the vacuum expectation value of time ordered products of field operators $\Phi(x)$ is given by

$$\langle 0|T\Phi(x_1)\dots\Phi(x_n)|0\rangle = \int \mathcal{D}\phi\, \phi(x_1)\dots\phi(x_n)e^{iS[\phi]/\hbar}$$

where T indicates the time-ordering of the operators before multiplication, $\mathcal{D}\phi$ represents the integration measure over all possible field configuration histories, and

$$S[\phi] = \int d^4x\, \mathcal{L}[\phi]$$

is the action. To formulate the path integral for the SM it is necessary to extend this formalism for multiple fields and introduce Grassmann variables to describe the fermion fields.

The Lagrangian $\mathcal{L}$ plays a fundamental role in the theory by encapsulating the dynamics of the fields and serving as the mathematical backbone for describing the interactions and behaviors of elementary particles within the SM.

Local and global symmetries imposed on the Lagrangian play pivotal roles in the construction of a consistent physical theory. Global symmetries ensure that the theory is invariant under transformations applied uniformly across the entire field, while local symmetries describe invariance under transformations that change with space-time. Importantly, the predictions of the theory should be Poincaré invariant. In quantum field theories this can be imposed by constructing a Lagrangian that is Poincaré invariant. This also means that the fields within it should belong to representations of the Lorentz group and transform accordingly.

The fundamental components of the SM Lagrangian are the scalar two component Higgs field, left- and right-handed Weyl spinor fields describing the fermions, and vector fields describing the gauge bosons. Fermions are classified into quarks and leptons, organized into three generations ordered by increasing mass. Each quark generation consists of an up-type and a down-type quark, while each lepton generation includes a charged lepton and a neutrino. With the exception of neutrinos, all fermions are present as left-handed and right-handed fields. The gauge bosons are responsible for the description of the forces of the theory. The elementary particles described by the SM are summarized in Figure 1.1.

1.2. Fields and Local Gauge Symmetries

Noether's theorem [10] establishes that each continuous symmetry in a physical system corresponds to a conserved quantity. In the Standard Model, the theorem explains the conservation of charges through its gauge symmetries. The SM Lagrangian possesses the combined local gauge symmetry

$$\mathrm{SU}(3) \times \mathrm{SU}(2) \times \mathrm{U}(1)$$

where SU(2) and SU(3) are the special unitary groups of degree 2 and 3 and U(1) is the unitary group of degree 1. The fields in the Lagrangian belong to representations of these three groups and transform under the gauge symmetries accordingly.

The quark fields are triplets belonging to the fundamental 3 representation of the SU(3) group, transforming with

$$\psi(x) \to e^{i\lambda^a(x)t^a}\psi(x)$$

where t^a are the eight generators of the SU(3) group in the fundamental representation. Here, $\lambda^a(x)$ are space-time dependent parameters that define the specific local transformation at point x, reflecting the local symmetry of the theory. The conserved charges of the symmetry are called color charges and the theory only including SU(3) gauge symmetry describes the strong nuclear force and is called Quantum Chromodynamics (QCD).

For each quark generation the left handed up type and down type quark form an SU(2) doublet

$$Q_L = \begin{pmatrix} u \\ d \end{pmatrix}_L$$

belonging to the fundamental 2 representation while the right handed fields are SU(2) singlets. Similarly, the left handed leptons of each generation form SU(2) doublets

$$E_L = \begin{pmatrix} \nu_e \\ e^- \end{pmatrix}_L$$

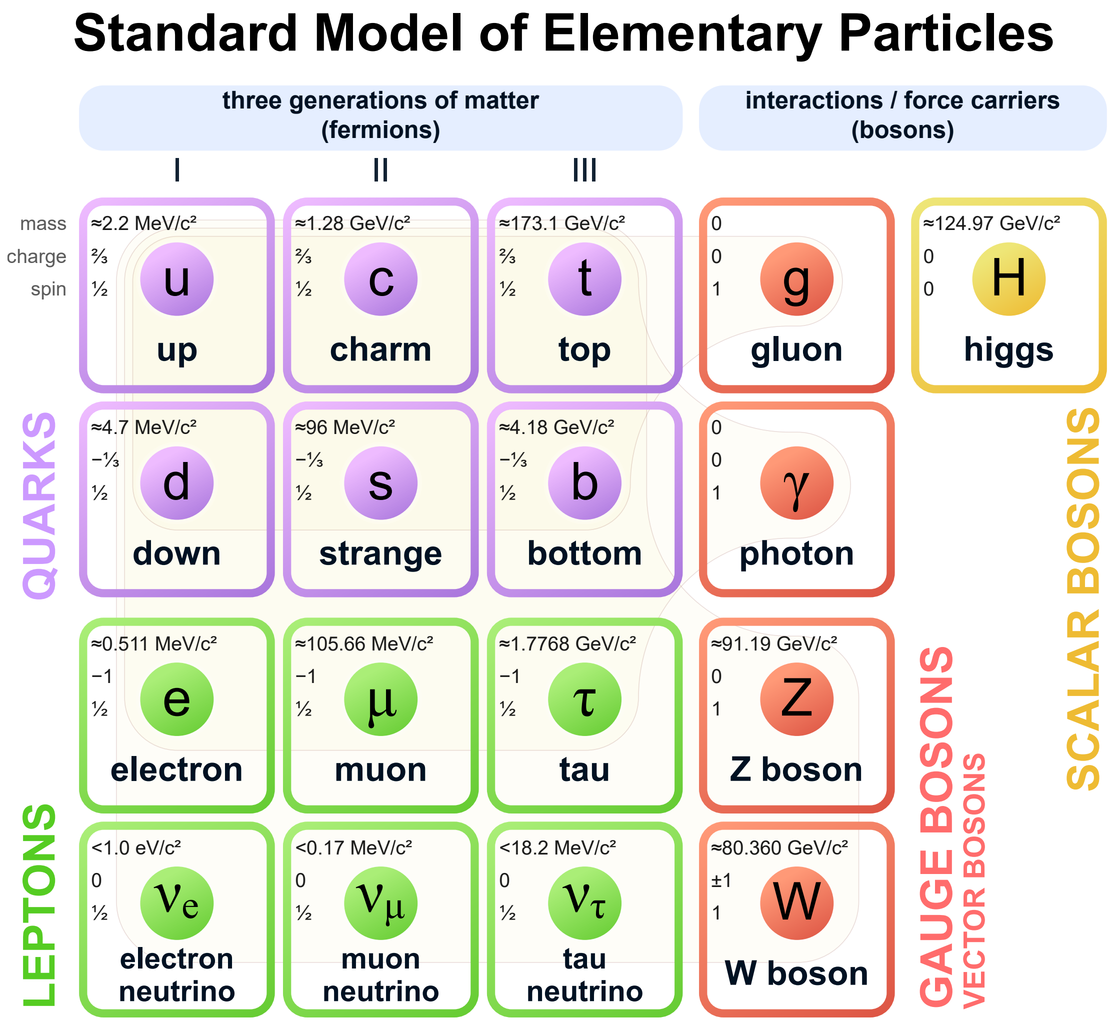

Figure 1.1.: Summary of elementary particles described by the SM [9]. The particles are divided into quarks, leptons, gauge bosons and scalar bosons by color and colored areas in the background indicate which fermions interact with which bosons.

and the right handed leptons are SU(2) singlets. The Higgs field is a doublet belonging to the 2 representation of SU(2). The SU(2) doublets transform with

$$\psi(x) \rightarrow e^{i\beta^a(x)\tau^a}\psi(x)$$

where τ^a are the three generators of the SU(2) group in the fundamental representation, and $\beta^a(x)$ are space-time dependent parameters that define the specific local transformation at point x. The conserved charge of the SU(2) symmetry is the three component weak isospin T. The transformation of the fermion fields under the U(1) group is determined by their weak hypercharge Y:

$$\psi(x) \rightarrow e^{i\alpha(x)Y}\psi(x)$$

Here, $\alpha(x)$ is the space-time dependent parameter that defines the local transformation at point x. The left handed leptons have $Y = -1$ and the right handed charged leptons have $Y = -2$. Left handed quarks have $Y = 1/3$, right handed up-type quarks have $Y = 4/3$ and right handed down-type quarks have $Y = -2/3$.

The imposed symmetries significantly restrict the allowed terms in the Lagrangian and cause all other approximate and exact global symmetries of the theory. Furthermore, the local gauge symmetry necessitates the existence of massless bosonic gauge fields, as they are needed to add derivatives of the spinor fields to the Lagrangian. The kinetic term $\bar{\psi}\gamma^\mu\partial_\mu\psi$ as expected from the Dirac equation [11] to describe the free relativistic electron field is not invariant under the local gauge transformation and can therefore not be added directly to the Lagrangian. Instead, the covariant derivative $D_\mu\psi$ is defined which transforms in the same way as the field ψ, e.g. for U(1):

$$D_\mu\psi \rightarrow e^{i\alpha(x)Y}D_\mu\psi(x)$$

To define the covariant derivatives with this transformation property a new vector field for each generator of SU(3) × SU(2) × U(1) is needed to counteract the transformation of the fields. For example for a left-handed quark field the covariant derivative is

$$D_\mu\psi = (\partial_\mu - iYB_\mu - igA^a_\mu\tau^a - igG^b_\mu t^b)\psi$$

where B_μ, A^a_μ and G^b_μ are called gauge fields transforming as

$$B_\mu \rightarrow B_\mu + \frac{1}{g_Y}\partial_\mu\alpha$$

$$A^a_\mu \to A^a_\mu + \frac{1}{g_L}\partial_\mu \beta^a + f^{abc} A^a_\mu \beta^c$$

$$G^b_\mu \to G^b_\mu + \frac{1}{g_C}\partial_\mu \lambda^a + t^{abc} G^a_\mu \lambda^c$$

where f^{abc} are the structure constants of the SU(2) group and t^{abc} are the structure constants of the SU(2) group. The definition of the covariant derivative depends on the weak hyper charge Y of the field and if the field transforms under SU(2) and SU(3).

There is one gauge vector boson field B_μ for the U(1) group, three vector fields W^a_μ with $a = 1 \ldots 3$ for SU(2) and eight vector fields G^a_μ with $b = 1 \ldots 8$ for SU(3). The kinetic terms for the fermions are then:

$$\mathcal{L}_{\text{kin}} = \bar{E}_L(i\not{D})E_L + \bar{e}_R(i\not{D})e_R + \bar{Q}_L(i\not{D})Q_L + \bar{u}_R(i\not{D})u_R + \bar{d}_R(i\not{D})d_R$$

where $\not{D}$ is short for $\gamma_\mu D^\mu$.

Kinetic terms for the gauge boson fields are constructed using the locally invariant field tensors of the gauge fields.

$$\mathcal{L}_{\text{bos}} = -\frac{1}{4}(B_{\mu\nu})^2 - \frac{1}{4}(A^a_{\mu\nu})^2 - \frac{1}{4}(G^b_{\mu\nu})^2$$

with

$$B_{\mu\nu} = \partial_\mu B_\nu - \partial_\nu B_\mu$$

$$A^a_{\mu\nu} = \partial_\mu A^a_\nu - \partial_\nu A^a_\mu - g_L f^{abc} A^b_\mu A^c_\nu$$

$$G^b_{\mu\nu} = \partial_\mu G^b_\nu - \partial_\nu G^b_\mu - g_C t^{abc} G^b_\mu G^c_\nu$$

An important aspect of the theory is the Higgs mechanism, responsible for the masses of the gauge bosons and the fermions. The Higgs field, a scalar SU(2) doublet, is introduced and a symmetric potential with a non zero minimum is added to the Lagrangian such that the Higgs field has a non zero vacuum expectation value.

$$\mathcal{L}_H = |D_\mu \phi|^2 + \frac{1}{4}\lambda(|\phi|^2 - v^2)^2$$

where λ and v are parameters determining the strength and minimum of the Higgs field potential. As a consequence, the ground state of the theory is not symmetric under the SU(2) × U(1) symmetry and the symmetry is said to be spontaneously broken. It makes sense to express the Higgs field in the Lagrangian in terms of its vacuum expectation value and its fluctuations around that value.

From now on, the unitarity gauge is used, where the vacuum expectation value is

$$\langle\phi\rangle = \frac{1}{\sqrt{2}}\begin{pmatrix}0\\ v\end{pmatrix}$$

The Higgs field can then be expressed as

$$\phi(x) = \frac{1}{\sqrt{2}}\begin{pmatrix}0\\ v+h(x)\end{pmatrix}$$

where $h(x)$ is a real valued field. Any other vacuum expectation value is physically equivalent as it can be reached by a $\mathrm{SU}(2)\times\mathrm{U}(1)$ gauge transformation of the theory. The term $|D_\mu\phi|^2$ can now be written in terms of the Higgs vacuum expectation value and of fluctuations of the Higgs field around this value:

$$\mathcal{L}_K = \frac{1}{2}\left(\partial_\mu h\right)^2 + \left[m_W^2 W^{\mu+}W_\mu^- + \frac{1}{2}m_Z^2 Z^\mu Z_\mu\right]\cdot\left(1+\frac{h}{v}\right)^2$$

where mass terms for combinations of the gauge fields arise with the $W^\pm$ bosons

$$W^\pm = \frac{1}{\sqrt{2}}(A_\mu^1 \mp A_\mu^2)$$

with mass $g\frac{v}{2}$ and the Z boson

$$Z = \frac{1}{\sqrt{g^2+g'^2}}(gA_\mu^3 - g'B_\mu)$$

with mass $\sqrt{g^2+g'^2}\frac{v}{2}$. The remaining combination

$$A_\mu = \frac{1}{\sqrt{g^2+g'^2}}(gA_\mu^3 + g'B_\mu)$$

is the electromagnetic vector potential and does not aquire a mass.

The Higgs ground state has a remaining local $\mathrm{U}(1)$ symmetry with the generator $Q = 1/2Y + \tau^3$ which is identified as the local gauge symmetry of the electromagnetic interaction. The corresponding conserved charge of the symmetry $Q = 1/2Y + T^3$ is the electric charge. The gauge theory only including the $\mathrm{U}(1)$ symmetry describes electromagnetic interactions and is called quantum electrodynamics (QED). The most general renormalizable gauge-invariant coupling terms between the fermion fields and the Higgs field are added to the Lagrangian.

$$\mathcal{L}_m = -\lambda_d^{ij}\bar{Q}_L^i\cdot\phi d_R^j - \lambda_u^{ij}\epsilon^{ab}\bar{Q}_{La}^i\phi_b^\dagger u_R^j - \lambda_\ell^{ij}\bar{E}_L^i\cdot\phi e_R^j + \text{h.c.}$$

Table 1.1.: Fermions in the SM with their corresponding weak isospin T_z, weak hypercharge Y and resulting electric charge Q. Left handed particles are given as SU(2) doublets using the mixed mass states d'^i for down type quarks. All quarks are SU(3) triplets with each component having a different color charge.

Fermions			T_z	Y	Q
$\begin{pmatrix}\nu_e\\ e\end{pmatrix}_L$	$\begin{pmatrix}\nu_\mu\\ \mu\end{pmatrix}_L$	$\begin{pmatrix}\nu_\tau\\ \tau\end{pmatrix}_L$	$+1/2$ $-1/2$	-1 -1	0 -1
e_R	μ_R	τ_R	0	-2	-1
$\begin{pmatrix}u\\ d'\end{pmatrix}_L$	$\begin{pmatrix}c\\ s'\end{pmatrix}_L$	$\begin{pmatrix}t\\ b'\end{pmatrix}_L$	$+1/2$ $-1/2$	$1/3$ $1/3$	$+2/3$ $-1/3$
u_R	c_R	t_R	0	$+4/3$	$+2/3$
d_R	s_R	b_R	0	$-2/3$	$-1/3$

where λ_d^{ij}, λ_u^{ij} and λ_ℓ^{ij} are free parameters and ϵ^{ab} is the Levi-Civita symbol. It is worth noting that this adds an interaction between the left handed and right handed fermion fields to the Lagrangian, explicitly breaking the global chiral symmetry. A coordinate transformation of the fermion fields brings these interaction terms in the form of mass terms:

$$\mathcal{L}_m = -m_d^i \bar{d}_L^i d_R^i \left(1+\frac{h}{v}\right) - m_u^i \bar{u}_L^i u_R^i \left(1+\frac{h}{v}\right) - m_\ell^i \bar{\ell}_L^i \ell_R^i \left(1+\frac{h}{v}\right) + \text{h.c.}$$

The only other part of the Lagrangian that is not invariant under this transformation is the interaction term of the $W^\pm$ boson and the quarks, where the quarks interact within their SU(2) doublets. When applying the transformation to the quark mass states here, a unitary matrix V called the Cabibbo–Kobayashi–Maskawa (CKM) [12, 13] matrix appears describing the mixing of the mass states in the interaction.

$$\mathcal{L} = \frac{1}{\sqrt{2}}\bar{u}_L^i \gamma^\mu V^{ij} d_L^j = \frac{1}{\sqrt{2}}\bar{u}_L^i \gamma^\mu d_L'^i$$

Defining $d'^i := V^{ij} d^j$ here, allows for writing down the quark SU(2) doublets in a convenient way.

An overview of all fermions and their charges is given in Table 1.1. The only constraint by the theory on the CKM matrix is its unitarity allowing to parameterize the matrix in terms of three angles and one complex phase. It is therefore necessary to measure the CKM matrix elements experimentally to determine the parameters.

Global SM fits are used to determine the most precise values of the CKM matrix by imposing SM constraints [14]:

$$|V_{\text{CKM}}| = \begin{pmatrix} 0.97435 \pm 0.00016 & 0.22500 \pm 0.00067 & 0.00369 \pm 0.00011 \\ 0.22486 \pm 0.00067 & 0.97349 \pm 0.00016 & 0.04182^{+0.00085}_{-0.00074} \\ 0.00857^{+0.00020}_{-0.00018} & 0.04110^{+0.00083}_{-0.00072} & 0.999118^{+0.000031}_{-0.000036} \end{pmatrix}$$

The larger diagonal elements of the CKM matrix suggest that quarks interacting with W bosons tend to transition to the mass state of the same generation.

1.3. Beyond the Standard Model

Despite its remarkable success, there are several observations in various fields of physics that appear to conflict with the predictions of the SM. These discrepancies strongly motivate the exploration of theories Beyond the Standard Model (BSM). One of the most significant challenges facing the SM is the enigma of dark matter and dark energy. Experimental observations, when interpreted through the lens of general relativity [15], indicate that these phenomena account for a substantial portion of the universe's mass and energy content. However, they remain unexplained within the framework of the SM. Additionally, the observed imbalance between matter and antimatter in the universe is not adequately explained by the SM.

The phenomenon of neutrino oscillations suggests that neutrinos possess mass, a feature not included in the SM, though it can be incorporated into the theory in a consistent way. Gravity is described by the theory of general relativity which is incompatible with quantum theory [16], and cannot be directly integrated into the standard model. The hierarchy problem, highlighting the vast disparity in strength between gravitational force and other fundamental forces, along with the fine-tuning issues related to the Higgs boson's mass, suggest that the SM may be part of a broader framework.

The existence of these gaps in the SM has spurred the development of various BSM theories, such as Supersymmetry, Extra Dimensions, and Grand Unified Theories, each aiming to resolve these unresolved issues. Experimental initiatives, like those conducted at the Large Hadron Collider, are crucial in testing these theories and may potentially reveal new physics that extends our current understanding as provided by the SM. These explorations could eventually lead to a theory that overcomes the SM's limitations. Consequently, making precision measurements of the SM's predictions is critical, as even minor deviations could hint at new physics.

1.4. Predictions with the Standard Model

Predicting experimental results using the SM is often not trivial. A key approach is the use of perturbation theory to make approximate predictions. For the prediction of proton-proton collisions, an important quantity is the transition amplitude of some initial state of particles to a final state of particles with definite momentum. In the asymptotic limit of infinite time for the interaction the transition of the states is described by the so called S matrix. To make predictions with the theory one wants to calculate the transition amplitude of an initial state of particles with definite momenta $|k_1 k_2\rangle_{\text{in}}$ to a final state of particles with definite momenta ${}_{\text{out}}\langle p_1 p_2 \dots|$ related by an asymptotically large time translation

$${}_{\text{out}}\langle p_1 p_2 \dots | k_1 k_2\rangle_{\text{in}} = \langle p_1 p_2 \dots |S| k_1 k_2\rangle$$

were the S matrix operator is defined, describing the transformation of the state over time, and $|k_1 k_2\rangle$ and $\langle p_1 p_2 \dots|$ are the states defined at the same time. The S matrix is further split up as $S = 1 + iT$ separating the interaction part of the transition. Finally the matrix element $\mathcal{M}$ is defined as

$$\langle p_1 p_2 \dots |iT| k_1 k_2\rangle = (2\pi)^4 \delta^{(4)} \left(\sum p_i - \sum p_f\right) \cdot i\mathcal{M}$$

externalizing the term describing the 4-momentum conservation. The matrix element encodes all the information about the interaction of the particles and as such is crucial for predicting the outcomes of particle collisions in the theory.

The matrix element can be expressed in terms of path integrals, which allows for the use of perturbative techniques, breaking down the calculation into orders of the coupling constants. These orders are composed of similar terms connected by common integration variables, making it highly convenient to represent them visually through diagrams. Initially introduced by Feynman, these graphical representations are now known as Feynman diagrams.

Higher-order diagrams involving loops suffer from divergences, which necessitate regularization through procedures like dimensional regularization, wherein the number of integration dimensions is reduced by a small amount. Once regularized, the diagrams are not divergent anymore. Subsequently, the theory must be renormalized, by redefining all free parameters of the theory, such as the coupling constants and particle masses, in a way that the predicted values of physical observables, accounting for the quantum effects of the divergent diagrams, match the observed experimental data.

After renormalization the regularization is removed while retaining the correct values of physical observables of the theory. The renormalization procedure depends on a chosen energy scale μ_{R} called renormalization scale, at which the parameters are renormalized. While the predictions of the theory do not inherently depend on μ_{R}, they exhibit a dependence when limiting calculations to a certain order in perturbation theory. Often, setting the renormalization scale equal to a characteristic energy scale of the physical process under consideration can simplify the theoretical calculations and lead to more accurate predictions, reducing the dependence of physical observables on the renormalization scale.

Of particular significance are the renormalized coupling constants and their dependence on the chosen renormalization scale. The change in

$$\alpha(\mu_r) := \frac{g^2(\mu_r)}{4\pi}$$

depending on the chosen renormalization scale is described by the renormalization group equation

$$\mu_R^2 \frac{d\alpha}{d\mu_R^2} = \beta\left(\alpha\right) = -\left(b_0\alpha^2 + b_1\alpha^3 + b_2\alpha^4 + \cdots\right)$$

where the right hand side represents an expansion in orders of α. At leading order the running of $\alpha(\mu_R)$ is then given by

$$\alpha\left(\mu_R^2\right) = \frac{\alpha\left(Q^2\right)}{1 + \alpha\left(Q^2\right) b_0 \log\frac{\mu_R^2}{Q^2}}$$

where

$$b_0 = -\frac{2n_f}{12\pi}$$

for QED and

$$b_0 = -\frac{33 - 2n_f}{12\pi}$$

for QCD. Here, n_f is the number of active quarks with masses below the energy scale. $\alpha(Q)$ acts as a reference point at which the coupling constant is determined at a certain scale Q. For the strong coupling constant the leading order formula can be written as

$$\alpha_s(\mu_r) = \frac{1}{b_0 \ln(\frac{\mu_r^2}{\Lambda^2})}$$

where Λ is the scale at which the leading order coupling diverges. Setting the renormalization scale to the momentum transfer of the process the coupling constants can be understood as a measure of the strength of the corresponding force at this scale. The electroweak coupling constant α_{EM} remains unaltered by the renormalization process at very low energies but increases as the energy scale rises, indicating the strength of the electromagnetic interaction intensifies at higher energies due to vacuum polarization effects. Measurements of the strong coupling constant at different scales can be compared with the predicted running of the constant. Figure 1.2 shows measured values of $\alpha_s(Q)$ at different scales and compares to the theory prediction.

The renormalized strong coupling constant decreases at higher scales, leading to increasingly weaker interactions between quarks and gluons, which is described as asymptotic freedom. As a result, perturbative calculations in QCD become more reliable at higher energy scales. However, at lower energies, the strong force intensifies, resulting in confinement, a phenomenon in which quarks are bound together within color-neutral hadrons, preventing their observation as isolated free particles. Hadrons can exist in two fundamental forms: three-quark states known as baryons and quark-antiquark states referred to as mesons. In addition to the valence quarks that define the quantum numbers of the hadrons, quark-antiquark pairs, known as sea quarks, and gluons, which emerge through the interaction of the valence quarks, also play an important role in the description of hadrons.

Protons and neutrons are the hadrons which form the foundational elements of atomic nuclei. Structurally, a proton is composed of two up quarks and one down quark, while a neutron consists of two down quarks and one up quark. Notably, the size of a proton is about 1 fm, which is significantly smaller than the overall scale of a hydrogen atom.

1.5. Chiral Symmetry Breaking

Due to the small mass of the u, d and s quarks the SM has an approximate chiral symmetry $\mathrm{SU}(3)_L \times \mathrm{SU}(3)_R$ of the left handed and right handed fields of these quarks [8]. This symmetry is spontaneously broken since the ground state of

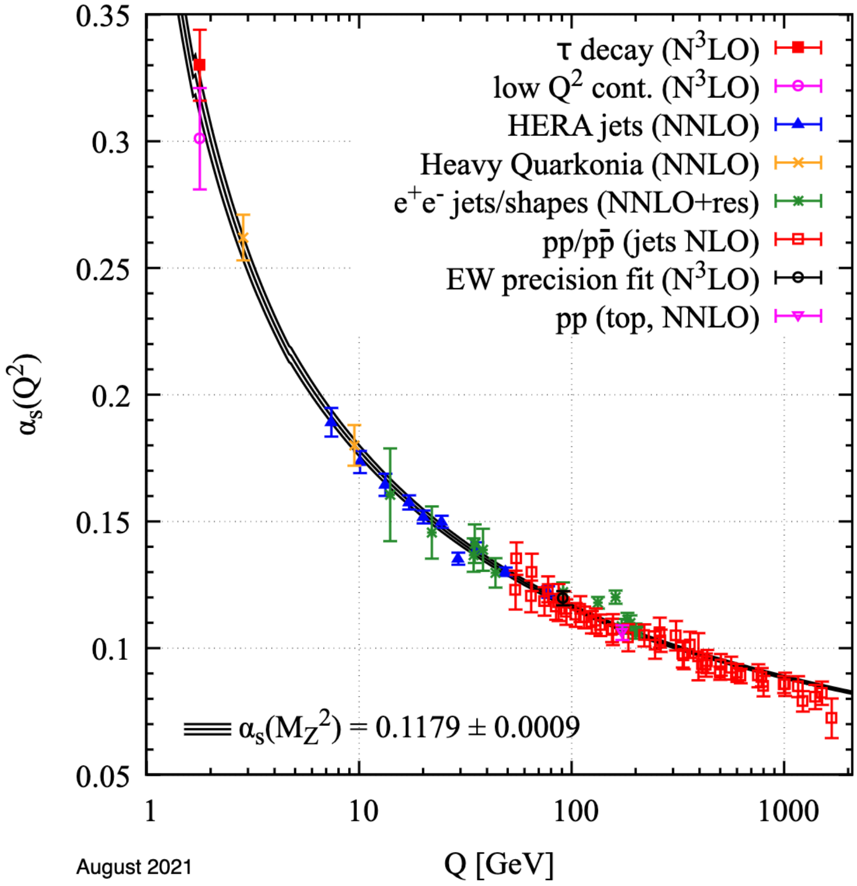

Figure 1.2.: Measured values of $\alpha_s(Q)$ at different scales compared to the theory prediction of the running of the constant [17].

QCD at low energy scales is a quark gluon condensate with

$$\langle 0|\bar{Q}Q|0\rangle \neq 0$$

The ground state is only invariant for identical transformations of left and right handed fields breaking the chiral symmetry, leaving an approximate SU(3) symmetry. This causes the light quarks to obtain big effective masses at low energies and is the main source of the mass of the hadrons. According to the Goldstone theorem, the eight spontaneously broken continuous symmetries generate eight massless particles which are certain meson types called the pions and kaons. Since the initial symmetry was only approximate due to the non zero light quark masses, the pions and kaons are not massless but have smaller masses then the other hadrons, where the kaons are heavier as they contain the heavier strange quark.

1.6. Measurements of the Standard Model

After the formulation of the SM, many of its key predictions remained untested experimentally. The theory predicted the existence of W and Z gauge bosons [18], mediating the weak force. These were subsequently searched for in the UA1 and UA2 experiments at CERN and were eventually discovered in 1983 [19, 20]. The top quark, predicted as the $\mathrm{SU}(2)$ doublet partner of the bottom quark discovered in 1977 at Fermilab [21], was found in 1994 at the Tevatron [22, 23]. Perhaps the most extraordinary prediction was that of the Higgs boson [24–26]. The theory's reliance on gauge symmetries meant that the only conceivable method to generate masses for the elementary particles was via the Higgs mechanism. The anticipated existence of the Higgs lead to the design of experiments capable of searching for the Higgs particle across higher mass ranges. The discovery of the Higgs particle in 2012 by ATLAS and CMS [27, 28] marked the identification of all the particles in the SM. However, the theory has made many more predictions, which have been measured in a variety of experiments since then.

The SM depends on several parameters that are not inherently predicted by the theory but must be determined through experimental measurements. These include the four parameters of the CKM matrix, the coupling constants of the theory, the parameters v and m_H of the Higgs field, the masses of the charged leptons and quarks, and the CP-violating phase θ_{CP} in QCD. Precise measurement of these parameters is accomplished through various analyses conducted at different experiments, with ongoing efforts focused on enhancing the accuracy of these measurements.

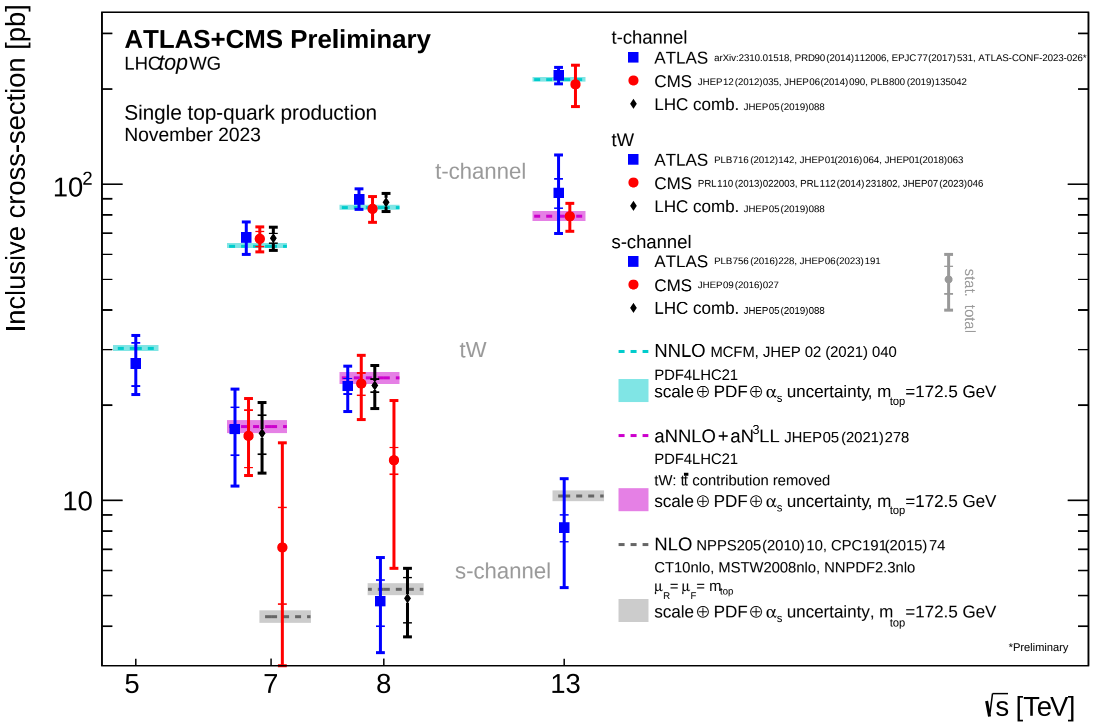

Figure 1.3.: Summary of ATLAS and CMS measurements of the single top-quark production cross-sections in various channels as a function of the center of mass energy and compared to theory prediction. A preliminary result of this analysis is included in the plot [29].

In the context of the measurement discussed in this thesis, the parameters that describe the CKM matrix are particularly significant. This is because one of the elements of the CKM matrix, $|V_{tb}|$, can be directly measured by interpretation of the t-channel cross-section measurement. Another class of analyses focuses on the measurement of cross-sections of different SM processes. The cross-section of a process depends on the collision energy and as such the cross-section predicted by the SM can be probed at different energies. The highest energy reached at the LHC are first analyses completed at 13.6 TeV. Analyses measuring single top-quark production cross-sections at different center of mass energies are shown in Figure 1.3.

Single top quark production via the t-channel was first observed at the Tevatron [30, 31] at 1.96 TeV. The t-channel single top-quark production cross-section was measured in various analyses at 5, 7, 8 and 13 TeV at ATLAS and CMS.

At 5 TeV ATLAS measures the cross-sections

$$\sigma(tq) = 19.8^{+3.9}_{-3.1}(\text{stat.})^{+2.9}_{-2.2}(\text{syst.})\,\text{pb},\;\; \sigma(\bar{t}q) = 7.3^{+3.2}_{-2.1}(\text{stat.})^{+2.8}_{-1.5}(\text{syst.})\,\text{pb},$$

and

$$\sigma(tq+\bar{t}q) = 27.1^{+4.4}_{-4.1}(\text{stat.})^{+4.4}_{-3.7}(\text{syst.})\,\text{pb},\;\; R_t = 2.73^{+1.43}_{-0.82}(\text{stat.})^{+1.01}_{-0.29}(\text{syst.})$$

using an integrated luminosity of 255 pb^{-1}[32].

At 7 TeV ATLAS measured the cross-sections

$$\sigma(tq) = 46 \pm 6\,\text{pb},\;\; \sigma(\bar{t}q) = 23 \pm 4\,\text{pb},$$

and

$$\sigma(tq+\bar{t}q) = 68 \pm 8\,\text{pb},\;\; R_t = 2.04 \pm 0.18$$

using 4.59 fb^{-1} [33] and CMS measured the cross-section

$$\sigma(tq+\bar{t}q) = 67.2 \pm 6.1\,\text{pb}$$

combining data with muon and electron final states with integrated luminosity of 1.17 fb^{-1} and 1.56 fb^{-1} respectively[34].

At 8 TeV ATLAS measured the cross-sections

$$\sigma(tq) = 56.7^{+4.3}_{-3.8}\,\text{pb},\;\; \sigma(\bar{t}q) = 32.9^{+3.0}_{-2.7}\,\text{pb}$$

and

$$R_t = 1.72 \pm 0.09$$

using an integrated luminosity of 4.59 fb^{-1} [35] and CMS measures the cross-sections

$$\sigma(tq) = 53.8 \pm 1.5(\text{stat.}) \pm 4.4(\text{syst.})\,\text{pb},\;\; \sigma(\bar{t}q) = 27.6 \pm 1.3(\text{stat.}) \pm 3.7(\text{syst.})\,\text{pb},$$

and

$$\sigma(tq+\bar{t}q) = 83.6 \pm 2.3(\text{stat.}) \pm 7.4(\text{syst.})\,\text{pb},\;\; R_t = 1.95 \pm 0.10(\text{stat.}) \pm 0.19(\text{syst.})$$

using an integrated luminosity of 19.7 fb^{-1} [36].

Additionally, analyses at 13 TeV using partial Run 2 datasets have been carried out by ATLAS measuring

$$\sigma(tq) = 156 \pm 5(\text{stat.}) \pm 27(\text{syst.}) \pm 3(\text{lumi.})\,\text{pb},$$

$$\sigma(\bar{t}q) = 91 \pm 4(\text{stat.}) \pm 18(\text{syst.}) \pm 2(\text{lumi.})\,\text{pb}$$

and

$$R_t = 1.72 \pm 0.09(\text{stat.}) \pm 0.18(\text{syst.})$$

using an integrated luminosity of 3.2 fb^{-1} [37] and by CMS measuring

$$\sigma(tq) = 130 \pm 1(\text{stat.}) \pm 19(\text{syst.})\,\text{pb}, \quad \sigma(\bar{t}q) = 77 \pm 1(\text{stat.}) \pm 12(\text{syst.})\,\text{pb}$$

and

$$R_t = 1.68 \pm 0.02(\text{stat.}) \pm 0.05(\text{syst.}),$$

using 35.9 fb^{-1} [38].

Previous measurements of R_t are summarized in Figure 1.4. All previous measurements of the t-channel single top-quark production found agreement with the SM predictions.

1.7. Factorization of Hadronic Cross-Sections

In proton-proton collisions, the previously described perturbation theory of QCD alone is insufficient to make predictions due to the phenomenon of confinement, preventing the direct use of the perturbation theory to describe the proton state itself.

To address this, the first-order parton model, initially proposed by Feynman, factorizes the calculation of cross-sections into two components: the proton's description through parton distribution functions (PDFs) and the calculation of the matrix element describing the interaction from an initial parton state to a final state of partons called the hard scattering.

$$\sigma = \sum_{ij} \int dx_1 dx_2\, f_i(x_1)\, f_j(x_2)\, \hat{\sigma}_{ij}(x_1 p, x_2 p)$$

where $f_i(x_1)$ and $f_j(x_2)$ are the leading order PDFs giving the probability of finding a parton i with momentum fraction x_1 in one proton and a parton j with momentum fraction x_2 in the other proton, respectively, and $\hat{\sigma}_{ij}(x_1 p, x_2 p)$ is the short-distance cross-section, describing only the transition from the initial state of partons i and j to the final state.

This simple picture needs to be modified when going to higher orders. At higher orders the short distance cross-section would naturally include terms with quark or gluon splittings in the initial state. These terms however have singularities when the splittings are collinear. It is possible to redefine the cross-sections and PDFs such that these collinear singularities are included in the PDF.

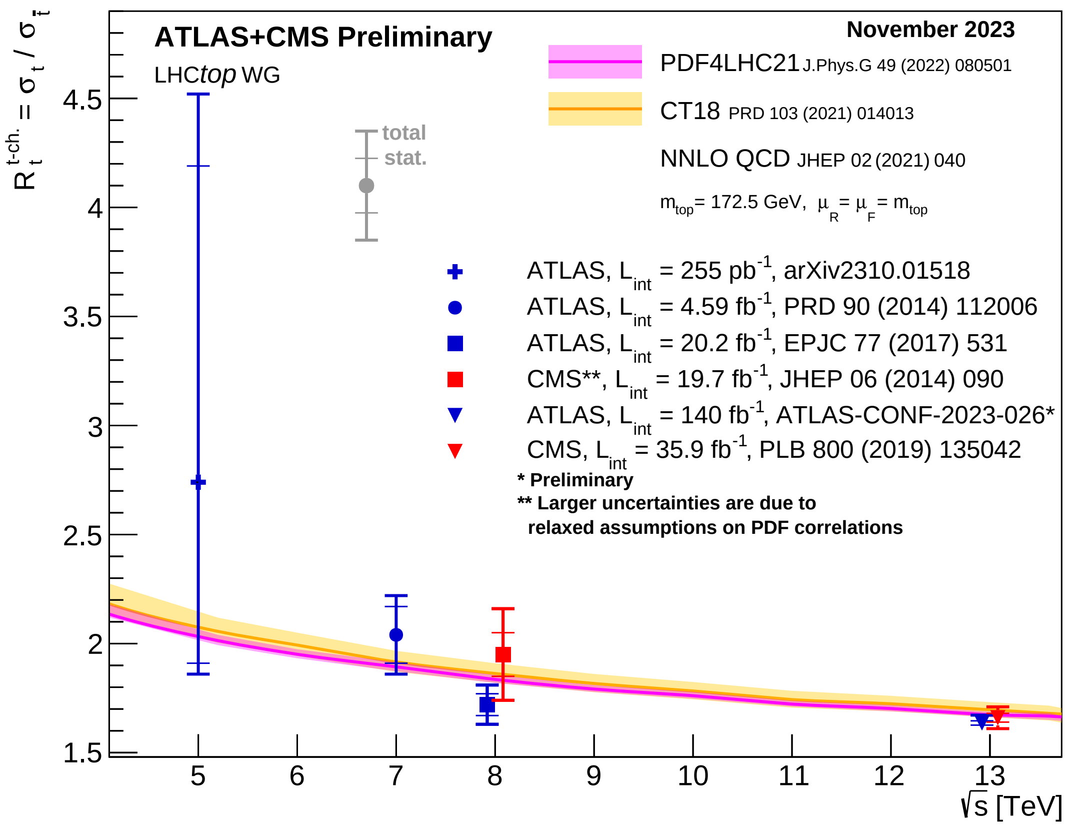

Figure 1.4.: Summary of ATLAS and CMS measurements of R_t measurements as a function of the center of mass energy and compared to theory prediction. A preliminary result of this analysis is included in the plot [29].

In this case the definition of the PDFs is determined by a chosen factorization scheme. Most commonly chosen is the modified minimal subtraction or $\overline{\text{MS}}$ scheme.

Additionally, a factorization scale μ_{F} is introduced which in some way depending of the chosen factorization scheme determines at what scale the PDF is probed. Since part of the partonic cross-sections is refactored into the PDF, also the partonic cross-section now depends on this factorization scheme and scale. Similarly to the factorization of long distance interactions in the initial state, also the hadronic final states can feature long distance interactions which need to be removed from the partonic cross-section. In this case, they are factored into fragmentation functions. Both PDFs and fragmentation functions are not directly calculable from QCD but need to be measured in data. However, the dependence on the factorization scale can be determined.

The PDFs of the proton are determined through a combination of experimental data, theoretical calculations, and global fits, where various measurements from high-energy scattering experiments are analyzed. Different sets of PDFs are available, created by different collaborations and groups, each with their specific methodology for analyzing the experimental data and incorporating theoretical calculations. These PDF sets come with uncertainties to account for the limitations in the knowledge of the proton's internal structure. In Figure 1.5 the NNPDF3.1 NNLO PDF [39] of different partons evaluated at $\mu^2{=}10\,\text{GeV}^2$ and $\mu^2{=}10^4\,\text{GeV}^2$ are shown. The figure illustrates that valence quarks are more commonly found at higher momentum fractions, and at higher center-of-mass energies, sea quarks and gluons are increasingly likely to participate in interactions.

1.8. Event Generation

The Monte Carlo (MC) method is fundamental for predictions in proton-proton collisions at the LHC. Instead of determining the analytical form of the probability distribution of events in phase space, which is typically not possible, simulated events are generated which follow the probability distribution. This approach enables the use of probabilistic models for the event generation and the simulation of the detector response on an per-event basis.

Processes relevant to the analysis can be defined by their hard scattering final state $X + k$, where X stands for the final state particles identifying the process and k for a number of additional final state particles. The processes relevant to this analysis are described in detail in Sections 1.15 to 1.17. Processes with different

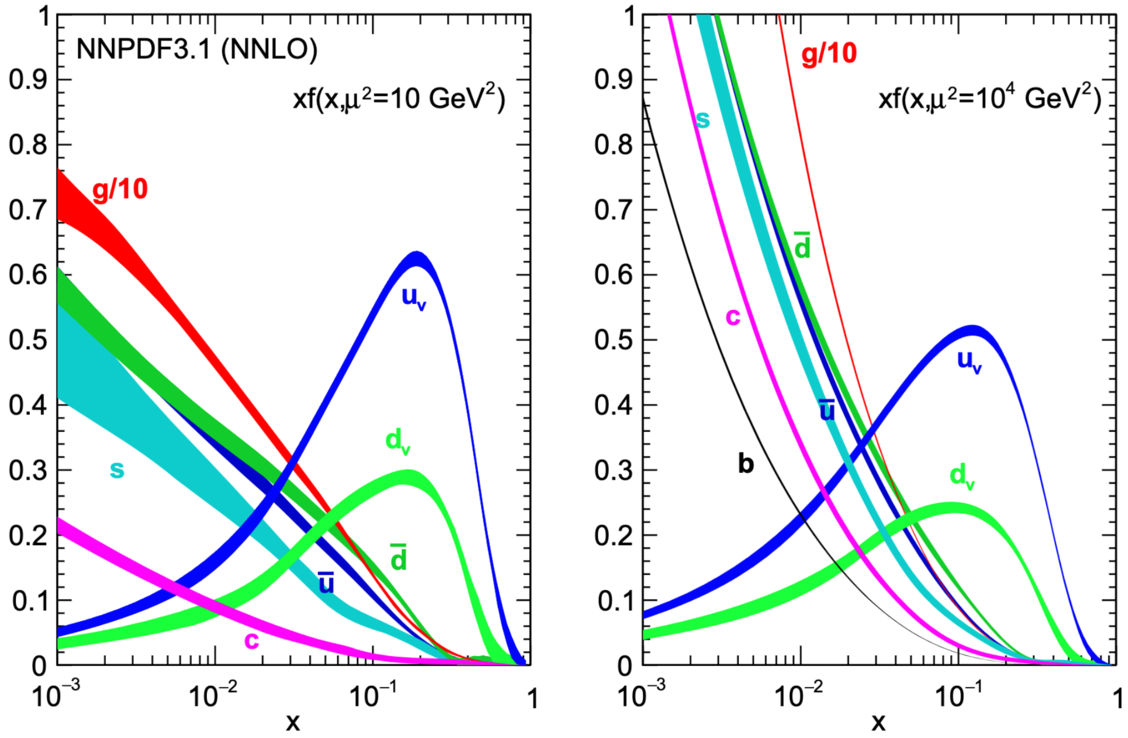

Figure 1.5.: The NNPDF3.1 NNLO PDF evaluated at $\mu^2{=}10\,\mathrm{GeV}^2$(left) and $\mu^2{=}10^4\,\mathrm{GeV}^2$(right) [39].

final states do not interfere with each other and as such their cross-section can be calculated separately and added at a later stage of the analysis to get the combined theory prediction.

The order of perturbation of the calculation determines the inclusion of higher order Feynman diagrams and additional radiations in a process's computation. At next-to-leading order (NLO) for the strong coupling constant, the process for the final state X involves the matrix element $\mathcal{M}_X$, which includes diagrams with at most one loop, and the matrix element $\mathcal{M}_{X+1}$, which includes one additional final state particle but no loops. At the next-to-next-to-leading order (NNLO), the total sum of loops and additional radiations is limited to two.

The differential hard scattering cross-section of a process with the final state $X + k$ can be related to the corresponding matrix element by

$$\frac{\mathrm{d}\hat{\sigma}}{\mathrm{d}\Phi_{X+k}} \approx \frac{|\mathcal{M}_{X+k}|^2}{2\hat{s}}$$

where $\hat{s} = (p_1 + p_2)^2$ is the square of the invariant mass of the initial state particles and assuming small masses of the initial state particles compared to $\hat{s}$. The total cross-section of the process with final state X can be written as

$$\hat{\sigma}_X = \sum_{k=0}^{N} \int \mathrm{d}\Phi_{X+k} \frac{|\mathcal{M}_{X+k}|^2}{2\hat{s}}$$

where N is the perturbation order. Due to the high dimensionality of the phase space it is usually most practical to evaluate the integral using MC integration techniques.

To simulate events for a process, random points within the allowed phase space are selected, and a weight is calculated for each. This weight is proportional to the product of the PDFs, the infinitesimal phase space volume $\mathrm{d}\Phi_{X+k}$, the factor $\frac{1}{2\hat{s}}$, and the squared matrix element $|\mathcal{M}_{X+k}|^2$. Importantly, the phase space variables are often transformed to a set that more effectively probes peaks in the differential cross-section. This transformation introduces a Jacobian determinant as an additional factor in the weight calculation. Each phase space point is accepted as an event with a probability that equals the ratio of its weight to the maximum possible weight. The events generated by this method are distributed according to the differential cross-section in phase space.

Several programs are available for automating the calculation of the matrix element in next-to-leading order (NLO), the simulation of hard scattering events and further steps in the simulation. Figure 1.6 shows an overview of the complete event generation as done in PYTHIA [40]. The following sections give an overview of the event generation beyond the hard scattering cross-section.

1.9. Parton Shower Simulation

Due to the limitations in perturbation order, the matrix element describes the collision process only well at the high energy scale of the hard scattering. To generate a simulated detector response the matrix element calculation has to be evolved down to an energy scale of around 1 GeV where hadronization, the formation of color neutral hadrons takes place.

This energy scale evolution is approximated at leading logarithmic order by shower algorithms implemented in programs such as PYTHIA, HERWIG or SHERPA not by first principle but using phenomenological models. Such parton shower algorithms take the initial and final state particles generated by the matrix element event generator as input and, in a first step, add radiations to the process.

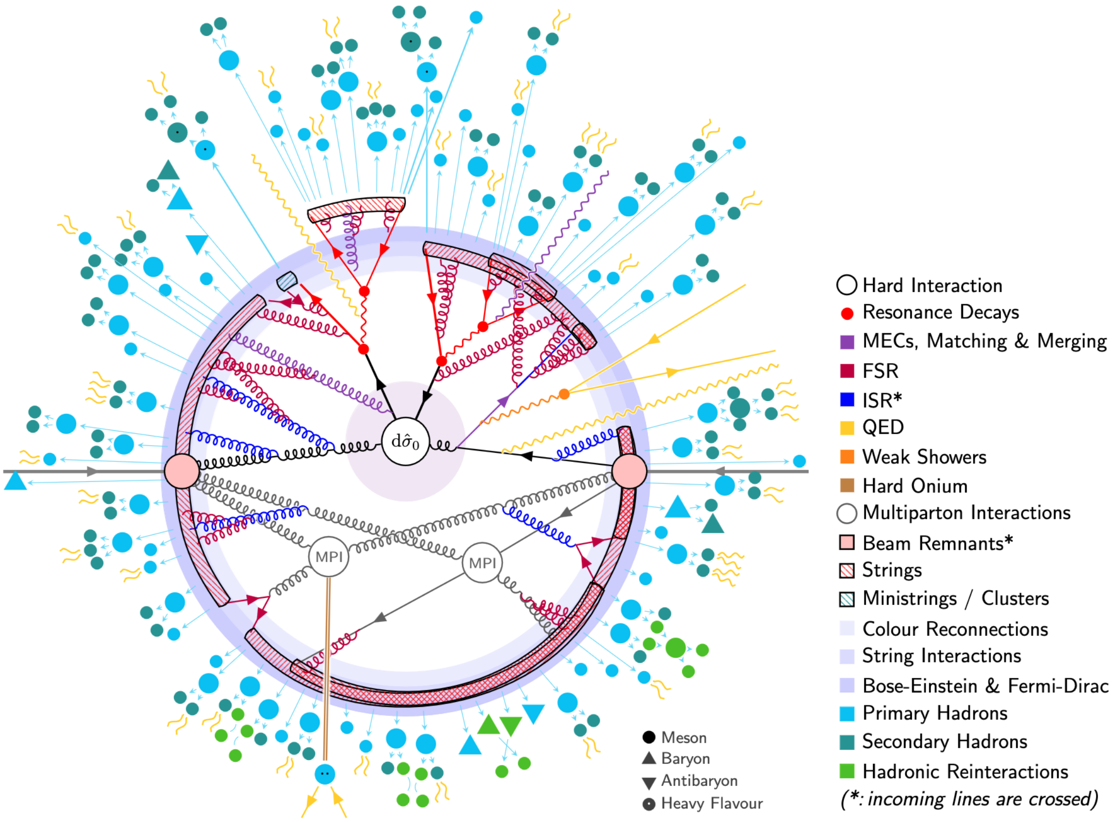

Figure 1.6.: Illustration of the entire simulated event in Pythia [40].

Shower algorithms work by considering different branching processes such as $q \to qg$ or $g \to q\bar{q}$ and calculating branching rates for each process depending on the energy distribution between the two particles produced in the branching. The algorithm evolves the event in an ordering variable defined in terms of the properties of the partons. Different definitions of the ordering variable are possible. While in Pythia the p_{T} of the partons is used in Herwig the opening angle between produced particles in the branching is used to reduce interference effects. The final state partons are evolved down in this ordering variable from the hard scattering scale to the hadronization scale until a branching takes place. Then, the produced particles in the branching are evolved further down in scale and so on.

A different parton shower is applied to simulate radiation in the initial state. The effects of initial state radiation on the initial state particles is already described by the evolved PDFs. The initial state parton shower is used to simulate the boost and rotation of the hard scattering system coming from the initial state radiation as well as the production of additional final state particles through radiation. The shower is evolved starting from the initial state partons of the hard scattering and evolved down in an ordering variable, but going backwards: When a branching occurs the considered parton is one of the two branching products and what is added is the parent particle with increased momentum fraction and the other produced particle of the branching process. This other particle usually does not further radiate. While gluon emissions play the biggest role in the parton shower also photon emissions and other relevant processes are included as branching processes.

At NLO, the matrix element encompasses Feynman diagrams with an additional final state particle, causing an overlap with parton shower simulations of leading-order diagrams, leading to double-counting. This overlap can be rectified using a matching procedure, for which multiple methodologies exist, each offering distinct advantages and challenges [41].

1.10. Hadronization Models

After the parton momenta drop below an energy of around 1 GeV the strong interaction starts to get non-pertubative and the production of color neutral hadrons takes place. As for the parton shower, this process is described using phenomenological models. The model implemented in Pythia is a type of Lund string fragmentation model. The model is based on the physical idea that color charged partons are connected by a string of self interacting gluons causing a linear increase in energy with increasing distance between the partons. Quarks are the endpoints of strings while gluons are intermediate points in the strings. At sufficient energy, the string breaks producing a quark pair and thus splitting the string into two strings. In the model, breaks in the strings are considered by iterating over the strings in steps. Finally, the hadrons are build combining quarks with antiquarks from adjacent breaks. The production of baryons can be simulated by allowing quark antiquark production in the strings via vacuum fluctuations.

An alternative approach is the cluster model [42] as implemented in Herwig and Sherpa. This approach is based on the fact that the particles produced by the shower algorithm can be grouped into clusters of color singlets. As a first step glouns are forced to decay into quark-antiquark pairs. This enables the grouping of the partons into color neutral clusters consisting of two quarks each. These clusters are then decayed randomly in one of the allowed two-body decay channels, assuming a probability proportional to the available phase space of the channel.

1.11. The Underlying Event and Pileup

In each colliding proton, one parton acts as the initial parton of the initial-state parton shower leading to the hard scattering. This leaves behind remnants of the protons. When the shower initiator carries a color charge, the proton remnants are also color-charged, and need to be considered in the simulation of the hadronization. The interaction of the remnants from colliding protons in a hard scattering event is often termed the underlying event. To simulate the underlying event, algorithms model the remnants of the proton, and the parameters of these algorithms are tuned to match experimental data. The interactions of these remnants can significantly impact the final state observables in the detectors.

Since each bunch contains many protons, multiple interactions, known as pileup, often occur among other protons in the detector during the same or neighboring bunch crossings. Pileup is estimated using minimum bias events, which are a very loose selection of inelastic events. The vast majority of minimum bias events are strong interaction processes that produce particles with low transverse momentum.

1.12. Decays and Detector Simulation

The hadrons produced in the event are usually unstable and decay into more stable hadrons before they reach the detector. The decays can be simulated directly by the main general purpose generators HERWIG, SHERPA and PYTHIA. In ATLAS, HERWIG and PYTHIA are commonly interfaced with EVTGEN [43] to handle bottom and charm hadron decays.

The response of the particles in the ATLAS detector is simulated using GEANT4 [44, 45]. A detailed model of the detector geometry is used to simulate both the interaction of the particles with the detector material and the response measured with the detector to the event. Alternatively, a much faster simulation, Atlfast-II [44], can be used, where the inner detector and the muon system are simulated with GEANT4 while the calorimeter response is determined by a parameterized simulation.

1.13. Top Quark

The top quark, the heaviest of all quarks in the SM, has an extremely short lifespan that prevents it from forming bound states with other quarks before decaying. This characteristic allows for more direct and precise measurements of the top quark's properties. In the SM, the primary production mechanism for top quarks is the pair production of top quarks, mediated by strong interactions. In contrast, single top quark production is a process of the weak interaction.

The top quark was first predicted in the 1970s by Kobayashi and Maskawa [13] as the weak isospin partner of the bottom quark. Its discovery in 1995 at the Tevatron colliders CDF and D0 at Fermilab [22, 23] based on the strong top quark-antiquark pair production, was a significant confirmation of the SM's validity. Since then, extensive studies of the top quark's properties have been conducted at various particle colliders, including the LHC at CERN, contributing to the precise determination of its mass, couplings, and production cross-sections, which further validate the predictions of the Standard Model. These measurements also provide constraints on new physics beyond the Standard Model giving the top quark an important role in exploring new frontiers of particle physics. The mass of the top quark is measured to be $172.69 \pm 0.30\,\mathrm{GeV}$ [14]. The top quark pair production cross-section is not particularly sensitive to $|V_{tb}|$ due to the production being mediated by the strong force where $|V_{tb}|$ plays no role. In single top production however, the top quark is produced directly via the Wtb vertex enabling a direct measurement of $|V_{tb}|$.

The initial state in top quark pair production can involve either two gluons or a quark-antiquark pair. Figure 1.7 presents the leading order Feynman diagrams for these processes. At a center of mass energy of 13 TeV, the cross-section for top quark pair production is predominantly governed by gluon fusion, depicted in Figures 1.7a and 1.7b.

1.14. Top Quark Decay

In relation to the other quarks, the top quark has not only an extraordinarily high mass but, consequently, also an exceptionally short lifetime of roughly $5 \times 10^{-25}\,\mathrm{s}$ [46]. Since hadronization takes place at time scales around $3 \times 10^{-24}\,\mathrm{s}$ [46] the top quark decays before it can form bound states with other quarks. This prevents the spin of the top quark to be influenced by hadronization. Moreover, a change of spin state through gluon emission takes place on much larger time

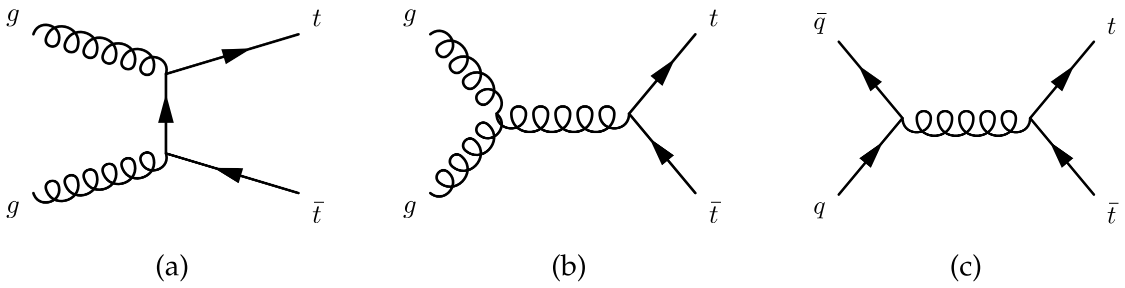

Figure 1.7.: Leading order Feynman diagrams of top-quark-antiquark pair production via gluon fusion in 1.7a and 1.7b and via quark antiquark annihilation in 1.7c.

scales than the top quark decay [46]. Because of this, if the top quark is produced in a polarized state it will stay in its spin state until it decays and convey its spin to its decay products.

Predominantly, the top quark decays into a bottom quark and a W boson, possible because the top quark mass is bigger than the combined mass of the W boson and bottom quark. While decays into a down or strange quark and a W boson are theoretically possible, these are exceedingly rare events due to the much smaller associated CKM matrix elements.

In the decay of the top quark, the resulting W boson can decay through two channels: the hadronic channel, leading to quark production, and the leptonic channel, resulting in the production of leptons. For this analysis, focus is placed exclusively on the leptonic decay channel, as the hadronic channel is obscured by a large background of hadronic strong interaction processes.

The Feynman diagrams depicting the top quark decay at leading order are shown in Figure 1.8.

The branching ratios of the W boson's decay modes, as predicted by the SM, are unequal: including final-state QED and QCD corrections the hadronic decay is expected to occur 67.5 % of the time, whereas the leptonic decay is predicted to happen at a rate of 32.5 % [14]. In the leptonic decay channel, the direction of the emitted lepton shows a strong correlation with the spin of the top quark. This correlation is not only instrumental in studying the polarization of the top quark but also beneficial in distinguishing its decays from various background processes.

The decay width Γ of a particle describes its probability of decay and is inversely proportional to its lifetime $\tau = 1/\Gamma$. This parameter is crucial in determining the range of energies over which the particle can decay.

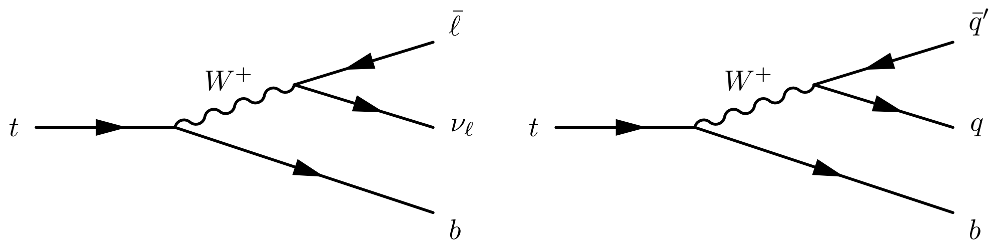

(a) (b)

Figure 1.8.: Leading order Feynman diagrams of top quark decay. The left diagram shows the decay into a bottom quark and leptons and the right diagram the decay into a bottom quark and two additional quarks.

In the context of top quark decay, the Narrow Width Approximation (NWA) is particularly relevant, as the top quark's decay width Γ is considerably smaller than its mass [47]. The NWA simplifies calculations by considering only amplitude contributions where the top quark is in its intermediate resonant state, due to their greater contribution to the overall cross-section. This allows for a focus on the dominant amplitude parts where the top quark is in its 'on-shell' state, satisfying the relation:

$$p^\mu p_\mu = m_t^2.$$

In practical terms, the NWA facilitates the separate calculation of top quark production and decay and allows for the factorization of the total cross section:

$$\sigma = \sigma_{\text{prod}} \cdot \mathcal{B},$$

where σ_{prod} is the production cross-section and $\mathcal{B}$ is the branching ratio for a particular decay.

1.15. Single Top-Quark Production

Single top-quark production is classified into three types: t-channel, s-channel, and tW channel production. In t-channel production, denoted by its LO final states tq and $\bar{t}q$, a light quark interacts weakly with a bottom quark, producing the top quark and a light quark. In the s-channel, denoted by its final states $t\bar{b}$ and $\bar{t}b$, the top quark is produced together with a bottom quark. Finally, in the tW channel, the top quark is produced alongside a W boson.

The signal process of this analysis is the t-channel production, which is the single top-quark production process with the biggest cross-section at the LHC.

Special care has to be taken when considering the *t*-channel Feynman diagrams shown in Figure 1.9a and 1.9b. The diagram in Figure 1.9a includes a bottom quark in the initial state. This is possible using the five flavor scheme where the initial state bottom quark is described by the PDF. Adding the diagram in Figure 1.9b to this is double counting when the bottom quark pair is nearly collinear [48]. This necessitates the implementation of a matching procedure. In this analysis, the *t*-channel production events are instead simulated using the four flavor scheme where the PDF does not include bottom quarks. Therefore, the diagram in Figure 1.9a is not included, avoiding the double counting issue.

The leading order tq production diagrams in the four flavor scheme are shown in Figure 1.9b and 1.9c. While the diagram in 1.9c only corresponds to a small cross-section, there is a destructive interference between the two diagrams [49]. At higher orders the contribution of the diagram in Figure 1.9a is automatically restored as the description of the bottom quark production in the matrix element becomes more accurate [49].

The additional bottom quark not produced in the top quark decay tends to have relatively high rapidity and low momentum making it difficult to identify and reconstruct in the later analysis.

The cross-sections of the single top quark production processes are affected differently by the center of mass energy. Higher center of mass energies increase the chance of gluon splitting in the initial state which favors *t*-channel production. Additionally, the *t*-channel phase space increases with higher energies further increasing the cross-section. The *s*-channel phase space on the other hand is less dependent on the center of mass energy, and the cross-section mostly increases due to the probing of smaller proton momentum fractions at higher center of mass energies [49]. At the center of mass energies at the LHC the *s*-channel process becomes very small relative to the *t*-channel.

The tW production is very small at low energies but increases rapidly and overtakes the s-channel process at high energies such as at the LHC. While the tq process increases rapidly at higher energies the $t\bar{t}$ background process increases even faster making a measurement of tq at higher energies not intrinsically more precise.

One characteristic property of the tq process is the kinematics of the light jet produced in the W interaction. This jet is produced preferably in the forward direction and tends to higher values of rapidity for increased center of mass energy. At 13 TeV the peak in the $|\eta|$ distribution is at around $|\eta| = 2.5$ [49]. While the reconstruction of such a forward jet can be more difficult, this feature

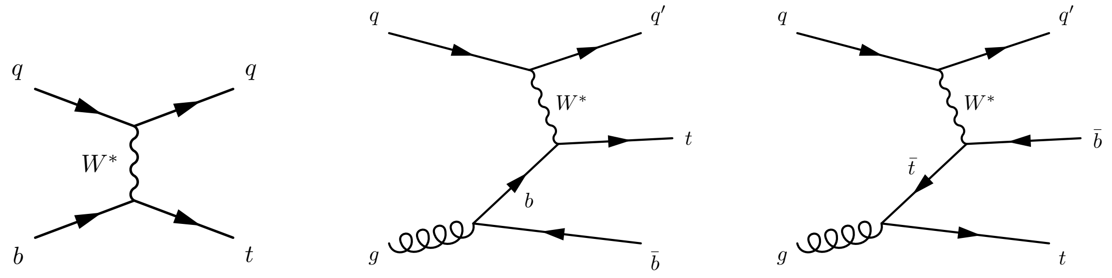

(a) (b) (c)

Figure 1.9.: Feynman diagrams of t-channel top-quark production with a bottom quark in the initial state in Figure 1.9a and a gluon in Figures 1.9b and 1.9c

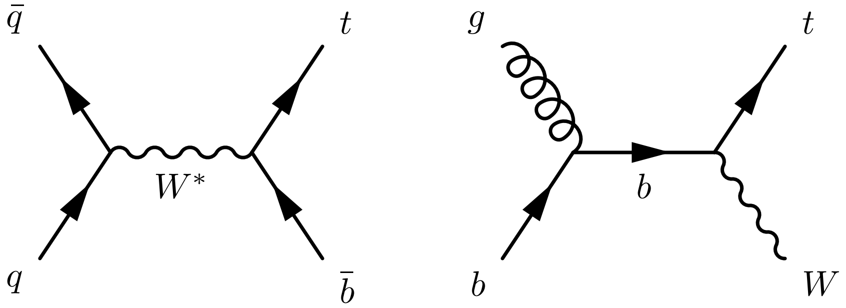

(a) (b)

Figure 1.10.: Leading order Feynman diagrams of top-quark production in the s-channel (1.10a) and tW-channel (1.10b) production

can also be used to separate the signal from the background processes in the analysis.

Single top quarks are produced with nearly 100 % polarization, due to the weak interaction only coupling to left handed particles and right handed antiparticles. The most polarization-sensitive angle is between the charged lepton from top decay and the direction of the spectator jet, in the top quark rest frame [48].

In s-channel top-quark production two quarks interact producing a top quark and a bottom antiquark. At LO the process is therefore differentiated from the t-channel process by its final state. Also at NLO there is no interference between the t-channel and s-channel process due to different color states of the final state quarks [48].

In the tW process, the top quark is produced together with an additional

W-boson. There is no interference between the tW process and the other single top-quark processes at NLO. However, there is an overlap of the tW process and the $t\bar{t}$ process at NLO, where identical Feynman diagrams are included for both processes. One way to solve this problem is to combine both processes into one process taking into account all interference. Another less precise solution, which is employed here, is to implement a method attempting to remove the overlap of the two processes from the tW process.

1.16. W+jets Background Process

An essential background process for the analysis is the W+jets process. Although this process does not involve a top quark, it directly produces a W boson, thereby potentially generating signal signatures similar to those of the signal process.

Exemplary leading-order Feynman diagrams of the W+jets process are presented in Figure 1.11. The most substantial contribution from the W+jets background arises from events where a bottom quark pair appears in the final state, as depicted in 1.11b. If one of the jets originating from the bottom quarks is not identified as such, the reconstructed particles resemble the signal particle content.

The subsequent largest contribution are processes with a charm quark in the final state. This category includes both $W + c$ and $W + \bar{c}$ production, as shown in 1.11a, and $W + c\bar{c}$, depicted in 1.11b. The combined process is referred to as $W + c(\bar{c})$. While the $W + c\bar{c}$ cross-section is symmetric in lepton charge, the $g + d \rightarrow W^- + c$ process has a larger cross-section than $g + \bar{d} \rightarrow W^+ + \bar{c}$ due to the down quark's role as a valence quark in the proton.

Since the $|V_{ub}|$ and $|V_{cb}|$ CKM matrix elements are small, the $W + b$ process is significantly suppressed. Another contribution from the W+jets process stems from W+light jet production. For this process to align with the signature of the t-channel process, a light jet must be incorrectly identified as a jet originating from a bottom quark.

1.17. Other Background Processes

Other background processes of smaller relevance include Z+jets production and the generation of two bosons with accompanying jets. At leading order, Z bosons

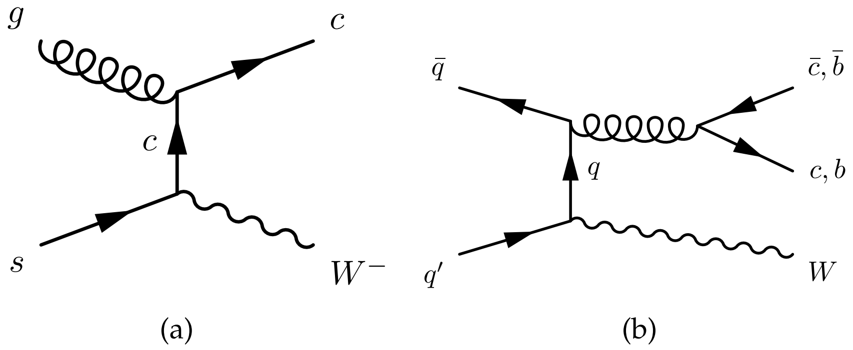

Figure 1.11.: Leading order Feynman diagrams of W+jets production

decay into a fermion and its corresponding antiparticle. Specifically, decays into an e^+e^- or $\mu^+\mu^-$ pair constitute 6.7 % of total decay events [14]. These events can mirror the signal signature if one of the resultant leptons are undetected or omitted. The Z+jets background is largely filtered out during the analysis through event selection criteria. The production of multiple bosons also contributes as a background, but it has a smaller overall cross-section.

Numerous strong interaction processes do not result in lepton production. However, there are various mechanisms through which such events might infiltrate the leptonic event selection in this analysis. One such instance involves a jet being erroneously identified as an electron, referred to as a "fake" electron. Another scenario includes the decay of B hadrons into muons or the generation of electron pairs through the interaction of photons with detector material. Leptons produced through these means are termed "non-prompt" leptons. The combination of these processes is denoted as the multijet background and is further discussed in Chapter 4.

2. The Large Hadron Collider

The Large Hadron Collider (LHC) [50], the world's largest and most powerful particle accelerator, is located at the European Organization for Nuclear Research (CERN) in Switzerland. It was built with the primary objective of studying the fundamental nature of matter and the forces that govern it.

The LHC is designed to accelerate particles to energies of up to 14 TeV, colliding them at four interaction points. By studying the particles produced by these collisions, one can gain insights into the properties of subatomic particles, including the Higgs boson, which was famously discovered at the LHC in 2012 by the ATLAS [27] and CMS [28] experiments.

A schematic overview of the LHC and CERN's accelerator complex is shown in Figure 2.1. The LHC is a 26.7 km circumference synchrotron, a circular particle accelerator with magnetic fields adapting to the particle energy to keep them on their fixed paths. The LHC has two beam pipes accelerating particles in opposite directions. A number of smaller accelerators are used before injecting the particles into the LHC.

Firstly, H^- ions are fed into the Linear accelerator 2 (Linac 2) bringing the ions to an energy of 50 MeV. Protons are produced by passing the ions through an electric field stripping away the electrons. The protons are accelerated in bunches by passing through radio frequency cavities timed to produce electric fields accelerating the particles. After the initial acceleration in the Linac 2 to 50 MeV, the protons are further accelerated in the Proton Synchrotron Booster (PSB), the Proton Synchrotron (PS) and the Super Proton Synchrotron (SPS) before being injected into the LHC. The PSB increases the proton energy to 1.4 GeV, the PS increases it to 25 GeV and the SPS further boosts it to 450 GeV, preparing the protons for injection into the LHC, where they reach their maximum energy of 6.5 TeV per beam before colliding in the four interaction points of the LHC.

The protons within the LHC are grouped into bunches, traveling in opposite directions in the two beam pipes. The acceleration of these protons is achieved using superconducting cavities that resonate at a frequency of 400 MHz and reach a maximum voltage of 2 MV. The protons are longitudinally focused by

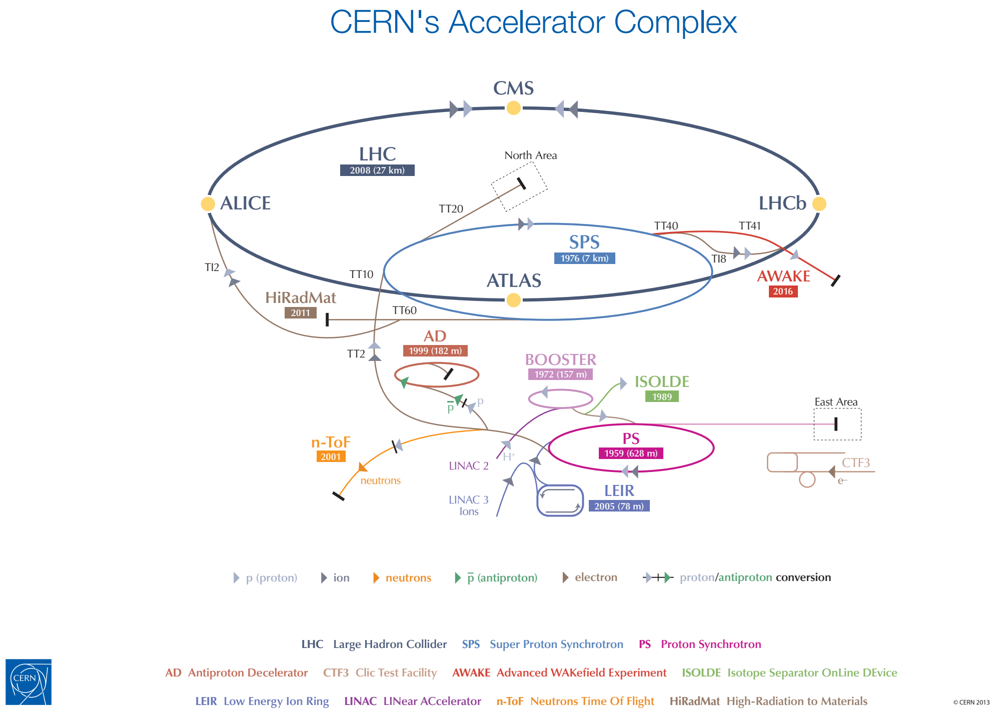

Figure 2.1.: Schematic overview of CERN's accelerator complex [51].

synchronizing their passage through the accelerating cavities to coincide with the rising phase of the voltage oscillation. This synchronization ensures that a proton ahead of the bunch receives greater acceleration in the cavity, leading it to follow a longer path around the ring. Conversely, protons lagging behind the bunch receive less acceleration and hence take a shorter path. This process, known as phase focusing, creates approximately 35 570 potential 'buckets' for proton acceleration in each beam of the LHC. However, due to limitations in injecting bunches into the LHC and to minimize heat load on the beam screens from electron clouds generated by synchrotron radiation, typically only around 2,808 bunches are filled during a run. These bunches are arranged in trains of a number bunches with a spacing of 25 ns.

The path of the particles is curved using 1232 helium cooled superconducting dipole magnets providing magnetic fields of 8 T. The magnets are cooled to temperatures below 2 K using superfluid Helium to remain superconducting. The transverse focusing of the particles in the beam is achieved using alternating vertically or horizontally focusing quadropule magnets. Additional setups are in place actively monitoring and correcting the paths of the particles. The operation of the accelerator complex is highly complex and requires permanent monitoring

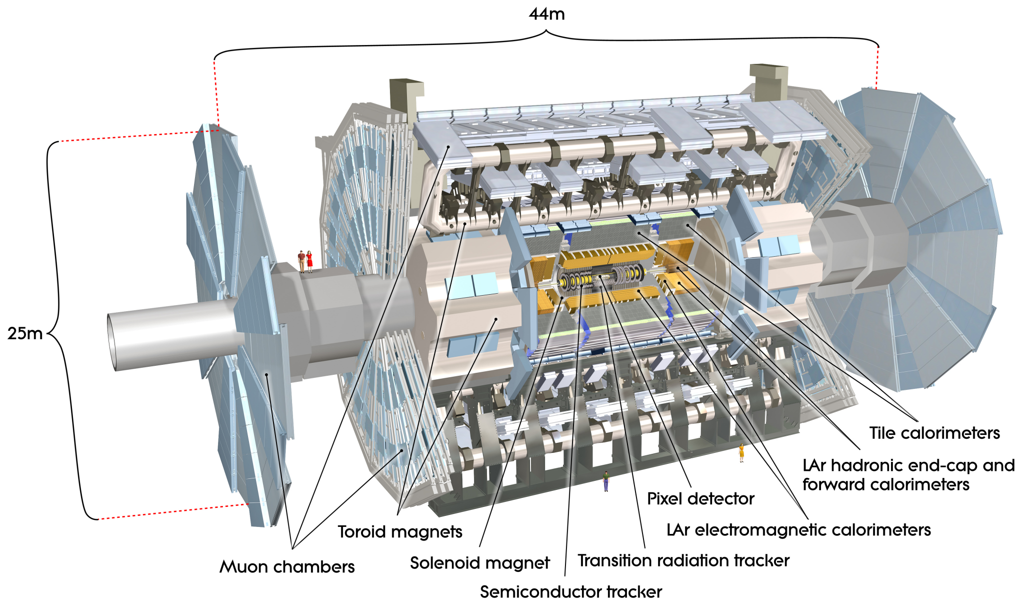

Figure 2.2.: Schematic view of the ATLAS detector [52].

for several systems during operation. At the interaction points of the LHC large detectors are installed: The two general purpose detectors ATLAS [52] and CMS [53], the LHCb [54] experiment focusing on B-physics and the heavy ion experiment ALICE [55].

2.1. ATLAS

The ATLAS detector [52], one of the two general-purpose detectors at the LHC, consists of a variety of subdetector systems, arranged in concentric layers around the interaction point, each designed to measure specific properties of particles produced in collision events. Its superconducting magnets generate strong magnetic fields that cause charged particles to follow curved trajectories through the detector. The curvature of these paths is utilized to determine the particles' momentum, while their energy is measured by their absorption in calorimeters.

Figure 2.2 provides a schematic view of the ATLAS detector. The protons intersect or collide in a small localized area called the beamspot of intense particle activity and interactions in the center of the detector. The various subdetector systems are each engineered for specific measurements of particles produced in the collisions. The inner detector systems are used for the reconstruction of particle tracks, collision vertices, and decay vertices of particles. These systems also play a significant role in the detector's trigger system, which is essential for event recording.

Surrounding the inner detector is the solenoid magnet, which generates a 2 T magnetic field [56], bending the paths of charged particles. The next layer is the calorimeter system, divided into the electromagnetic calorimeter (ECAL) for absorbing and measuring the energy of electrons and photons, and the hadronic calorimeter (HCAL) for hadrons and jets.

The calorimeter system is encircled by toroid magnets, arranged around the muon spectrometer, specifically designed to measure muon momentum by tracking the curvature of their paths.

Particles are differentiated based on their interactions with the detector. Photons, with no electric charge, bypass the inner tracking detector and are absorbed in the ECAL. Electrons leave a track in the inner detector before being absorbed in the ECAL. Muons, also charged, create tracks but penetrate further, reaching the muon spectrometer. Jets leave tracks in the inner detector and deposit energy in both calorimeters, aiding in their identification and reconstruction.

2.1.1. Coordinate System

The description of positions relative to the interaction point in the ATLAS detector employs various coordinate systems. A right-handed Cartesian coordinate system, centered at the interaction point, is defined where the x-axis points towards the center of the LHC, the y-axis points upwards, and the z-axis aligns with the anti-clockwise direction of the beam pipe.

In addition, a spherical coordinate system is used, characterized by the polar angle θ measured from the z-axis, the azimuthal angle ϕ measured from the x-axis and the radial distance r from the beam pipe. Additionally, often the linear distance $r\phi$ along the direction of the azimuthal basis vector e_ϕ is used.

Particle momenta in the z-direction are often quantified using rapidity, defined as:

$$y = \frac{1}{2} \ln \left(\frac{E + p_z}{E - p_z} \right) .$$

Rapidity is particularly useful because the difference in rapidity between two particles remains invariant under Lorentz boosts along the z-axis. For high-energy particles, rapidity (y) can be approximated by pseudorapidity (η), calculated as:

$$\eta = -\ln\left(\tan\frac{\theta}{2}\right).$$

The angular distance ΔR between two particles is then determined using the differences in their pseudorapidity (η) and azimuthal angle (ϕ):

$$\Delta R = \sqrt{(\Delta\eta)^2 + (\Delta\phi)^2}.$$

2.1.2. Inner Tracking Detector

The inner tracking detector is responsible for measuring the tracks of charged particles produced in the collisions. The tracks are used to reconstruct momenta, primary vertices, and decay vertices of the particles in a range of $|\eta| < 2.5$. The Pixel detector [52] is used to achieve high resolution near the interaction point, followed by the Semiconductor Tracker (SCT). The outer part of the inner detector is comprised of the Transition Radiation Tracker (TRT) able to identify electrons along with measuring the tracks. Its design enables the inner detector to function effectively even in the presence of the high number of particles produced in each bunch crossing.

The pixel tracking detector consists of four cylindrical barrel layers around the beam pipe and three end caps of high-precision pixel modules. The Insertable B-Layer (IBL) [58], the innermost layer, was installed at a radius of 3.3 cm from the beam axis in 2014 during the Long Shutdown 1 to enhance the tracking performance. The about 12 million pixels of the IBL have a size of $50 \times 250\,\mu\text{m}^2$ each and are designed to cope with the high density of tracks near the interaction point. The outer three layers of the pixel detector have a combined 80 million pixels, each with a size of $50 \times 400\,\mu\text{m}^2$. The pixel detector has a very high spatial resolution of $10\,\mu\text{m}$ in $r\phi$ and $60\,\mu\text{m}$ in z for the barrel region or $115\,\mu\text{m}$ in r for the end caps, which allows for the accurate reconstruction of the particle's path.

The SCT [59–61] is positioned around the Pixel detector and consists of silicon strip modules. These modules are arranged in four barrel layers and two end caps each consisting of nine discs of modules. Each module contains two pairs of strip sensors, with each pair rotated by an angle of 40 mrad relative to one another. The modules have a much better lateral resolution than longitudinal resolution with respect to the strips. The arrangement of the modules within the detector is designed to align the strips parallel to the beam axis for the barrel modules and orthogonal to the beam axis for the end cap modules, allowing for

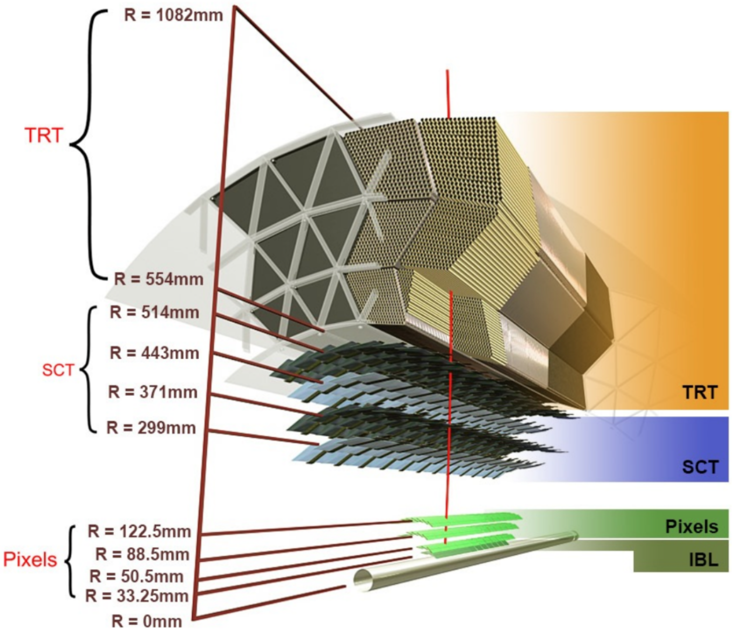

Figure 2.3.: Schematic view of the layers of the inner detector [57].

an enhanced resolution in $r\phi$ of 17 µm while the resolution in z for the barrel and r for the end caps is 580 µm.

The final subsystem of the inner detector is the TRT, which is located around the SCT, covering the range $|\eta| < 2.0$. The TRT detector elements consist of 4 mm diameter polyimide drift (straw) tubes, filled with a Xe-based gas mixture, interleaved with transition radiation material. In the middle of the tubes, gold plated tungsten wires act as an anode with a potential of -1530 V.

High energy particles passing through the drift tubes ionize the gas setting free electrons. These electrons then drift towards the wire causing a cascade of electrons which is detected as a current in the electric circuit. Electron drift time is used to infer the location of passing particles yielding a spatial resolution of 130 µm.

The production of transition radiation depends on the Lorentz factor γ of the particles. Due to the small mass of electrons they produce high amounts of transition radiation compared to heavier charged particles. The transition radiation produces a high amount of electrons in the drift tubes and can thereby be distinguished from other ionizing particles such as pions.

Together, the three subsystems of the inner tracking detector provide a very

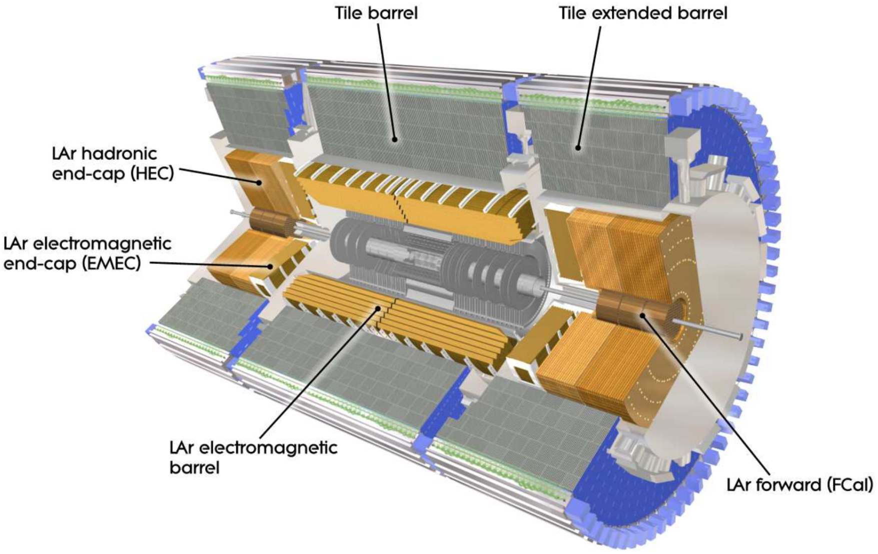

Figure 2.4.: Schematic view of the calorimeters of the ATLAS detector [52].

precise measurement of the trajectories of charged particles, which can be used to reconstruct particle momenta, interaction vertices and decay vertices. Among else, this information is later used to identify the production of B-hadrons

The exact geometry and alignment of the inner detector is measured over time by minimizing track-hit residuals of reconstructed tracks in the detector [62].

The inner detector components achieve a transverse momentum resolution of

$$\sigma_{p_\mathrm{T}}/p_\mathrm{T} = 0.05\% \cdot p_\mathrm{T}[\mathrm{GeV}] \oplus 1\%$$

where $\oplus$ denotes addition in quadrature.

2.1.3. Calorimeter System

The calorimeter system is designed to measure the energy and position of particles that are absorbed in the calorimeter. The arrangement of the calorimeters is schematically shown in Figure 2.4.

The ECAL consists of a barrel section arranged cylindrically around the inner detector and two end-cap sections (EMEC). While the electromagnetic calorimeter covers a range of $|\eta| < 3.2$ the forward calorimeter (FCAL) can measure electrons and photons up to $|\eta| < 4.9$. The ATLAS calorimeters use two alternating materials, an absorber material and an active detector medium. Additionally, electrode layers are inserted to detect the electrons produced in the active material.

The ECAL uses lead as an absorber and liqiud argon as an active detector medium. High energy electrons produce photons through bremsstrahlung in the absorber material. Conversely, photons produce electron-positron pairs through interaction with a nucleus in the absorber material, which can again produce photons, as long as their energy is still high enough. This repeating process produces a particle shower in the calorimeter. In the liquid argon, the particles ionize the gas producing electrons which drift to an electrode layer placed between two absorber layers. The electrode layer is made of three insulated copper layers, where the outer ones are at the high-voltage potential and the middle one is used to measure the currents via capacitive coupling.

The absorber and electrode layers are arranged in an accordion structure, where they run in a zig zag pattern radially for the barrel section which covers $|\eta| < 1.475$ and axially in end caps covering $1.375 < |\eta| < 3.2$. This has the advantage that electrode layers correspond to values in ϕ simplifying the segmentation and readout of the electrode layers significantly. The electrodes are further separated in η and three depth layers by etched patterns on the electrodes. The segmentation in η is made finer for the inner most layer and less fine for the outer layer. Overall the ECAL measures the energy of absorbed particles with a relative resolution of

$$\sigma(E)/E = \frac{10\%}{\sqrt{E[\mathrm{GeV}]}} \oplus 0.7\%.$$

The hadronic tile calorimeter (HCAL) is located in a cylindrical shape around the electromagnetic and end cap calorimeters. It is split into a central barrel section covering $|\eta| < 1.0$ and an extended barrel section covering $0.8 < |\eta| < 1.7$. Two hadronic end cap calorimeters cover the range $1.5 < |\eta| < 3.2$. The hadronic calorimeters are designed to measure the energy of hadrons, which interact primarily through strong nuclear interactions. The HCAL is composed of layers of steel plates, which are interspersed with layers of plastic scintillator material. When a hadron enters the hadronic calorimeter, it interacts with the metal plates and produces a shower of secondary particles. The shower of particles produces a cascade of light, which is detected by photodetectors located at the back of the HCAL. By measuring the amount of light produced by the particles, the energy of the original particle can be determined. The hadronic end cap calorimeter uses flat plates of copper as an absorber and liquid argon as active material. Its readout is segmented in η and ϕ to enable spatial resolution. The HCAL measures the energy of absorbed particles with a relative resolution of

$$\sigma(E)/E = \frac{50\%}{\sqrt{E[\mathrm{GeV}]}} \oplus 3\%.$$

The FCAL is used in addition to the electromagnetic and hadronic calorimeters to measure the forward region of $3.1 < |\eta| < 4.9$ and has three layers, one electromagnetic layer and two hadronic layers. The electromagnetic layer uses copper as an absorber and the hadronic layers use tungsten. Tubes and rods made out of the absorber material are arranged parallel to the beam pipe. The gap between the rods and the tubes is filled with liquid argon and just 0.27 mm to 0.50 mm thin, allowing for a fast readout necessary for the high particle density in the forward region.

The FCAL reduces the number of particles escaping undetected in the forward region, which is crucial for a precise determination of the missing transverse momentum. The FCAL measures the energy of absorbed particles with a relative resolution of

$$\sigma(E)/E = \frac{100\%}{\sqrt{E[\mathrm{GeV}]}} \oplus 10\%.$$

Together, the ECAL, HCAL, and FCAL provide a complete measurement of the energy of particles produced in the ATLAS collisions. The data collected by the calorimeter system is used in conjunction with the other subsystems of the ATLAS detector to identify particles and measure their properties.

2.1.4. Muon Spectrometer

The muon spectrometer (MS) is positioned around the calorimeters. Muons typically have the ability to traverse the entire detector. As a result, the MS plays a pivotal role in identifying muons and measuring their momenta. The paths of the muons are measured using drift chambers. The magnetic field, generated by the toroid magnets, enables the reconstruction of muon momenta by assessing the curvature of their tracks. In the barrel region, a magnetic field reaching up to 2.5 T is generated by a barrel toroid. Complementing this, two smaller end-cap toroids produce a magnetic field of up to 3.5 T. Each toroid, comprising eight evenly distributed superconducting coils encircling the beam pipe, creates magnetic fields that effectively bend the trajectories of muons in the η direction. In the barrel section, the drift chambers are situated between and on the magnet coils in three layers each made of eight larger and eight smaller chambers. In the end-cap section, the chambers are arranged in three discs on each side of the detector, one in front and two behind the end-cap toroid magnets.

Most drift chambers are Monitored Drift Tube (MDT) chambers constisting of three to eight layers of cylindrical aluminum drift tubes with a diameter of 3 cm with a centered anode wire. When muons pass through the drift tubes electrons and gas ions are produced which drift to the cathode tube wall and anode wire, respectively. The drift time of the electrons is used to measure the distance of the track to the wire. Information from the tubes are combined to measure the muon track orthogonal to the magnetic field with a resolution of around 35 µm. The support structure the tubes are placed on needs to be built extremly precisly. To account for changes in the structure an active monitoring system is built into the frame. In the forward region of the inner most end cap layer, Cathode-Strip Chambers (CSCs) are employed due to the higher amount of particles produced in the forward region. The CSCs are multi-wire proportional chambers with segmented cathode walls. One cathode wall is finely segmented in η allowing for a resolution of 60 µm in the bending direction of the muons, the other is segmented broadly in $r\phi$ resulting in a resolution of 5 mm transverse to the bending plane of the muons.

2.1.5. Trigger System

ATLAS is equipped with a sophisticated trigger system that filters out unwanted data and selects interesting events for further analysis.

The ATLAS trigger system consists of three levels, the Level-1 (L1) trigger, the Level-2 (L2) trigger and the event filter. The L2 and event filter form the high-level trigger (HLT). The L1 trigger is a hardware-based system that performs a fast selection of events based on simple criteria. It is composed of two main parts: the calorimeter trigger and the muon trigger. The calorimeter trigger analyzes the energy deposited in the detector's calorimeter system to identify high-energy particles and missing transverse momentum, while the muon trigger uses information from the special muon trigger detectors, the Resistive Plate Chambers (RPC) and Thin-Gap Chambers (TGC) located around the MDT chambers, to identify high-energy muons. The information from these triggers is combined to select the most interesting events for further analysis.

If an event passes the L1 trigger, it is sent to the L2 trigger along with information about Regions-of-Interest (RoIs) identified by the L1 trigger and used by the L2 trigger to limit the data needed from the readout. The L2 trigger is a software-based system that performs a more detailed analysis of the data.

Events passing the L2 trigger are fully reconstructed using the complete detector information, and in the event filter an offline analysis is run, selecting the events which are permanently saved. The ATLAS trigger system is designed to reduce the data rate from the collision rate of up to 40 MHz down to a rate of approximately 1.2 kHz [63], which is compatible with the available storage and processing capabilities.

2.1.6. Luminosity

The SM provides theoretical predictions in terms of cross-sections, which are independent of experimental conditions, such as the number of colliding particles in a detector. To derive the predicted number of particles produced by a specific process, the cross-section σ is multiplied by the instantaneous luminosity $\mathcal{L}$. This luminosity encompasses information about the experimental setup, including the intensity and density of the particle beams. The relationship is given by the formula:

$$\frac{dN}{dt} = \sigma \mathcal{L}$$

where $\frac{dN}{dt}$ represents the rate of a specific scattering process. Thus, the instantaneous luminosity directly influences the number of events detected for a given process. A higher luminosity increases the probability of detecting rare events, making it a crucial factor in the design and operation of particle colliders. Luminosity can be expressed in terms of the number of bunches n_b, number of protons per bunch n_p, revolution frequency f_r, and the convoluted transverse beam sizes σ_x and σ_y:

$$\mathcal{L} = \frac{n_\mathrm{b} n_p^2 f_\mathrm{r}}{2\pi \sigma_x \sigma_y}$$

The LHC has a revolution frequency of $f_\mathrm{r} = 11.245\,\mathrm{kHz}$. In the data used for this analysis, the number of bunches ranges from $n_\mathrm{b} = 2220$ to $n_\mathrm{b} = 2556$, and the protons per bunch vary between $n_\mathrm{p} = 1.1 \times 10^{11}$ and $n_\mathrm{p} = 1.25 \times 10^{11}$. An accurate determination of the integrated luminosity is essential for many analyses since all predicted event yields are proportional to it. The most precise determination of the integrated luminosity for this analysis is $\mathcal{L}_\mathrm{int} = 140.1\,\mathrm{pb}^{-1}$ with a relative uncertainty of 0.83 % [64]. The value is derived from van der Meer scans during special annual runs and extrapolated to physics data-taking using measurements from multiple luminosity-sensitive detectors.

The total integrated luminosity of the LHC during the Run 2 data-taking period is shown in Figure 2.5.

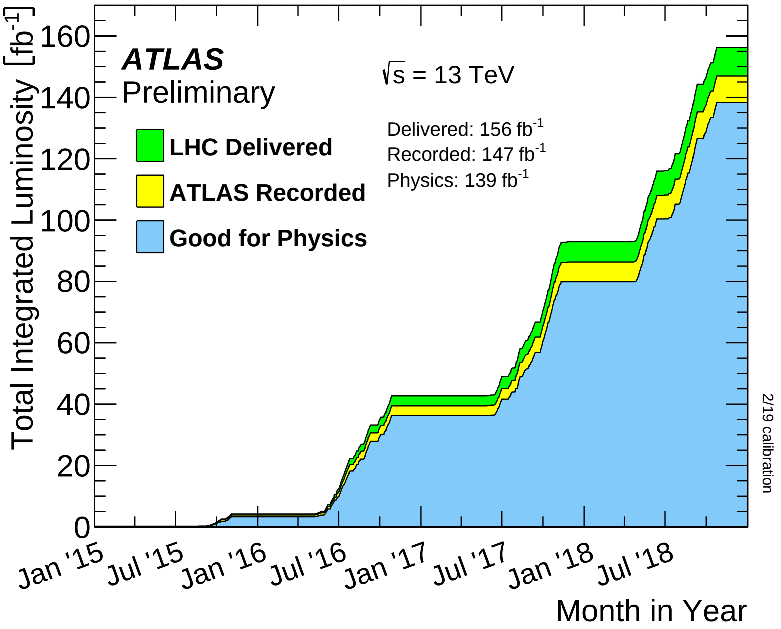

Figure 2.5.: Integrated luminosity during Run 2 using a previous calibration of the luminosity [65].

2.2. LHC Run 2

The data sample used for the analysis is defined by further requirements based on stable beam conditions, correct functionality of all ATLAS subdetectors and a set of data-quality requirements [66]. In the years 2015 to 2018, the Run 2 of the LHC took place. During this period, the LHC operated at a center-of-mass energy of 13 TeV, significantly higher than in previous runs.

The dataset collected during Run 2 comprises a vast amount of collision data, amounting to an integrated luminosity of 140.1 fb^{-1}. This represents a substantial increase in data volume compared to Run 1.

Upgrades and maintenance were performed on the ATLAS detector between the LHC Runs to ensure optimal performance despite the increased demands placed on the detector system by the higher collision energy and luminosity. The distribution of the number of pileup events in Run 2 is shown in Figure 2.6 split up into periods of one year.

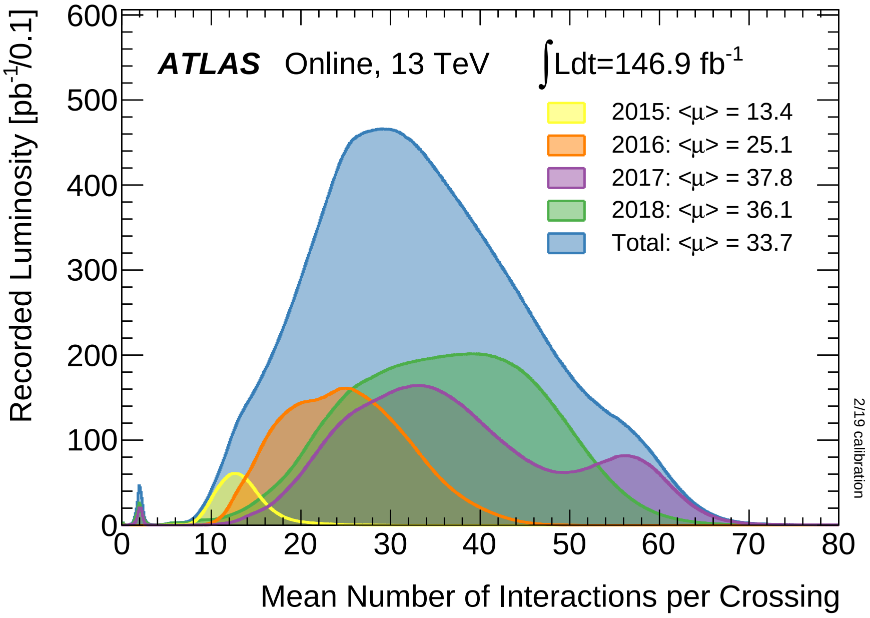

Figure 2.6.: Mean number of interactions per bunch crossing during Run 2 [65].

3. Monte Carlo Samples

To effectively analyze data recorded with the ATLAS detector, accurate theoretical predictions of the distributions of reconstructed quantities are essential. As detailed in Chapter 1, individual hard scattering events are generated using generator programs specifically designed for this purpose. These programs are interfaced with a showering algorithm to model the development of parton showers, hadronization, and the underlying event. Subsequently, the response of the detector is simulated. For these various steps, different programs are employed, each selected for their specific advantages in modeling different processes. In this Chapter, the setups used for the different processes are described.

In all simulated processes, the effects of pileup have to be accounted for. To describe pileup in the simulation, the number of bunch crossings per event, denoted as μ, is defined. μ is determined in each event using the count of reconstructed vertices. In the MC simulations, pileup is accounted for by adding simulated minimum bias events to the hard scattering event. The μ measured in MC is then compared to data, and adjustments are made by applying event weights to account for any differences in the μ distribution.

3.1. Signal Sample

The t-channel process is simulated at NLO in QCD using the POWHEG BOX v2 [67–73] matrix-element generator. The process is generated in the four-flavor scheme, with the top-quark mass set to $m_t = 172.5\,\text{GeV}$. The PDF set NNPDF3.0NLO_NF4 [74] is utilized for this simulation.

POWHEG BOX v2 has been optimized to match NLO matrix-element calculations with parton showers. It is interfaced with PYTHIA 8.230 [75] for parton shower generation, using the A14 parameter set [76] and the NNPDF2.3LO PDF set [77].

The simulated event samples for tq and $\bar{t}q$ production are normalized using predicted cross-sections calculated by the MCFM 10.1 program at NNLO in

QCD [78]. The cross-section for tq production is set at $\sigma(tq) = 134.2 \pm 2.2$ pb, with a relative uncertainty of 1.6%, while the cross-section for $\bar{t}q$ production is $\sigma(\bar{t}q) = 80.0 \pm 1.6$ pb, corresponding to a relative uncertainty of 2.0%.

The renormalization and factorization scales in this simulation are set according to the guidelines in Ref. [73], specifically to $\sqrt{m_b^2 + p_{\mathrm{T},b}^2}$. This setting ensures an accurate representation of particle interactions at these scales.

The decay of the top quark is calculated separately, employing the NWA, which confines the simulation to on-shell top quark states. To account for finite-width effects in the top-quark decay, the top-quark mass is subsequently modified to follow a Breit-Wigner distribution. To ensure the preservation of spin correlations, the top quarks are decayed at LO using MadSpin [79, 80]. This method effectively retains the angular correlations between the initial and final state particles. Additionally, the decays of bottom and charm hadrons are simulated using the EvtGen 1.6.0 program [43].

To estimate the uncertainty in the choice of shower algorithm, an alternate generator setup, interfacing Powheg Box v2 with Herwig v.7.2.1p3, is used to produce a comparative sample.

Furthermore, to address the uncertainty in the matching procedure between Powheg Box and Pythia, an additional sample is created by modifying the `POWHEG:pThard` parameter to one, which determines how the hardness of the Powheg event is determined in Pythia. While zero is the default setting for `pTHard`, adjusting it to one provides a viable alternative for estimating the uncertainty in the matching procedure. Employing a different matching algorithm altogether could be another method for quantifying this uncertainty. However, such alternative configurations have additional changes and are not as finely tuned to data as the Powheg Box + Pythia setup which might result in an overestimation of the uncertainty.

For the nominal sample, the detector simulation employs a full Geant4-based model [81]. For alternative samples, which are used to define systematic uncertainties, the faster Atlfast-II simulation is utilized. Additionally, to ensure consistency and avoid attributing differences between the full Geant4 simulation and Atlfast-II to uncertainties, the nominal sample is also produced using Atlfast-II for comparative purposes.

3.2. Single Top Background

The tW process is simulated using the POWHEG BOX v2 generator at NLO in QCD. This simulation employs the five-flavor scheme along with the NNPDF3.0NLO PDF set. To mitigate interference and overlap with $t\bar{t}$ production, the diagram removal scheme is utilized [82]. The uncertainty associated with this approach is estimated by comparison with an alternative sample generated using the diagram subtraction scheme [82, 83]. The events are interfaced with PYTHIA 8.230, applying the A14 parameter set and the NNPDF2.3LO PDF set [77].

The sample is normalized to conform with a total cross-section of $\sigma(tW + \bar{t}W) = 79.3 \pm 2.9\,\text{pb}$, corresponding to a relative uncertainty of 3.7%. This normalization is based on calculations at NLO in QCD [84].

Similarly, single-top s-channel production is simulated with POWHEG BOX v2 at NLO in QCD. This process also uses the five-flavor scheme and the NNPDF3.0NLO PDF set [85]. For the generation of the parton shower, POWHEG BOX v2 is interfaced with PYTHIA 8.230, utilizing the A14 tune and the NNPDF2.3LO PDF set.

The sample is normalized to match a total cross-section of $\sigma(t\bar{b} + \bar{t}b) = 10.32 \pm 0.38\,\text{pb}$, which corresponds to a relative uncertainty of 3.7%. This value is calculated at NLO in QCD using the HATHOR 2.1 program [86, 87].

Alternative samples using POWHEG BOX+PYTHIA are generated, with `pTHard` set to one, to describe the uncertainty of the matching procedure.

For these samples, the nominal simulation uses the full GEANT4 detector simulation, while alternative samples for systematic uncertainties and comparative analysis employ the quicker Atlfast-II [44] simulation.

3.3. $t\bar{t}$ Background

The $t\bar{t}$ process is simulated using POWHEG BOX v2, employing the NNPDF3.0NLO PDF set in the five-flavor scheme.

Parton showering, hadronization, and the modeling of the underlying event are accomplished using PYTHIA 8.230 with the A14 set of tuned parameters and the NNPDF2.3LO PDF set. The POWHEG BOX + PYTHIA generator setup uses a matching scheme for hard emissions in the two programs. This matching is governed by the h_{damp} parameter, which controls the p_{T} of the first additional gluon emission beyond the LO Feynman diagram in the parton shower. Thus, it regulates the high-p_T emission against which the $t\bar{t}$ system recoils. Event generation was performed with $h_{\text{damp}} = 1.5 \times m_t$ [83]. To evaluate the uncertainty of the procedure a comparative sample is generated with $h_{\text{damp}} = 3 \times m_t$.

The simulated $t\bar{t}$ event sample is normalized to align with a total cross-section of $\sigma(t\bar{t}) = 834 \pm 33\,\text{pb}$, corresponding to a relative uncertainty of 4.0%. This calculation uses the NNLO computations provided by the TOP++ 2.0 program. As outlined in Ref. [88], along with its associated references, TOP++ 2.0 not only does the NNLO calculations but also integrates the resummation of next-to-next-to-leading logarithmic soft-gluon terms, enhancing the precision and reliability of the calculation.

To estimate the uncertainty arising from the choice of the shower algorithm, an alternative generator setup is employed to produce a comparative sample. In this setup, POWHEG Box v2 interfaces with HERWIG v.7.2.1p3 [89, 90].

An alternative sample using POWHEG BOX+PYTHIA is generated, with `pTHard` set to one.

The nominal simulation uses the full GEANT4 detector simulation, while alternative samples for systematic uncertainties and comparative analysis employ the quicker Atlfast-II simulation.

3.4. Boson processes

The production of Z+jets and W+jets events is simulated with the SHERPA 2.2.1 [91] generator using NLO matrix elements for up to two partons, and LO matrix elements for up to four partons calculated with Comix [92] and OPENLOOPS [93–95]. They are matched with the SHERPA parton shower [96] using the MEPS@NLO prescription [41, 97–99] and the set of tuned parameters developed by the SHERPA authors. The NNPDF3.0NNLO set of PDFs [85] was used, and the samples were normalized to a NNLO prediction [100].

QCD $V+$ jets production is simulated with the SHERPA v2.2[101] parton shower Monte Carlo generator. Additional hard parton emissions [92] are matched to a parton shower based on Catani-Seymour dipoles [96]. The NNPDF3.0NNLO set [85] of PDFs as well as the dedicated set of tuned parton shower parameters developed by the SHERPA authors for this version are used.

The ME+PS matching [41] is employed for different jet multiplicities which are then merged into an inclusive sample using an improved CKKW matching procedure [98, 99] which is extended to NLO accuracy using the MEPS@NLO prescription [97]. These particluar simulations are NLO accurate for up to two additional partons and LO accurate for up to four additional partons. The virtual QCD correction for matrix elements at NLO accuracy is provided by the OpenLoops library [94, 95].

The $V+$ jets samples are normalized to a NNLO prediction [100].

For the nominal samples the full Geant4 detector simulation is used, while alternative samples for systematic uncertainties and comparative analysis employ the quicker Atlfast-II simulation.

4. Multijet Background

The multijet process encompasses all processes that do not incorporate a lepton in their hard scattering final state. Multijet events may infiltrate the selection if a jet is mistakenly identified as a lepton, or if hadrons within the jets decay, thereby producing real non-prompt leptons. Furthermore, electrons can be produced from photon conversion in the detector material.

Despite the multijet process possessing an exceptionally large cross-section, events from this process are very infrequently selected in the presented analysis due to the lepton requirements applied in the analysis. Simulating multijet events using the MC methods used for the other processes proves to be unfeasible due to the low efficiency of selected events. Consequently, two methods are utilized in this analysis to generate event samples that emulate the multijet process. The used methods, however, do not offer an estimate of the overall number of events of the multijet process, leaving the normalization of the samples to be determined from data. The normalization is first determined in a preliminary multijet estimate described in Section 6.1 and later determined simultaneously with the signal parameters in the statistical analysis, which accounts for all uncertainties.

In this analysis, the multijet process is categorized into subprocesses depending on the presence of a muon or an electron in the event. Furthermore, electron subprocesses are classified based on the electron's pseudorapidity, differentiating between events with $|\eta| < 1.37$, labeled `mj` e, and those with $|\eta| > 1.52$, labeled `mj` fe. The subprocess involving muons is labeled `mj` μ.

4.1. Jet-Electron Method

The jet-electron method [102] is implemented for multijet events where an electron is found in the final state. This method employs a dijet MC simulation sample. This sample is produced using PYTHIA 8.186, employing LO matrix elements, combined with a p_{T}-ordered parton shower. The renormalization (μ_{r}) and factorization (μ_{f}) scales in this simulation are set to the square root of the geometric mean of the product of the squared transverse masses of the two outgoing particles from the matrix element. Specifically,

$$\mu_\mathrm{r} = \mu_\mathrm{f} = \sqrt[4]{(p_{\mathrm{T},1}^2 + m_1^2)(p_{\mathrm{T},2}^2 + m_2^2)}.$$

During the generation process, a filter is applied at the generator level to ensure the presence of at least one jet with a transverse momentum p_T exceeding 17 GeV. The generation of this sample uses the NNPDF2.3LO PDF set and employs the A14 tuning parameters set.

In the dijet MC sample, jets that deposit a high fraction of their energy in the electromagnetic calorimeter are reclassified as 'jet electrons'. These jet electrons are jets that have a higher probability of being mistakenly identified as electrons. In the analysis that follows, these jet electrons are treated as identified electrons, not as jets, to mimic the real-world scenario where jets are misidentified as electrons.

For a jet to be classified as a jet electron, it must meet several conditions: it should deposit more than 80 % of its energy in the electromagnetic calorimeter ($f_\mathrm{EM} > 0.8$), possess a transverse energy $E_\mathrm{T} > 25$ GeV, and have a pseudorapidity $|\eta| < 2.4$.

To assess the uncertainty of this method, an additional sample is created with a modified criterion for the energy deposited in the electromagnetic calorimeter, specifically $f_\mathrm{EM} > 0.9$. This variation can be compared to the nominal sample to estimate the robustness and reliability of the jet electron identification process.

4.2. Anti-Muon Method

For multijet events where a muon is found in the final state, the data-driven anti-muon method [102] is employed. This technique utilizes a data sample that is enriched in muons originating from hadron decays, since the number of multijet events with jets misididentified as muons is negligible. To obtain events that are enriched in such non-prompt muons, the usual muon selection and isolation criteria are replaced by a set of criteria that select non-isolated muons with similar kinematic properties to isolated muons. Notably, an inverted isolation requirement is used, requiring the transverse energy measured in the calorimeters within a ΔR of 0.2 around the muon to be larger then 0.03 times the muon p_T.

The resulting sample contains real data events highly enriched in the multijet process with non-prompt muons that would be removed by isolation requirements in the actual data sample. At the same time the events in the sample mimic events where non-prompt muons wrongfully pass the nominal isolation requirements.

5. Event Reconstruction

For subsequent analysis, it is beneficial to translate the data measured by the detector back to objects representing the final state particles from the hard scattering process. This event reconstruction process involves combining data from various detector systems to identify and characterize particles produced in the collision. The process utilizes tracking information of charged particles, energy deposits in the calorimeters, and data from the muon system. This approach allows for identifying different particle types, such as electrons, muons, and jets, and reconstructing their energy and direction. By combining this information, a detailed representation of the event is constructed.

5.1. Particle tracks

Tracks of charged particles measured in the inner detector are used to reconstruct the momentum of the particles. This is achieved by measuring the curvature of the tracks in the strong magnetic field of the solenoid magnet. Each interaction between a particle and an inner detector module yields a measured signal, referred to as a hit. Subsequently, a tracking algorithm [103, 104] identifies hits belonging to the same track.

The track reconstruction process begins with clusterization. This involves assembling clusters from raw sensor measurements, where a connected component analysis groups pixels and strips in each sensor into clusters. These are based on deposited energy resulting in a charge above a certain threshold. From these clusters, three-dimensional measurements, known as space-points, are created. Notably, in pixel sensors, the charge is often dispersed across multiple adjacent pixels. The precise intersection point with the sensor is calculated from the pixels contributing to the cluster, using a linear approximation technique that is refined with charge interpolation.

These clusters are then categorized: those formed from charge deposits by a single particle are called single-particle clusters, whereas those from multiple particles are termed merged clusters. The primary-track reconstruction algorithm takes over from here, forming track seeds from sets of three space-points. Utilizing a combinatorial Kalman filter [105], these seeds are extended into track candidates. This filter methodically incorporates additional space-points from the pixel and SCT detectors' remaining layers, provided they align with the initial trajectory.

However, this stage can result in an ambiguity of track candidates, where space-points overlap or are misassigned. To resolve this, an ambiguity-solving stage is implemented. Tracks are processed individually, prioritized by a track score that hinges on simple measures of track quality. A crucial part of this stage involves scrutinizing shared clusters, which are clusters used in multiple track candidates but not identified as merged. Since these shared clusters strongly suggest incorrect assignments, a limit on the maximum number shared clusters is enforced.

To aid in identifying merged clusters, an artificial neural network (NN), specifically trained for this purpose, is employed. This NN demonstrates remarkable efficiency, correctly identifying clusters created by two particles about 90% of the time, and those by three charged particles with an efficiency of 85%. Subsequently, track candidates failing to meet a set of basic quality criteria are discarded by the ambiguity solver.

Finally, the tracks are extended through the TRT and high-resolution track fits are performed using additional neural networks to ascertain the position and uncertainty of each cluster. An additional reverse sequence is used which starts to search for tracks in the TRT to find additional tracks.

Each reconstructed track is defined by five parameters: the azimuthal angle ϕ, the polar angle θ, the charge-to-momentum ratio q/p, and two impact parameters, d_0 and z_0. The parameter d_0 denotes the minimum transverse distance to the nominal interaction point, while z_0 represents the closest longitudinal distance. The performance of the ATLAS track reconstruction algorithms in Run 2 is analyzed in Ref. [106].

From the reconstructed tracks vertices corresponding to the collision points in the detector are reconstructed [107]. The reconstruction of vertices unfolds in two main stages: vertex finding and vertex fitting. The initial stage, vertex finding, involves associating reconstructed tracks with potential vertex candidates. In the vertex fitting process the precise position of the vertex and its covariance matrix are reconstructed.

The process begins by selecting a seed position for the first vertex. Utilizing both this seed and the associated tracks, an iterative fit is applied to estimate the best vertex position. During each iteration of this fitting procedure, tracks that are less compatible with the current vertex estimate are progressively down-weighted, and the vertex position is recalculated to refine its accuracy.

Once a stable vertex position has been determined, tracks that do not align well with this vertex are removed. These removed tracks are not discarded but rather made available for the determination of subsequent vertices. The entire procedure is then repeated with the remaining tracks in the event.

Finally, the primary vertex is chosen from the set of vertices with at least two associated tracks. This selection is based on identifying the vertex with the highest sum of squared transverse momenta p_{T}^2 [108]. Events must have at least one vertex associated with a minimum of two inner detector tracks, each having a transverse momentum p_{T} greater than 0.5 GeV. Secondary vertices, located outside the beamspot, are later utilized for B-hadron identification.

Given that the expected size of the beamspot is considerably smaller than the resolution of the primary vertex position in the transverse direction, calculating the transverse impact parameter d_0 of tracks relative to the primary vertex is not necessary. However, the situation differs for the longitudinal position of the primary vertex. In this case, it is beneficial to determine the longitudinal track impact parameter z_0 of the tracks relative to the primary vertex position. This parameter is subsequently denoted as Δz_0.

5.2. Topological clusters

A topological cluster algorithm [109] is used to group energy deposits (hits) recorded in the calorimeters into distinct clusters. The algorithm uses a cell signal significance S, the ratio of the measured cell energy to its average noise value, of $|S| > 4$ to determine seed cells for the clusters. Cells neighboring the clusters are added to the cluster as long as the corresponding cell on the cluster border has a signal significance of $|S| > 2$. If a seed cell neighbors another cluster, or a cell with $|S| > 2$ neighbors another cluster, the two clusters are merged. Topological clusters are not expected to only contain the shower of a single particle in all cases, as often showers from different particles cannot be distinguished. However, they do provide a comprehensive representation of the collective energy signature of significant signals in the calorimeters removing noise from different sources.

5.3. Jet algorithm

Combined information from the inner detector and the calorimeters is used to reconstruct jets. The particle flow algorithm [110] is used matching topological clusters with a selection of well measured tracks and subtracting the energy of the tracks from the matched topological clusters. If the energy of the track is smaller then that of the matched clusters, the energy is subtracted by estimating the energy density profile and subtracting the energy step wise in rings of cells starting with high energy density and going to lower energy density until the energy is completely subtracted. The algorithm further decides if the remaining energy in the topological clusters matched to the track is consistent with a shower fluctuation of a single particle and removes it accordingly.

The remaining topological clusters and the tracks are then combined in a list of entities serving as the input of the algorithm building the jets. Here, the anti-k_T algorithm [111] is used because of several of its advantageous properties. The anti-k_T algorithm is an iterative procedure combining the entities based on the distance measures

$$d_{ij} = \min(p_{\mathrm{T}i}^{-2}, p_{\mathrm{T}j}^{-2})\frac{\Delta R_{ij}^2}{R^2},$$

$$d_{iB} = p_{\mathrm{T}i}^{-2}.$$

where R is a radius parameter determining the size of the jets. An illustration of the anti-k_T algorithm is given in Figure 5.1. The entities, starting from the particles measured in the calorimeters, are merged depending on the smallest d_{ij} and d_{iB}. If a d_{ij} is the smallest, the two respective entities are combined to one, and if a d_{iB} is smallest, the entity is declared a jet and removed from the list of entities. This way jets are conical around high p_T particles and when multiple high p_T particles are close together higher p_T jets have priority over lower p_T jets. This ensures the shapes of the jets from high p_T particles are unaffected by soft radiation. Additionally, the found set of jets is unaffected by additional soft radiation and collinear splittings of particles making the algorithm infra-red and collinear safe. The radius parameter R is set for this analysis to $R = 0.4$.

To suppress jets from pile-up a multivariate combination of track-based variables, the jet-vertex-tagger (JVT) [112], is used. Jets with $p_\mathrm{T} < 60\,\mathrm{GeV}$ and $|\eta| < 2.4$ are required to have a JVT above 0.5. For jets with high pseudorapidity the forward-jet-vertex-tagger (fJVT) [113] is used. Jets with $p_\mathrm{T} < 120\,\mathrm{GeV}$ and $|\eta| > 2.5$ are required to have a fJVT below 0.4 and pass an additional jet timing condition. Differences in the efficiencies of the JVT and fJVT be-

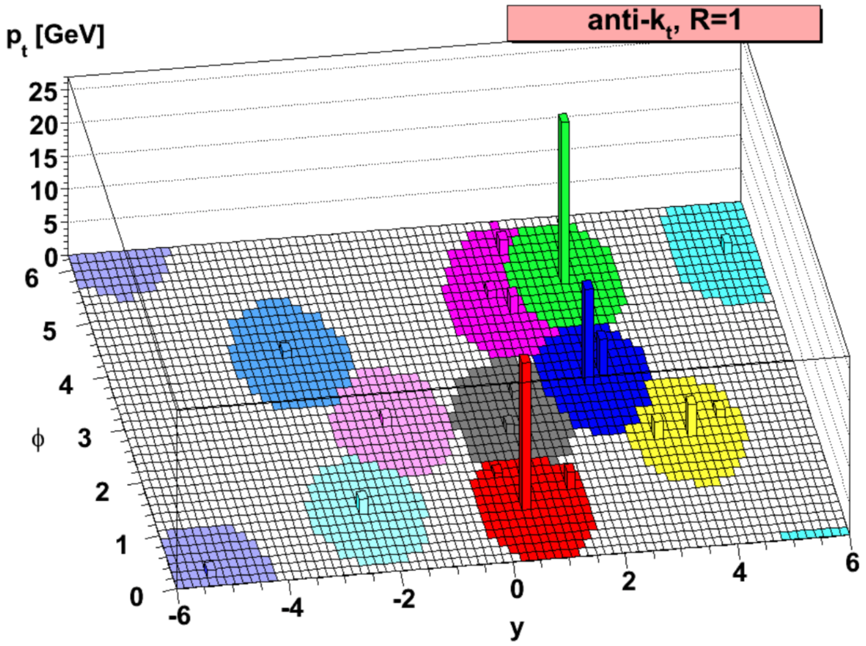

Figure 5.1.: Illustration of the clustering achieved with the anti-k_T algorithm [111].

tween collision data and simulation are corrected by corresponding scale factors.

5.4. Jet Energy Scale

The calibration of jet energy starts with the calibration of the energy deposited in the calorimeter by electrons using test beams, thus establishing the electromagnetic (EM) energy scale. Jets are reconstructed at this EM scale using the jet algorithm. The Jet Energy Scale (JES) correction then adjusts the jet energy to align with the energy of truth jets, defined using the anti-k_T algorithm on stable, final-state particles coming from the initial results of the event simulation before they undergo further interactions or decay. The measurement of the JES correction for jets using the particle flow algorithm is derived in Ref. [114].

The JES calibration comprises multiple stages to address various effects. Initially, the four-momentum of the jets is adjusted to point towards the primary hard scatter vertex, keeping the energy constant, which is essential for accurate jet positioning and energy distribution. Following this, pileup corrections are applied, considering both the jet's transverse momentum and its area. An additional, residual pileup correction considers the average number of interactions per crossing μ and the number of primary vertices N_{PV}.

Subsequently, the jet four-momentum is corrected to the level of jets constructed from final-state truth particles, based on matching in Monte Carlo (MC) simulations. This process is followed by a global sequential calibration using five observable parameters to correct effects from different p_{T} fractions in quark- and gluon-initiated jets.

The final calibration stage, in situ calibration, addresses differences between data and MC simulations due to the detector's response. This multi-step process starts with the η-intercalibration, aligning jets in the forward region with those in the central region in dijet events. The calibration is further refined using Z+jets and γ+jets events to balance the jet with the Z boson or photon. For high p_{T} jets, multijet events calibrate them against well-calibrated low p_{T} jets.

5.5. Electron Reconstruction

Electron candidates are reconstructed from energy clusters in the electromagnetic calorimeter matched to an inner detector track [115–118]. Superclusters are formed out of EM topo-clusters, considering initial seed cluster candidates based on descending E_{T} values. Seed clusters must have $E_{\mathrm{T}} > 1\,\mathrm{GeV}$ and a matched track featuring at least four hits. Adjacent topo-clusters fulfilling specific criteria are identified as satellite candidates, possibly from bremsstrahlung or splitting, and are merged with seed clusters to create superclusters.

Subsequently, superclusters are associated with inner detector tracks to form electron candidates. Clusters are required to be in the range $|\eta_{\mathrm{cluster}}| < 2.47$ and are excluded if they are in the transition region $1.37 < |\eta_{\mathrm{cluster}}| < 1.52$ between the central and the endcap electromagnetic calorimeters. The tracks are required to have a transverse momentum of $p_{\mathrm{T}} > 10\,\mathrm{GeV}$ and are required to point to the primary vertex with a transverse impact parameter significance $|d_0/\sigma_{d_0}| < 5$ and longitudinal impact parameter, Δz_0, to satisfy the requirement $|\Delta z_0 \sin\theta| < 0.5\,\mathrm{mm}$. Here, the factor of $\sin\theta$ is used to account for the larger uncertainty of the impact parameter determination in the forward region.

Electron energy is derived from supercluster energy. A multivariate algorithm is used to account for energy loss outside the supercluster, such as in material in front of the calorimeter. The algorithm is calibrated using simulated single electron event samples. Next, adjustments in data are made accounting for the differences between the calorimeter layers and local non-uniformities in the detector response.

The overall energy scale is corrected in data and the energy resolution is decreased slightly in MC by smearing to agree with data using a sample of Z boson decays into electron-positron pairs. To improve the purity of correctly identified electrons a likelihood discriminant is constructed from quantities from the calorimeters and the inner detector, such as shower shape, number of hits in the inner detector and the likelihood of transition radiation from the TRT. Likelihoods are built as the product of the probability density functions of the input quantities both for prompt electrons and for a background of jets with similar signatures to electrons, electrons from photon conversions and electrons from heavy hadron decays. The signal likelihood and background likelihood are combined to a single discriminant used to place a cut selecting identified electrons.

Finally, to refine the selection of electrons, non-prompt electrons are further excluded through the implementation of an isolation requirement. This involves the use of a multivariate discriminant based on boosted decision trees, known as the prompt lepton BDT [115, 119]. This discriminant integrates electromagnetic shower shapes and track information from the inner detector, along with various metrics describing the isolation of the leptons, to effectively identify and select prompt electrons.

The efficiency of the applied electron trigger, reconstruction, identification and isolation criteria for the used working points is measured in data and simulation [115]. Simulated events are corrected using scale factors to account for differences between data and simulation in these efficiencies.

5.6. Muon reconstruction

Muons are reconstructed by matching tracks in the muon detector with tracks in the inner detector [120, 121]. Tracks in the muon detector are reconstructed as follows. A Hough transformation is used to search for aligned hits in each MDT chamber. A straight line fit is performed to aligned hits to build a track segment using RPC or TGC hits for measuring the coordinate orthogonal to the bending plane. The segments are used as seeds in a combinatorial search algorithm fitting hits from different segments to form a muon track candidate. To build a muon track at least two matching segments are required except for the barrel-endcap region where the requirement is relaxed. Finally, a global χ^2 fit is performed to select the track candidates. Next, the tracks from the muon detector are combined with the inner detector tracks by a matching algorithm. Tracks are required to have a transverse momentum of $p_\mathrm{T} > 10\,\mathrm{GeV}$ and are required to point to the primary vertex with a transverse impact parameter significance $|d_0/\sigma_{d_0}| < 5$ and longitudinal impact parameter, Δz_0, to satisfy the requirement $|\Delta z_0 \sin\theta| < 0.5\,\mathrm{mm}$.

Similarly to the electrons, additional identification criteria are applied to muon candidates to select prompt muons. Non-prompt muons originate mainly from decays of pion and kaon decays in the detector. As such non-prompt muons often have a kink in their reconstructed track. Differences in the track properties in the inner detector and the MS and the normalized χ^2 of the combined track fit are used to select tracks where the track from the inner detector and the track from the muon detector are compatible, reducing the number of selected non-prompt muons. Different identification selection categories are defined in Ref. [121]. The medium identification selection category is used for the selected muons in this analysis, while muons selected in the loose identification selection category are to veto events as described in Chapter 6.

Subsequently, the muon selection process is similarly enhanced by excluding non-prompt muons through an isolation criterion. This refinement utilizes a multivariate discriminant, known as the prompt lepton BDT [119, 120], which is developed using boosted decision trees. It incorporates information on muon track characteristics from the inner detector and muon spectrometer, along with data regarding the isolation of the muons.

The efficiency of the applied muon trigger, reconstruction, identification and isolation criteria for the used working points is measured in data and simulation [120]. Simulated events are corrected using scale factors to account for differences between data and simulation in these efficiencies.

5.7. Flavor-tagging of Jets

For the further analysis it is important to identify jets originating from *b*-quarks (*b*-tagging). Such jets have several properties that can be exploited to differentiate them from jets coming from light quarks or gluons. One useful indicator is the vertex the tracks of the jets converge on. Jets originating from a bottom quark in the hard scattering final state are characterized by a B-hadron which travels a short distance away from the interaction point until it decays further. The properties of the secondary vertices and impact parameters of the tracks are used to identify jets originating from *b*-quarks. For this purpose multiple algorithms were developed and later combined.

The `IP3D` algorithm [122] utilizes track information for *b*-tagging, focusing on the transverse impact parameter significance (d_0/σ_{d_0}) and longitudinal impact parameter significance ($z_0 \sin\theta / \sigma_{z_0 \sin\theta}$), which are employed in a log-likelihood ratio.

Complementing this, the `SV1` algorithm [123] reconstructs secondary vertices using an iterative χ^2 fitting procedure. Further, the `JetFitter` algorithm [124] reconstructs the entire B-hadron decay chain and employs a BDT to combine various reconstructed observables for jet classification.

These algorithms' outputs are then integrated into the deep feed-forward neural network `DL1r`. The `DL1r` network, a variation of the `DL1` algorithm [125], incorporates an additional Recurrent Neural Network [126] as input. For the identification of b-tagged jets, a threshold is set on the `DL1r` network output, corresponding to a b-tagging efficiency of 60 % for b jets in a sample of $t\bar{t}$ events.

Differences in the b-tagging efficiency between collision data and simulation are corrected using simulation-to-data scale factors derived from $t\bar{t}$ events and consistent with unity. The scale factors depend on the p_{T} of the jets and are corrected for different parton-shower generators using additional MC-MC scale factors.

5.8. Missing transverse momentum

Neutrinos produced in the interaction, travel through the detector without interacting with it, making a direct detection impossible. However, by adhering to the principle of momentum conservation, the sum of transverse momenta $\vec{p}_{\mathrm{T}}$ of all particles originating from the hard scattering should be zero. Thus, by examining the total measured momenta of all particles involved in the interaction, the magnitude and direction of the missing transverse momentum $\vec{p}_{\mathrm{T}}^{\,\mathrm{miss}}$ can be deduced. Specifically, for the t-channel process, this missing transverse momentum corresponds to the neutrino's transverse momentum, enabling the full reconstruction of the top quark as discussed in Section 6.3.

To determine the missing transverse momentum, all momenta of the reconstructed leptons and jets, and well-measured inner detector tracks that point to the primary vertex but are not associated with a reconstructed object are summed [127]. However, signals from the calorimeters that are not part of reconstructed particles are excluded due to their high contamination from pileup. To accurately determine the missing transverse momentum, it is therefore necessary to analyze data from all subdetectors.

By convention, the magnitude of the missing transverse momentum $\vec{p}_{\mathrm{T}}^{\,\mathrm{miss}}$ is denoted as $E_{\mathrm{T}}^{\mathrm{miss}}$.

5.9. Overlap Removal

In the object reconstruction process the same subdetector information is often utilized multiple times to reconstruct various objects. To avoid the double-counting of objects that are reconstructed from identical detector signals, an overlap removal procedure is implemented. This procedure uses objects meeting loose quality criteria and follows a systematic sequence:

Firstly, electrons that share an inner detector track with a muon are removed. This ensures that there's a clear distinction between the electron and muon categories.

Next, jets positioned within a $\Delta R = 0.2$ radius from an electron are eliminated. This is important to avoid mistakenly counting electron energy deposits as jets, which could distort the energy scale by double counting the energy of objects.

Subsequently, electrons found within a $\Delta R = 0.4$ radius from any remaining jet are removed. This targets the reduction of non-prompt electrons that may arise from photon conversions or semileptonic decays within jets.

For muons, any jets within a $\Delta R = 0.2$ radius are discarded if they are associated with two or fewer tracks. This ensures that authentic muon signals are not confused with proximate jet activity.

Finally, muons located within a $\Delta R = 0.4$ radius of any remaining jet are also removed. This step is designed to decrease the inclusion of non-prompt muons that could be produced from hadron decays within the jet.

By adhering to this procedure, the analysis effectively guarantees that each reconstructed object is distinctly classified, thereby minimizing ambiguities and potential biases in the resulting data.

6. Event Selection

In the event selection phase, properties of the reconstructed physical objects are utilized to select events that match the expected signal signature. The primary aim here is not solely to maximize the signal fraction but to establish a solid basis for further analysis by efficiently filtering out easily distinguishable background events. This selection hinges on the characteristic signature of the *t*-channel signal process in the detector. At the tree level, the signal's final state includes the decay products of the top quark along with the light spectator quark. In the leptonic channel, the top quark decays into a bottom quark, a neutrino, and a lepton.

The criteria for event selection require exactly one lepton (ℓ), representing the lepton from the leptonic decay of the W boson. The analysis deliberately excludes the hadronic decay channel due to its substantial multijet background, which poses significant challenges in effectively distinguishing the signal process. Furthermore, events must have exactly two jets: one corresponding to the light spectator quark from the *t*-channel process, and the other associated with the jet resulting from the top-quark decay. Exactly one of these jets is required to be *b*-tagged, indicative of its origin from a bottom quark decay in the *t*-channel process. The *b*-tagged jet is denoted as b, and the untagged jet as j.

The spectator bottom quark, not originating from the top quark decay, usually has low transverse momentum (p_{T}), resulting in its omission from the jet count. This specific trait plays a crucial role in substantially minimizing the dominant $t\bar{t}$ background via the jet counting selection criteria. In the case of the $t\bar{t}$ background, both b quarks are likely to produce a *b*-tagged jet. Therefore, the selection criterion of having exactly one *b*-tagged jet effectively helps in excluding events with $t\bar{t}$ background. Additionally, events with forward jets within $2.3 < |\eta| < 4.5$ and $30\,\mathrm{GeV} < p_{\mathrm{T}} < 35\,\mathrm{GeV}$ are removed, which improves the agreement between the simulation and data in the pseudorapidity distribution of these jets.

A cut on the missing transverse momentum of $E_{\mathrm{T}}^{\mathrm{miss}} > 30\,\mathrm{GeV}$ is added, consistent with the expectation of a neutrino coming from the leptonic W decay. The transverse mass of the W boson is the invariant mass of its decay products assuming they have no momentum in beam direction. It is defined as

$$m_{\mathrm{T}}\left(W\right) = \sqrt{2 p_{\mathrm{T}}(\ell) E_{\mathrm{T}}^{\mathrm{miss}} \left(1 - \cos \Delta\phi \left(\vec{p}_{\mathrm{T}}^{\mathrm{miss}}, \ell\right)\right)}$$

where $\Delta\phi \left(\vec{p}_{\mathrm{T}}^{\mathrm{miss}}, \ell\right)$ is the difference in the azimuthal angles of the lepton and $\vec{p}_{\mathrm{T}}^{\mathrm{miss}}$. The transverse mass is invariant under Lorentz boosts in the direction of the beam pipe and peaks at the W-boson mass given the process involves an on-shell W-boson and the decay products are correctly measured. A cut on the transverse mass of $m_{\mathrm{T}}(W) > 50\,\mathrm{GeV}$ is used to reduce multijet events, which lack a W boson and tend to lower values in $m_{\mathrm{T}}(W)$.

To further reduce the multijet background, a triangular cut is applied, removing events with low lepton p_{T} based on the difference in azimuthal angle between the lepton and the jet with the highest p_{T}, denoted by j_1:

$$p_{\mathrm{T}}(\ell) > 40 \cdot |\Delta\Phi(j_1, \ell)/\pi|$$

A cut on $m(\ell b)$ is implemented to exclude regions of phase space where the top quark is not produced in an on-shell state, aligning with the MC simulation's assumption that the top quark is produced on-shell. The kinematic limit of $m(\ell b)$ for on-shell top-quark production is given by the equation $m(\ell b)^2 = m_t^2 - m_W^2$ [35]. Consequently, a requirement that $m(\ell b) < 160\,\mathrm{GeV}$ is enforced.

Following these selection criteria, events are categorized into two signal regions, SR `plus` and SR `minus`, based on the charge of the selected lepton, enabling sensitivity to R_t. The number of selected events in the defined analysis regions is given in Table 6.1 and the composition of the SRs is visualized in Figure 6.1. The multijet process is normalized to values obtained from the preliminary multijet estimate described in the following Section 6.1.

The applied selection criteria result in a signal fraction of 21 % in the SR `plus` and 16 % in the SR `minus`. It is important to note that a higher signal fraction is not necessarily more advantageous for subsequent analysis, especially considering the additional use of a neural network to distinguish signal events from background events. The focus, instead, is on constraining the phase space to regions where the majority of the signal is concentrated. This approach allows for a more effective definition of the kinematic properties that will be used later to further differentiate between signal and background events. The predominant background contributions in the SRs are from $t\bar{t}$ and W+jets events.

Table 6.1.: The yields in the two SRs. All uncertainties applied in the analysis are included.

Process	SR `plus`	SR `minus`
tq	$167\,000 \pm 8000$	150 ± 150
$\bar{t}q$	90 ± 90	$105\,000 \pm 5000$
$tW + \bar{t}W, t\bar{b} + \bar{t}b$	$52\,000 \pm 4000$	$51\,000 \pm 4000$
$t\bar{t}$	$281\,000 \pm 31\,000$	$281\,000 \pm 31\,000$
W+$b\bar{b}$, light	$180\,000 \pm 70\,000$	$130\,000 \pm 50\,000$
W+$c(\bar{c})$	$59\,000 \pm 14\,000$	$55\,000 \pm 13\,000$
Z+jets, diboson	$19\,000 \pm 4000$	$18\,000 \pm 4000$
Multijet	$48\,000 \pm 10\,000$	$47\,000 \pm 10\,000$
Total	$800\,000 \pm 80\,000$	$690\,000 \pm 60\,000$
Observed	814 185	698 845

6.1. Preliminary Multijet Estimation

Neither the jet-electron method nor the anti-muon method offers an estimate for the quantity of multijet events. Consequently, the overall normalization of these samples is determined concurrently with the signal parameters in the analysis. To assess the agreement of distributions between MC and data prior to the main fit of the analysis, a preliminary multijet fit is conducted to estimate the normalization

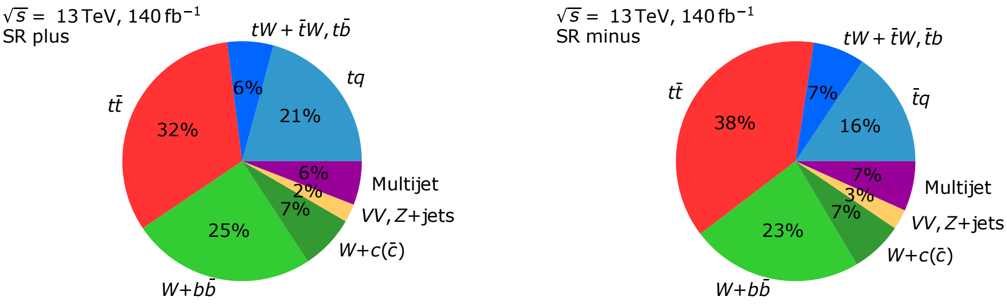

(a) SR plus

(b) SR minus

Figure 6.1.: Pie charts visualizing the composition of the SRs in terms of the defined processes. SR plus is shown on the left and SR minus is shown on the right.

Table 6.2.: Multijet yields from the preliminary multijet fit. The given uncertainties only include the statistical uncertainty.

	barrel e^+	end-cap e^+	μ^+	barrel e^-	end-cap e^-	μ^-
Multijet	$27\,700 \pm 1400$	$10\,800 \pm 500$	1870 ± 110	$27\,900 \pm 1400$	$10\,900 \pm 500$	1900 ± 110
Total	$319\,900 \pm 500$	$82\,770 \pm 260$	$12\,020 \pm 90$	$282\,500 \pm 500$	$67\,600 \pm 230$	9710 ± 90
Multijet/Total	9%	13 %	16%	10 %	16%	20%

of the multijet background.

For this initial fit, regions are defined split in positive and negative lepton channels, as well as electron and muon channels. Additionally, the electron regions are further divided by pseudorapidity of the lepton into regions with $|\eta| < 1.37$ (barrel) and with $|\eta| > 1.52$ (end-cap). In the fit the normalization for each of the multijet subprocesses, `mj` e, `mj` fe and `mj` μ is determined by separate normalization factors. For the electron channel the full $E_{\mathrm{T}}^{\mathrm{miss}}$ distribution is used removing the $E_{\mathrm{T}}^{\mathrm{miss}} > 30\,\mathrm{GeV}$ cut and for the muon channel the $\Delta\Phi(\vec{p}_{\mathrm{T}}^{\mathrm{miss}}, \mu)$ distribution is used in a region enriched in muon multijet events by inverting the multijet veto cut:

$$p_{\mathrm{T}}(\mu) < 40 \cdot |\Delta\Phi(j_1, \mu)/\pi|$$

The preliminary multijet fit is performed using only the statistical data uncertainty and the statistical MC uncertainties. All other processes including the signal processes are set to their SM expectation values. Figure 6.2 shows the post-fit agreement between data and simulation in the included regions and Table 6.2 shows the corresponding yields and multijet fractions determined in the fit.

6.2. Multijet Background Control Regions

For the statistical analysis the normalization of the multijet background is determined in additional control regions (CRs) that are orthogonal to the SRs but are kinematically close to the definition of the SRs. To get a good determination of the multijet normalizations it is advantageous to have many events and a high multijet fractions in the CRs. Therefore sensible choices for the definition of the CRs are the inversion of cuts that aim to remove multijet in the SR. In the statistical analysis all SRs and CRs are used in a simultaneous fit. This way the uncertainty of the normalization of the multijet process is included in the fit by construction.

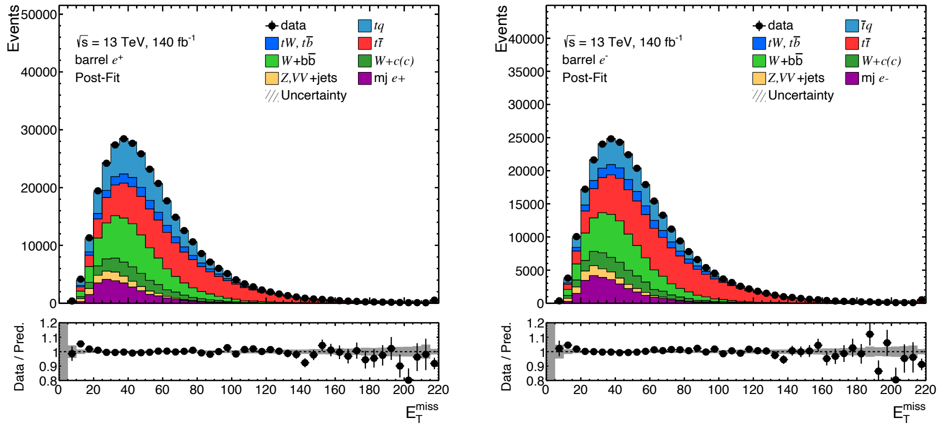

(a) barrel e^+ (b) barrel e^-

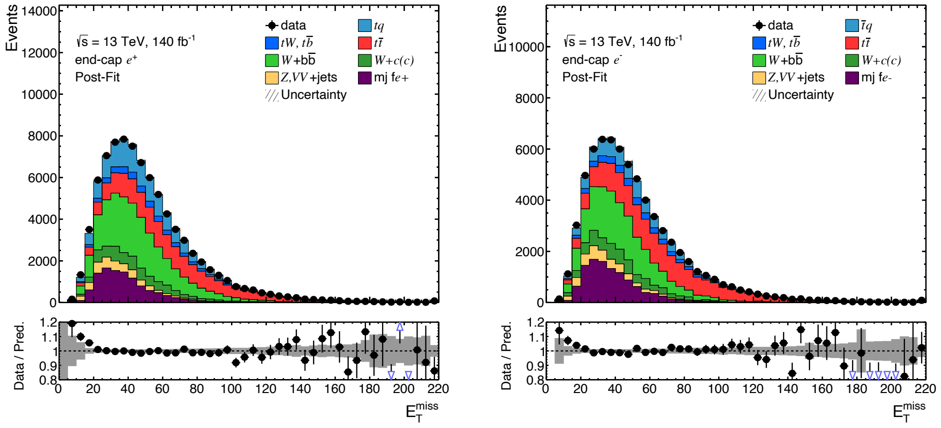

(c) end-cap e^+ (d) barrel e^-

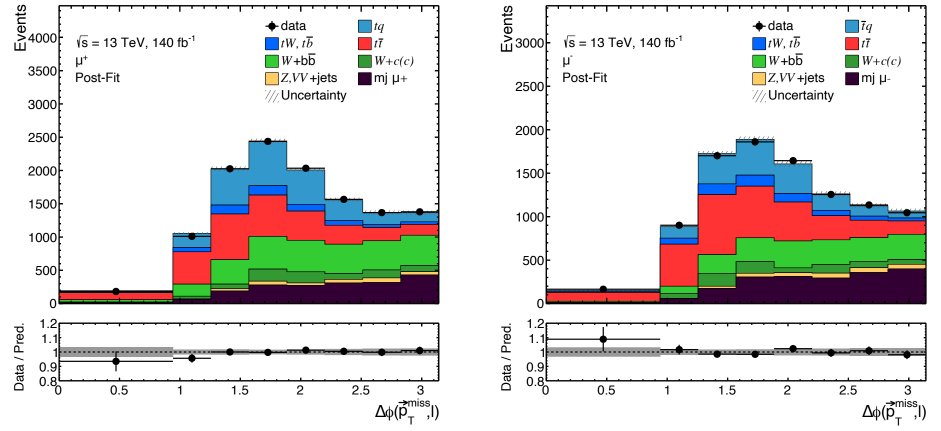

(e) μ^+ (f) μ^-

Figure 6.2.: Distributions used in the preliminary multijet estimate showing the agreement between data and MC prediction after the fit.

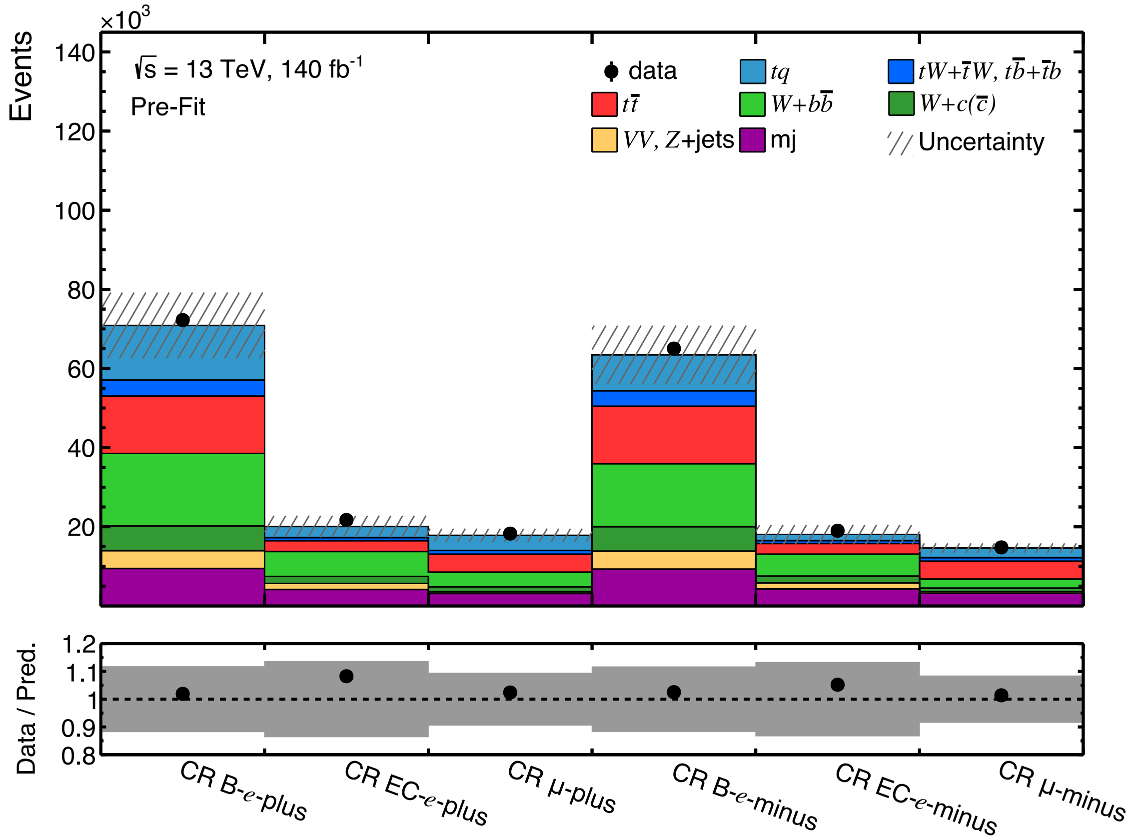

Figure 6.3.: Yields in the CRs comparing data and simulation. The uncertainty band represents the combined MC uncertainty. The bottom plot displays the ratio of observed events to the predicted count for each region.

Like in the preliminary multijet fit the muon CRs for the further statistical analysis are defined by the inversion of the triangular multijet veto cut

$$p_{\mathrm{T}}(\ell) < 40 \cdot |\Delta\Phi(j_1, \ell)/\pi|.$$

Two multijet CRs are defined, CR μ-`plus` containing positively charged muon events, and CR μ-`minus` containing negatively charged muon events. Electron CRs are defined by inverting the requirement on $E_{\mathrm{T}}^{\mathrm{miss}}$. The electron CRs are further divided by lepton charge and pseudorapidity of the lepton into regions with $\eta < 1.37$ (barrel) denoted CR `B-e-plus` and CR `B-e-minus` and with $\eta > 1.52$ (end-cap) denoted CR `EC-e-plus` and CR `EC-e-minus`.

The yield of data compared to simulation with the multijet process scaled to the values determined in the preliminary multijet fit is shown in Figure 6.3.

6.3. Reconstruction of the Top Quark

Reconstructing the top quark is necessary for defining kinematic variables, such as the invariant mass of the top quark. This reconstruction involves summing the four-momenta of the decay products of the top quark:

$$p(W) := p(\nu) + p(\ell)$$

$$p(t) := p(W) + p(b)$$

While the four-momenta of the lepton $p(\ell)$ and the b-quark $p(b)$ are already determined, the neutrino's four-momentum $p(\nu)$ presents a challenge, as only its transverse component is directly measurable as the missing transverse momentum $\vec{p}_{\mathrm{T}}^{\mathrm{miss}}$. The z-component of $p(\nu)$ can be reconstructed using the well-established mass of the W boson as a constraint:

$$80.4\,\mathrm{GeV} = m_W = \sqrt{p(W)^2}$$

This constraint leads to a quadratic equation for the z-component of $p(\nu)$, typically resulting in two possible solutions. The smaller of these two solutions is selected.

However, situations arise where the transverse mass of the reconstructed W boson ($m_{\mathrm{T}}(W)$) is less than the mass of the W boson due to uncertainties in the measurement of the $\vec{p}_{\mathrm{T}}^{\mathrm{miss}}$. In such cases, where the quadratic equation yields no real solutions, a correction procedure [128] is employed for the measured $\vec{p}_{\mathrm{T}}^{\mathrm{miss}}$. Initially, $m_{\mathrm{T}}(W)$ is constrained to the mass of the W boson, yielding a single solution for $p_z(\nu)$. Subsequently, the x and y components of $p(\nu)$ are adjusted to maintain the mass constraint of $80.4\,\mathrm{GeV} = m_W$. This adjustment results in two new solutions, from which the one is selected that minimizes the difference between the measured and modified values of $p_x(\nu)$ and $p_y(\nu)$.

7. Neural Network

A neural network is employed to further distinguish between signal and background events in the SRs by combining the information from several kinematic variables. Its architecture is that of a feed-forward network, featuring one hidden layer and a single output node which categorizes events into signal or background events. As a software implementation NeuroBayes [129, 130] is used.

The feed-forward neural network employed in this analysis is a linear progression model, processing data linearly from input to output without cycles. The architecture of the neural network is depicted in Figure 7.1. The process begins combining input variables v_i into weighted sums,

$$h_j = f\left(\sum_i w_{1i} v_i\right),$$

to form the nodes in the hidden layer. In these sums, each input variable is multiplied by a unique weight w_{1i}, which is optimized during the training. The resultant weighted sums at each node are subsequently processed through an activation function f, introducing non-linearity into the model. A sigmoid function

$$f(x) = \frac{2}{1+e^{-x}} - 1$$

is chosen as the activation function. This function is point symmetric around zero treating negative and positive values equally. It is differentiable and maps input values into a bound output range between -1 and 1.

Following the activation function, the hidden layer nodes are further combined using another weighted sum

$$D_{\mathrm{nn}} = f\left(\sum_j w_{2i} h_j\right)$$

to produce a single output value for each event.

Neural networks and other methods available for signal separation, such as boosted decision trees [131], typically yield better results than simple cut-based

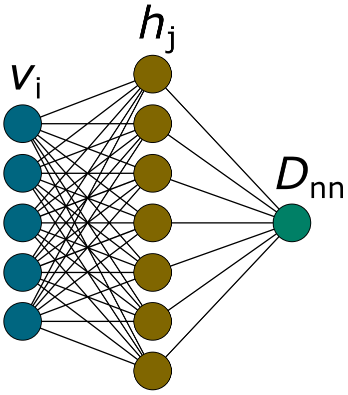

Figure 7.1.: Schematic structure of the feed forward neural network.

analyses. Although boosted decision trees are often preferred for their simplicity and robustness, the neural network implemented in NeuroBayes demonstrates exceptional robustness in training, owing to the advanced, automated preprocessing procedures it incorporates.

The training process for the feed-forward network involves refining the weights to minimize a loss function characterizing the difference between the network's prediction o_i and the target value T_i, which is defined as one for signal and minus one for background events. For this analysis the entropy loss function

$$E_D = \sum_i \ln\left(\frac{1}{2}\left(1 + T_i \cdot o_i + \epsilon\right)\right)$$

is employed which is often preferred for classification problems. Here, ϵ is a small value to avoid numerical issues in the beginning of the training process and is reduced to zero as the training continues. The minimization is performed by employing a backpropagation algorithm, which computes the gradient of the loss function with respect to the weights. The weights are adjusted iteratively by an algorithm reducing the loss function until a minimum is found. Here, the Broyden-Fletcher-Goldfarb-Shanno (BFGS) algorithm, a quasi-Newton method, is chosen for its efficiency in handling large datasets and its capability to converge rapidly to a solution. The BFGS algorithm estimates the Hesse matrix in addition to the gradient to make more efficient steps towards the minimum. Specifically, a limited memory implementation [132] of the algorithm with bound constraints is used.

The network architecture chosen for this analysis consists of a single hidden layer containing 22 nodes. A bias node is included to allow for more flexible function mapping, enhancing the network's capability to fit the training data. The input layer consists of 17 distinct kinematic variables, each representing specific physical quantities derived from the reconstructed events.

The kinematic variables chosen as input are not directly fed into the neural network. Instead, the variables first undergo a transformation procedure within NeuroBayes. This procedure aims to reformat the information of the variables in a manner that's more suitable for neural network processing.

Initially, the distribution of both signal and background events is ascertained for each variable. The distributions are binned, ensuring that each bin contains approximately an equal number of total events. Following this, for every bin, the signal purity, which is the fraction of signal events, is computed. Subsequently, a spline function is fitted to these signal purity values. The spline function's value at any given input variable directly corresponds to the estimated signal purity for that specific variable value.

Subsequent to this, a series of two transformations are administered to the input variables. For each event, the variable's value is transformed via its respective spline function, replacing it with the corresponding signal purity value. Each variable's signal purity distribution is then analyzed determining its mean and standard deviation, and for each variable a linear transformation is applied changing its distribution to have a mean of zero and a standard deviation of one.

In the final step, the set of variables undergoes transformation through a linear map, resulting in a decorrelated set of variables. Initially, the covariance matrix of the input variable vector is computed. Subsequently, the orthogonal transformation that diagonalizes this matrix is determined and then applied as a coordinate transformation to the input variable vector. The processed input variables exhibit a mean of zero, a standard deviation of one, and are not linearly correlated with each other. This approach prevents the neural network from having to learn the linear correlations among the variables, thereby reducing the complexity of the training process.

To avoid overfitting and to ensure a generalized model, Bayesian regularization is applied to the weights. This technique introduces a penalty in the loss function for large weights of the form

$$E_W = \alpha_1 \sum_i \frac{1}{2} w_{1i}^2 + \alpha_2 \sum_i \frac{1}{2} w_{2i}^2$$

where α_1 and α_2 are regularization parameters adjusted by NeuroBayes and w_{1i} are the weights in the first layer and w_{2i} are the weights in the second layer of the network. Such a regularization ensures the model remains robust and less sensitive to individual data fluctuations.

7.1. Input Variables

The neural network employs 17 distinct input variables, each representing physical quantities derived from the reconstructed events. These variables, summarized in Table 7.1 serve as discriminants to separate signal from background events. Here, an overview of these variables is provided, along with accompanying figures illustrating their distribution in both MC simulations and observed data. It is important to check the adequate modeling of all input variables to avoid biases in the neural network's predictions.

The 17 variables were chosen from a vast pool of potential quantities. For this selection, a procedure within NeuroBayes was employed. This procedure ranks the variables by assessing their correlation with the target variable. The method incorporates an iterative algorithm. Initially, the cumulative correlation of all variables to the target is determined. Following this, the variable that, when removed, causes the least reduction in total correlation is eliminated. This elimination process is repeated until all variables have been removed.

The magnitude of total correlation reduction serves as a metric of the importance of the individual variables, with the last remaining variable deemed the most crucial. The number of used input variables was determined based on studies examining the signal uncertainty in the subsequent statistical analysis for varied numbers of input variables in the neural network. It was found that beyond approximately 15 variables, the improvements in reducing the uncertainty plateaued. The Figures 7.2 to 7.4 showcase the shapes of the signal process and the main background processes for each variable in MC compared to the data.

The highest ranked variable is the invariant mass of the two jets $\mathrm{m}(jb)$. Invariant mass is defined as $m(x) = x_\mu x^\mu$ making it Lorentz invariant and insensitive of the momentum fractions carried by the colliding partons. In the t-channel process, this variable typically exhibits higher values compared to the background processes. This can be attributed to the high overall momentum of the light jet produced alongside the top quark in the t-channel process. The $\mathrm{m}(jb)$ captures this high momentum by relating it to the usually centrally produced b jet. The second highest ranked variable is the pseudorapidity of the light jet, $|\eta(j)|$. This observable captures the forward direction in which the light jet is produced within the t-channel process. For the main background processes the $|\eta(j)|$ peaks at lower values. The variables $|\Delta\eta(\ell, j)|$, $|\Delta R(\ell, j)|$ and $|\Delta\eta(b, j)|$ add to the description of the light jet by relating it to the lepton and b tagged jet. Collectively, these variables capture the distinctive properties of the light jet produced alongside the top quark in the t-channel.

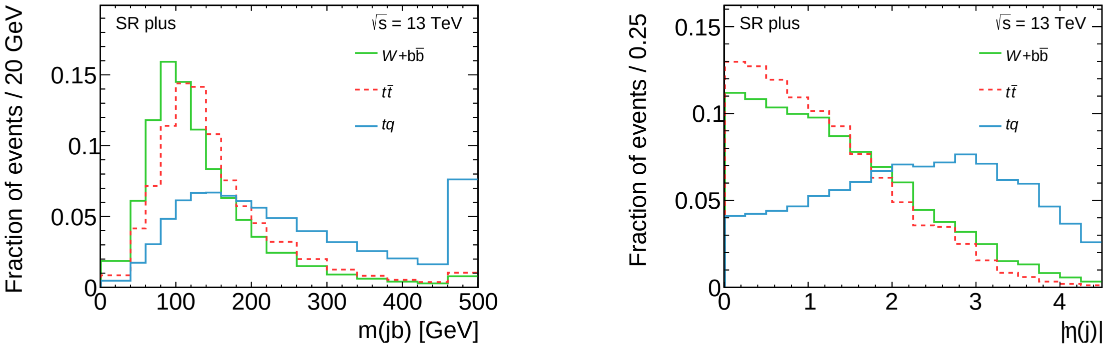

(a) $\mathrm{m}(jb)$ (b) $|\eta(j)|$

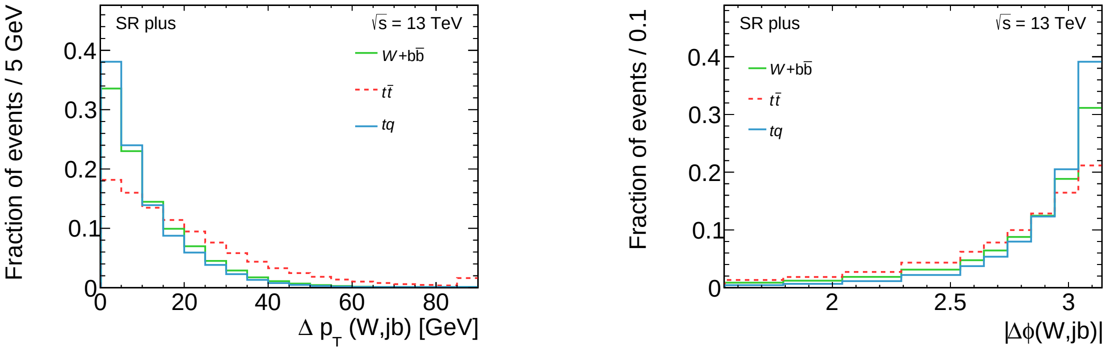

(c) $|\Delta p_{\mathrm{T}}(W, jb)|$ (d) $|\Delta\phi(W, jb)|$

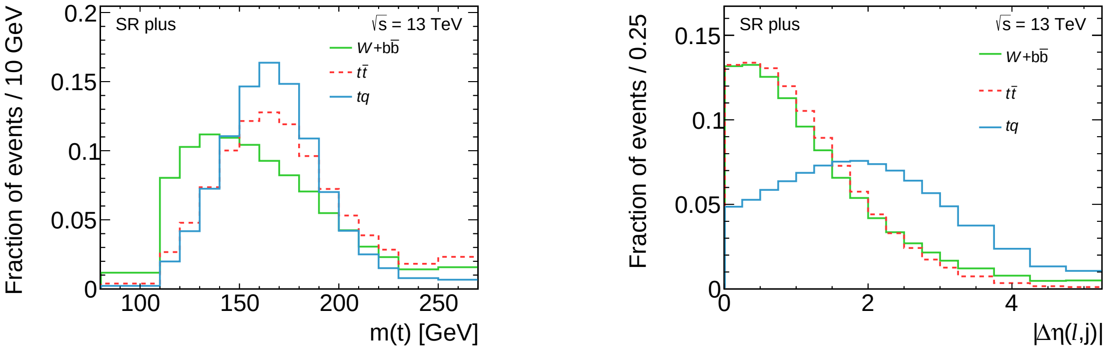

(e) $m(t)$ (f) $|\Delta\eta(\ell, j)|$

Figure 7.2.: Shape of the simulated distributions of the signal process and the main background processes the first six input variables.

The invariant mass of the reconstructed top quark, $m(t)$, peaks at the top quark mass for the signal process where the reconstructed top-quark corresponds to a real top quark. For the $t\bar{t}$ process, the distribution is broader since the b-tagged jet can belong to the other top quark, not the one decaying to the selected lepton.

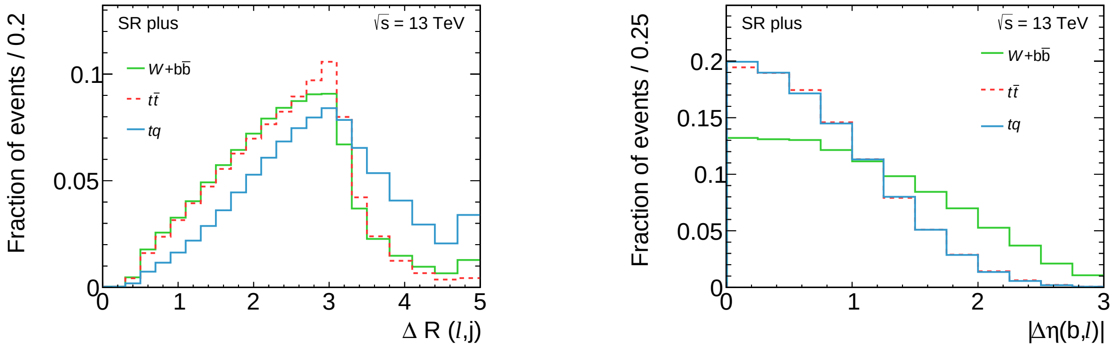

(a) $\Delta R(\ell, j)$ (b) $|\Delta\eta(b, \ell)|$

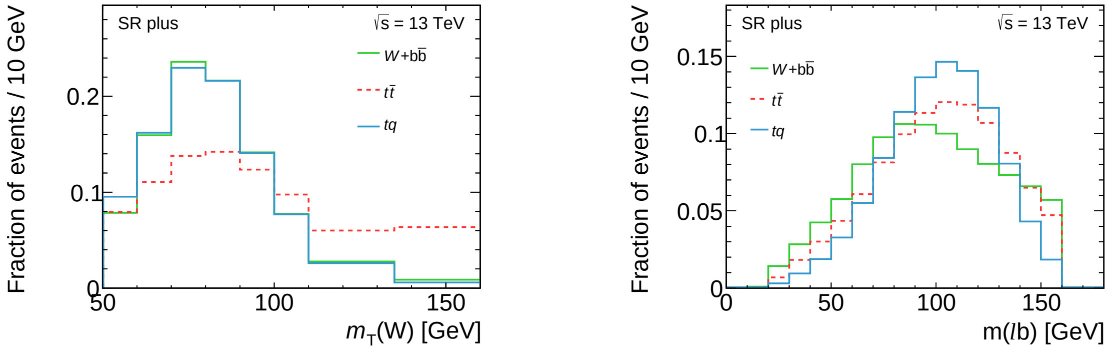

(c) $m_{\mathrm{T}}(W)$ (d) $m(\ell b)$

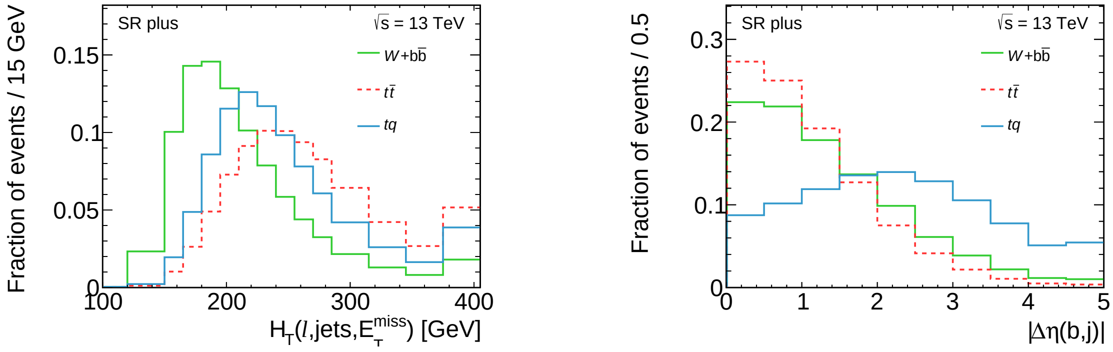

(e) H_{T} (f) $|\Delta\eta(b, j)|$

Figure 7.3.: Shape of the simulated distributions of the signal process and the main background processes for the seventh to twelfth input variable.

In the W+jets process, the distribution peaks at a lower value and is broader because the reconstructed top quark there does not correspond to a real top quark. The spin correlation of the initial state light quark and the final state lepton is exemplified by the angle of the spectator light quark and the lepton

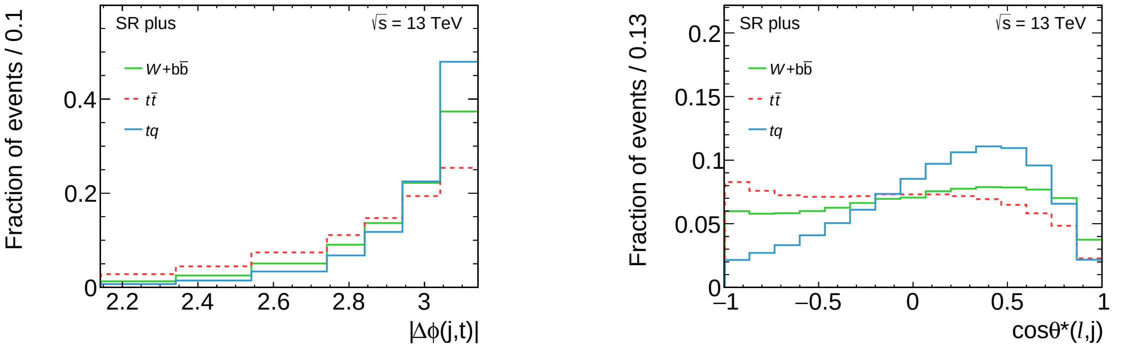

(a) $|\Delta\phi(j,t)|$

(b) $\cos\theta^*(\ell,j)$

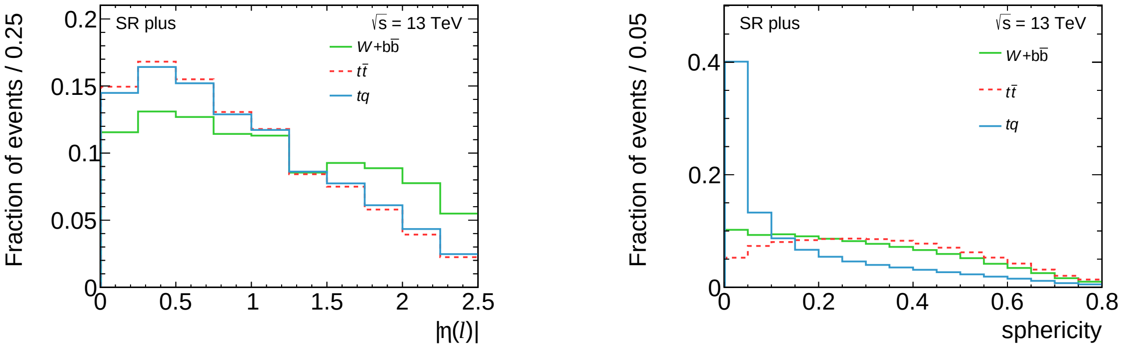

(c) $|\eta(\ell)|$

(d) sphericity

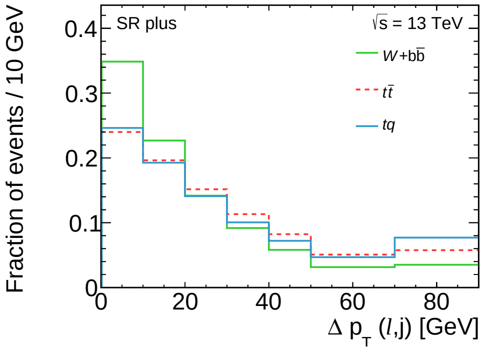

(e) $|\Delta p_{\mathrm{T}}(\ell,j)|$

Figure 7.4.: Shape of the simulated distributions of the signal process and the main background processes for the last five input variables.

in the top rest frame $\cos\theta^*(\ell,j)$ as explained in Section 1.15. Due to the spin correlation, in the signal process a strong dependence on the angle is found. In the main background processes the distribution is found to be flatter. The variables $|\eta(\ell)|$ and $|\Delta\eta(b,\ell)|$ describing the pseudorapidity of the visible top-quark decay products and their relation are valuable in differentiating the W+jets background process from both the signal and $t\bar{t}$ processes, due to broader distributions of the former.

Sphericity is determined by adding the second and third largest eigenvalues of the sphericity tensor and multiplying the result by 3/2. The sphericity tensor itself is defined as

$$S^{\alpha\beta} = \frac{\sum_i p_i^\alpha p_i^\beta}{\sum_i |\vec{p}_i|^2},$$

where α and β denote the spatial components x, y, and z, and p_i represents the three-momenta of the reconstructed objects: the two jets, the charged lepton, and the reconstructed neutrino. For the signal process, the sphericity distribution peaks at zero, whereas the main backgrounds present significantly broader distributions.

In $t\bar{t}$ events selected in this analysis, usually one of the top quarks decays leptonically while the other one decays hadronically. This allows for different combinations of which top quark the selected jets belong to. This in turn leads to broader distributions of the $t\bar{t}$ process in $|\Delta p_\mathrm{T}(W, jb)|$ and $|\Delta\phi(W, jb)|$ than the other main backgrounds and the signal process. The distribution of $m_\mathrm{T}\,(W)$, as defined in Chapter 6, peaks at the mass of the W boson provided that the process involves a W boson decay and the decay products are accurately identified. Consequently, the shape of $m_\mathrm{T}\,(W)$ is similar for both tq and $W + b\bar{b}$ processes. However, in the case of $t\bar{t}$ events, where two W bosons are involved, $m_\mathrm{T}\,(W)$ exhibits a broader distribution due to the presence of decays from two W bosons.

Figures 7.5 to 7.7 show the comparison between the total MC predictions and the data for each input variable to the neural network in the positive signal region. The analogous comparisons for the negative signal region are presented in Appendix A. For each distribution, a test statistic that conforms to a χ^2 distribution is calculated to evaluate the agreement between MC predictions and observed data. This calculation includes all systematic uncertainties, as detailed in Chapter 8. The test statistic is defined by the Mahalanobis distance:

$$\chi^2 = (\boldsymbol{n}_\mathrm{pred} - \boldsymbol{n}_\mathrm{data})^\mathrm{T} S^{-1} (\boldsymbol{n}_\mathrm{pred} - \boldsymbol{n}_\mathrm{data})$$

In this formula, $\boldsymbol{n}_\mathrm{pred}$ denotes the vector of predicted event counts in the histogram bins, while $\boldsymbol{n}_\mathrm{data}$ represents the vector of observed data event counts in these bins. S^{-1} is the inverse of the covariance matrix for the bin values, incorporating all uncertainties and bin-to-bin correlations of the predicted event counts. Finally, a p-value is calculated to quantify the probability that the observed differences between the MC predictions and the data could occur by chance, assuming the model accurately describes the underlying process. This statistical measure helps in assessing the level of agreement between the theoretical predictions and the data.

For this comparison the multijet normalization is set to the values determined in the preliminary multijet fit. All other processes are scaled to their SM prediction. Good agreement is found between data and MC prediction in all variables indicating adequate modeling of the distributions by the simulation.

Rank	Variable	Description
1	$m(jb)$	Invariant mass of the untagged jet and b-tagged jet
2	$\lvert\eta(j)\rvert$	Pseudorapidity of the untagged jet
3	$\lvert\Delta p_{\mathrm{T}}(W, jb)\rvert$	Transverse momentum difference of the W boson and jet pair
4	$\lvert\Delta\phi(W, jb)\rvert$	Azimuthal angle difference of the W boson and jet pair
5	$m(t)$	Invariant mass of the reconstructed top quark
6	$\lvert\Delta\eta(\ell, j)\rvert$	Pseudorapidity difference of the charged lepton and untagged jet
7	$\Delta R(\ell, j)$	Angular distance of the charged lepton and untagged jet
8	$\lvert\Delta\eta(b, \ell)\rvert$	Pseudorapidity difference of the b-tagged jet and charged lepton
9	$m_{\mathrm{T}}(W)$	Transverse mass of the W boson
10	$m(\ell b)$	Invariant mass of the charged lepton and b-tagged jet
11	H_{T}	Scalar sum of the transverse momenta of the charged lepton, jets and $E_{\mathrm{T}}^{\mathrm{miss}}$
12	$\lvert\Delta\eta(b, j)\rvert$	Pseudorapidity difference of the two jets
13	$\lvert\Delta\phi(j, t)\rvert$	Azimuthal angle difference of the untagged jet and top quark
14	$\cos\theta^{*}(\ell, j)$	Cosine of the angle between the charged lepton and untagged jet in the top quark rest frame
15	$\lvert\eta(\ell)\rvert$	Pseudorapidity of the charged lepton
16	S	Sphericity defined as $3/2$ times the sum of the 2nd and 3rd largest sphericity tensor eigenvalues
17	$\lvert\Delta p_{\mathrm{T}}(\ell, j)\rvert$	Transverse momentum difference of the charged lepton and untagged jet

Table 7.1.: The 17 variables used as input to the neural network, ranked by their discriminating power.

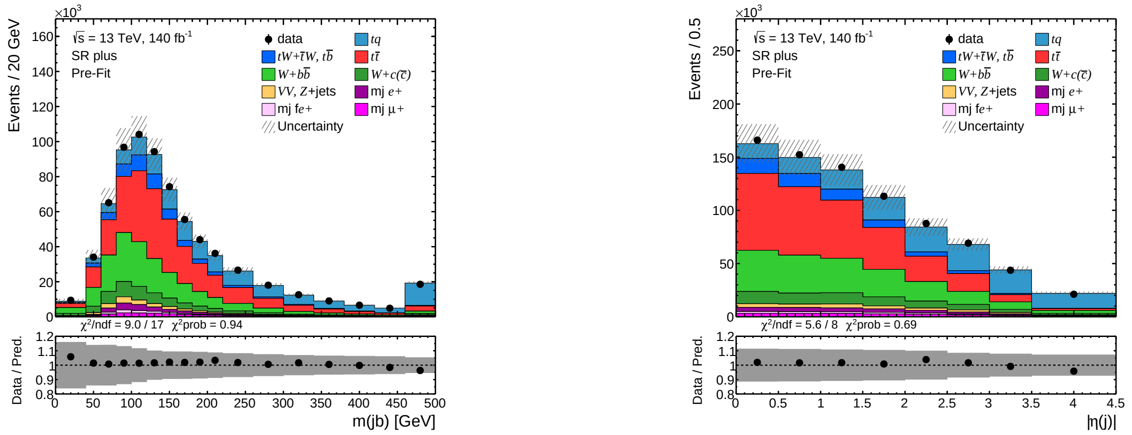

(a) m(jb) (b) $|\eta(j)|$

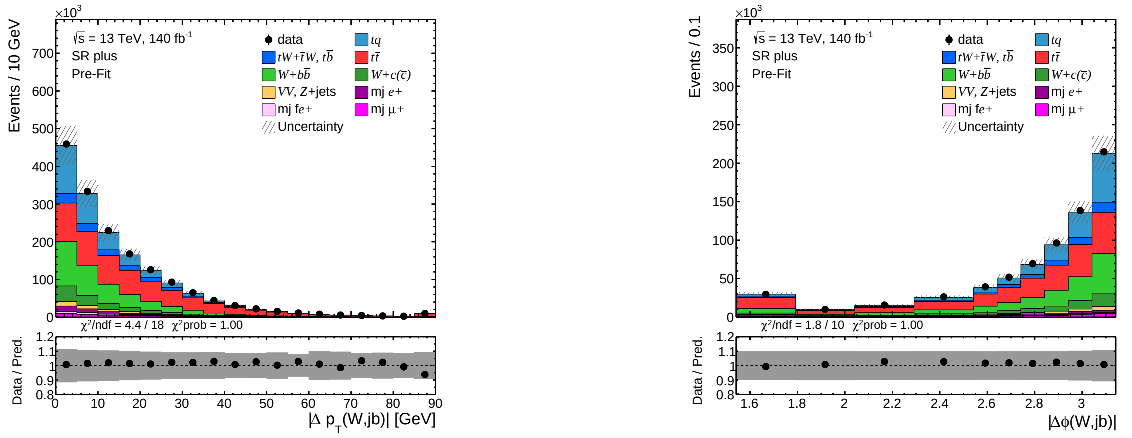

(c) $|\Delta p_{\mathrm{T}}(W, jb)|$ (d) $|\Delta\phi(W, jb)|$

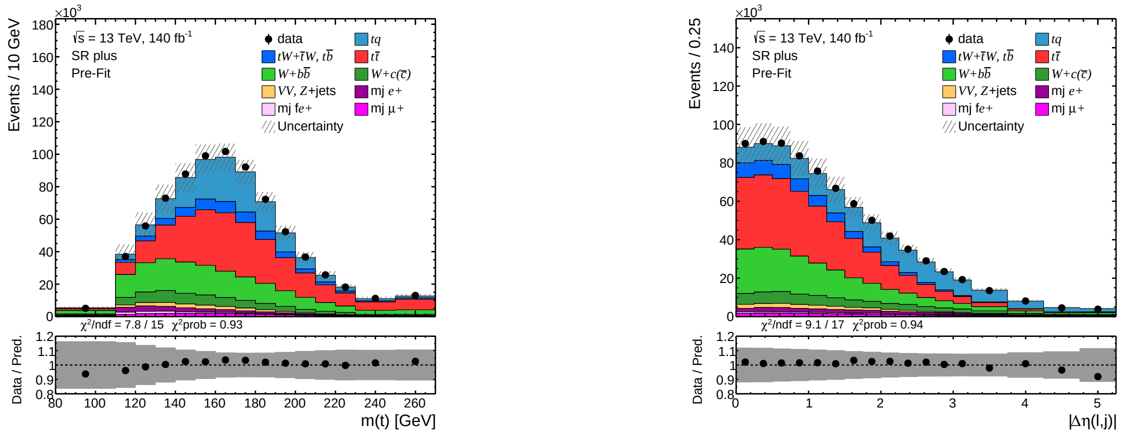

(e) $m(t)$ (f) $|\Delta\eta(\ell, j)|$

Figure 7.5.: Distributions for the first six input variables comparing simulation to data. The uncertainty band includes all systematic uncertainties.

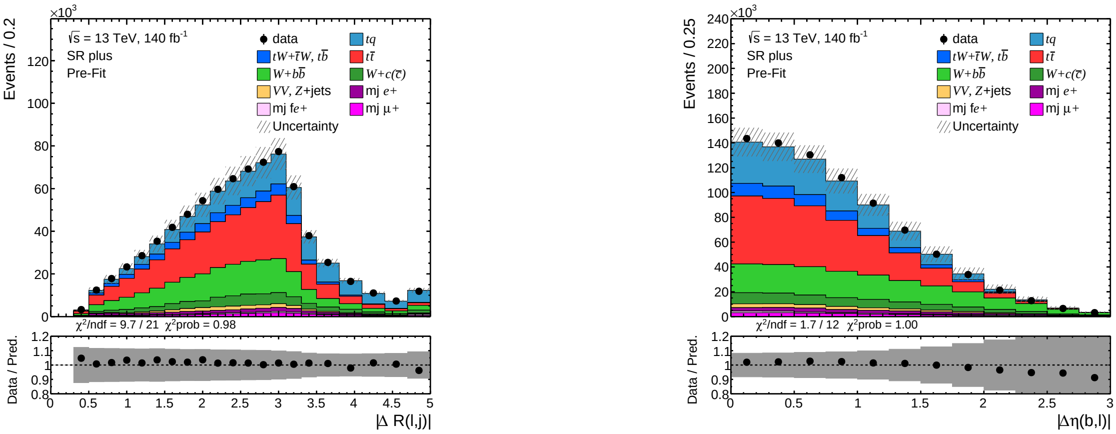

(a) $\Delta R(\ell, j)$ (b) $|\Delta\eta(b, \ell)|$

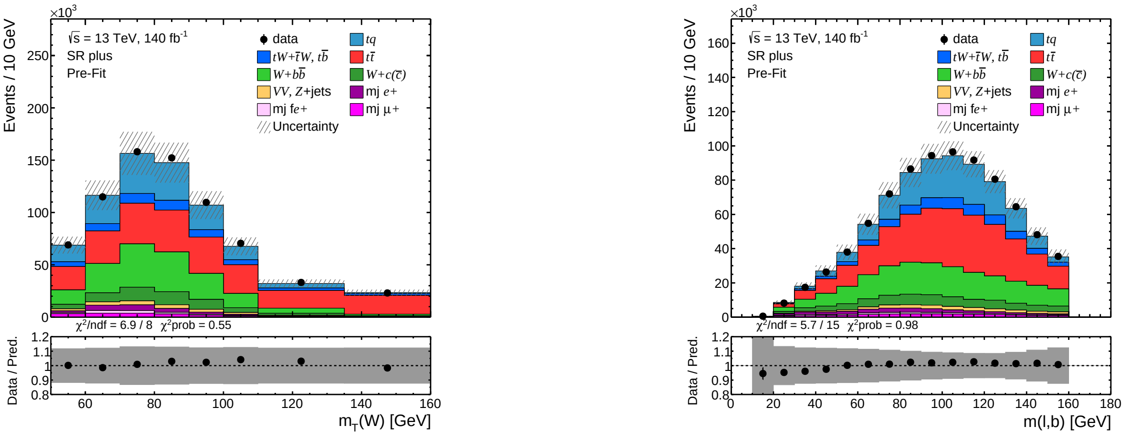

(c) $m_{\mathrm{T}}(W)$ (d) $m(\ell b)$

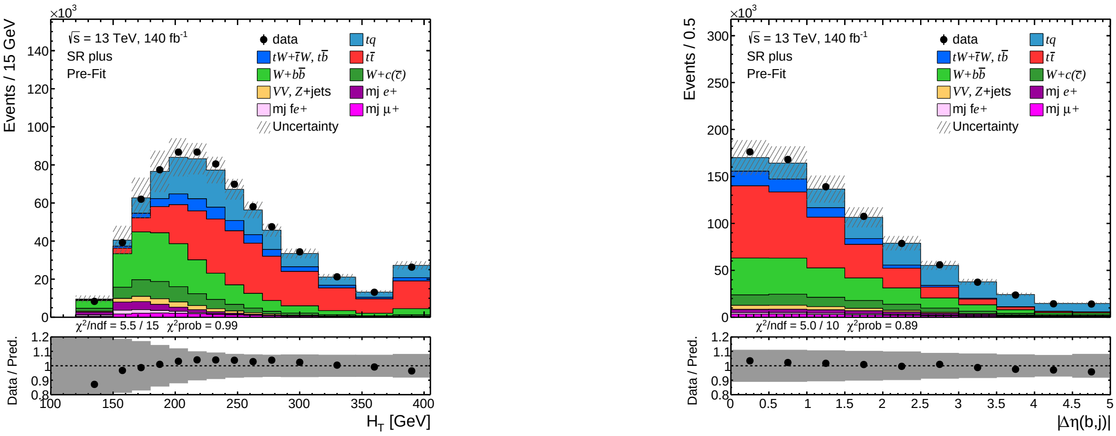

(e) H_{T} (f) $|\Delta\eta(b, j)|$

Figure 7.6.: Distributions of the seventh to twelfth input variable comparing simulation to data. The uncertainty band includes all systematic uncertainties.

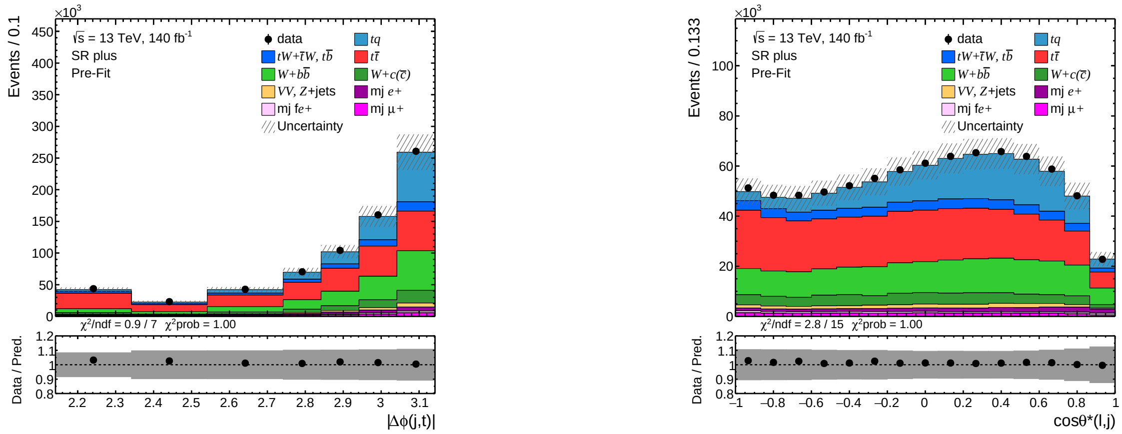

(a) $|\Delta\phi(j,t)|$

(b) $\cos\theta^*(\ell,j)$

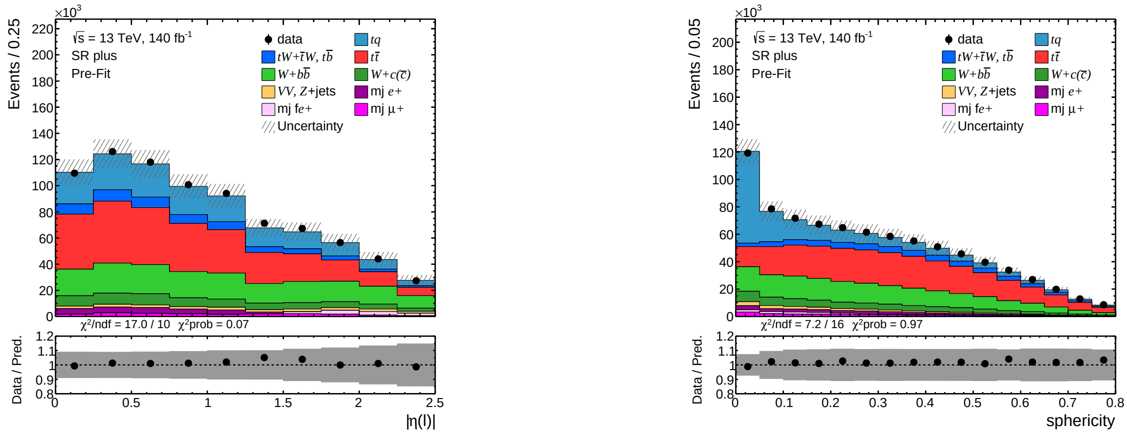

(c) $|\eta(\ell)|$

(d) sphericity

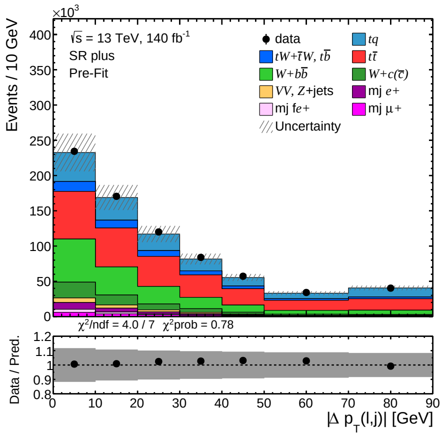

(e) $|\Delta p_{\mathrm{T}}(\ell,j)|$

Figure 7.7.: Distributions of the last five input variables comparing simulation to data. The uncertainty band includes all systematic uncertainties.

7.2. Training Quality

The training of the neural network converges after five iterations of the BFGS algorithm. A low number of iterations is expected due to the high efficiency of the algorithm. The shape of the distribution of the neural network output variable D_{nn} for the signal process and the main background processes is given in Figure 7.8.

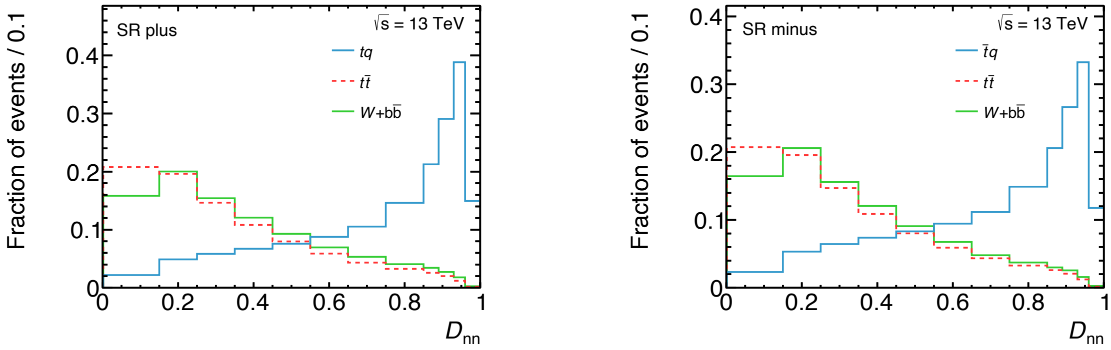

(a) SR `plus`

(b) SR `minus`

Figure 7.8.: Simulated shape of the signal and main background processes in the neural network output distributions.

NeuroBayes provides additional plots to check the quality of the training. As is the case in the training, for these plots the signal process is scaled to match the background yield. In Figure 7.9 the signal purity, defined as the fraction of signal events, of the network output distribution is shown. Due to the use of the entropy loss function the signal purity is expected to approximately follow the diagonal line once the network is trained [129].

It is possible to change multiple hyper parameters to configure the training process in NeuroBayes. Various values for *speed* which is a factor on the training speed, *maxlearn* which sets a maximum value of the training speed and *momentum* which adds a fraction of the change in weights of the previous weight update to the next one, are tried to improve the separation power of the neural network. In all such tests no significant improvements could be achieved and therefore NeuroBayes default values are used.

In Figure 7.10 the signal purity is plotted against the signal efficiency when introducing a selection based on D_{NN} to the simulated data. Specifically, a cut of

$$D_{\mathrm{NN}} < x \quad \text{or} \quad D_{\mathrm{NN}} > x$$

where x is the chosen cut-off value, selects a part of the simulated dataset with a certain fraction of selected signal events from the total number of signal events, called the signal efficiency. For different signal efficiencies reached by placing a cut on D_{NN} the signal purity is computed. The resulting curves can be used to determine a good cut value on D_{nn} or to compare different neural networks with each other.

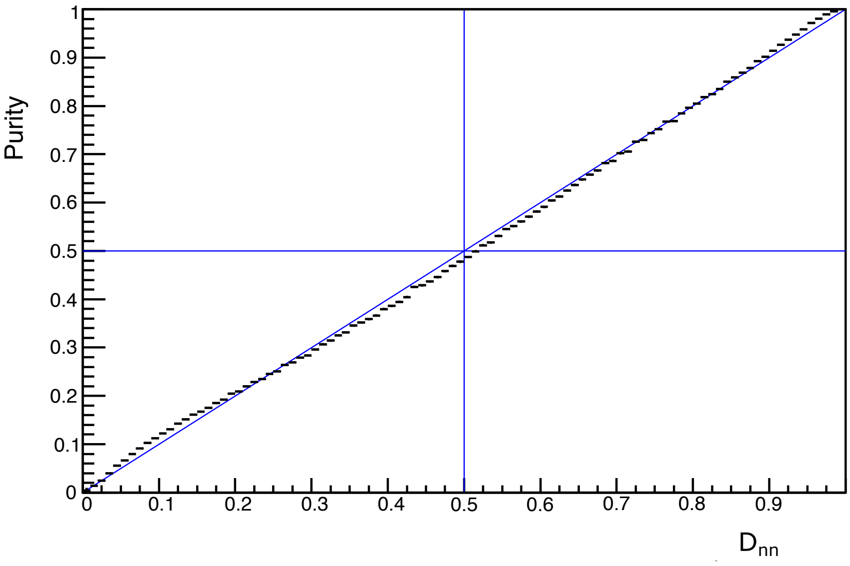

Figure 7.9.: Signal purity in the neural output distribution.

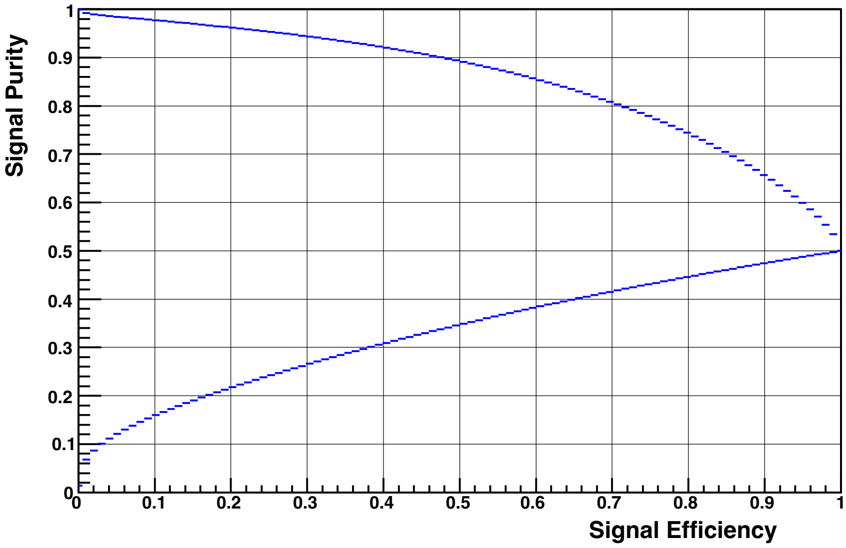

Figure 7.10.: Signal purity of selected events based on a cut on the neural network output value with a certain signal efficiency.

8. Uncertainties

Precisely determining the uncertainties affecting a measurement is essential for ensuring the reliability and validity of the results in any analysis. The inherent statistical uncertainty from the dataset can be directly quantified. However, several sources of systematic uncertainty demand a more nuanced evaluation. These sources of uncertainty can be broadly categorized into two main groups:

- Uncertainties arising from detector calibration and precision: These uncertainties stem from the calibration processes and the inherent precision limits of the detector apparatus. They encompass various factors such as detector alignment, energy scale calibration, and efficiency of the detector components.
- Uncertainties related to MC simulation and modeling: These uncertainties are associated with the assumptions and approximations used in the simulation and modeling of the data. They include uncertainties due to the choice of parton distribution functions, modeling of the parton shower and hadronization processes, and potential mismatches between the simulated and real-world experimental conditions.

In the statistical analysis, all systematic uncertainties are quantified as $\pm 1\sigma$ deviations from the nominal MC samples. Notably, any source of systematic uncertainty that exhibits multiple degrees of freedom is broken down into individual components. This approach allows for a comprehensive evaluation, ensuring that each aspect of the systematic uncertainty is properly accounted for. Such granularity is crucial in assessing the collective impact of these uncertainties on the measurements, thereby enhancing the overall robustness and credibility of the analysis.

8.1. Jet Uncertainties

Reconstructed jets are affected by systematic uncertainties of the JES calibration and the determination of the JER. A comprehensive description of the JES and JER uncertainties can be found in [114]. In this analysis, the *category reduction* set of 30 distinct variations is used to describe JES uncertainties, capturing the various systematic influences on the jet energy calibration. There are different sources of uncertainties included in the description of the JES which are reduced to a set of orthogonal terms. Sources of considered uncertainties include the intercalibration of forward and barrel jets, pile-up uncertainties, flavour dependence uncertainties accounting for relative flavour fractions and differing responses to quark- and gluon-initiated jets. Additional uncertainties are included to describe uncertainties in the response to high p_{T} particles, as well as uncertainties accounting for the difference in jet response between Atlfast-II and the full detector simulation with Geant4.

The JER uncertainties are described using the *FullJER* set of MC variations, using 13 variations. This ensures that differences in the simulated JER and the true JER in data are accounted for in the analysis with high precision. JER uncertainties are generated by smearing the measured jet energy in MC and pseudodata, which is obtained by treating the available MC as data. The smearing is determined based on the observed difference between JER in data and MC depending on jet η and jet p_{T}. An additional jet uncertainty comes from the calibration of the JVT and fJVT.

8.2. Flavor Tagging Uncertainties

Uncertainties associated with the b-tagging efficiency for true b-jets and the mistagging rates for light-quark jets and c-jets are considered. The b-tagging efficiency is measured in dileptonic $t\bar{t}$ events, with discrepancies between observed data and detector simulations corrected via p_{T}-dependent scale factors. These uncertainties are represented as variations in these factors and are divided into 45 orthogonal components, as detailed in Ref. [133]. For c-jets, the mistagging rate is determined in semileptonic $t\bar{t}$ events, utilizing the well-established $W \to cs$ branching ratio. The uncertainties in this rate, which vary from 3% to 17%, are categorized into 20 orthogonal components, as referenced in Ref. [134]. Furthermore, the misidentification rate of light-quark jets is assessed, with calibration factors ranging from approximately 1.5 to 3 and uncertainties up to 50%. The analysis of light-quark jet misidentification involves 20 independent eigenvectors, as outlined in Ref. [135].

8.3. Missing Transverse Momentum

The uncertainty in the $\vec{p}_{\mathrm{T}}^{\mathrm{miss}}$ includes the uncertainties of all reconstructed objects used in the calculation of the $\vec{p}_{\mathrm{T}}^{\mathrm{miss}}$. Additionally, the uncertainty of the soft component of the $\vec{p}_{\mathrm{T}}^{\mathrm{miss}}$ coming from inner detector tracks that point to the primary vertex but are not associated with a reconstructed object needs to be evaluated. This uncertainty corresponds to the disagreement of the soft and hard terms in events without true $\vec{p}_{\mathrm{T}}^{\mathrm{miss}}$. It is split into three components:

- A parallel scale uncertainty, characterized by deviations along the p_{T} (hard) axis, representing shifts in the expected value of the soft track component parallel to the hard component.
- Resolution along the p_{T} (hard) axis.
- Resolution perpendicular to the p_{T} (hard) axis.

The uncertainty is evaluated by comparing these components in a data sample to predictions by different MC generators and taking the maximum difference as uncertainty.

8.4. Lepton Uncertainties

For electrons measured at the average transverse energy in the Z-based calibration, systematic uncertainties related to the electron energy scale are effectively negated. However, at other energy levels, these uncertainties are not completely removed due to their potential energy-dependent nature. The electron energy scale encompasses a wide array of uncertainty sources, as elaborated in Ref. [116]. For the purposes of this analysis, all systematic uncertainties linked to the electron energy scale are aggregated into a single variation.

The energy resolution for electrons arises from fluctuations within the shower in the calorimeter, variations in energy loss prior to reaching the calorimeter, and noise introduced by pileup and readout electronics. The energy resolution is ascertained via the Z-based calibration, meaning systematic uncertainties predominantly influence the extrapolation of this resolution to different energies. The uncertainty associated with the electron energy resolution is captured in a single variation.

The uncertainty in the trigger efficiency measurement, as referenced in Ref. [136], which is utilized to adjust the trigger efficiency in simulations to match the data, is also consolidated into one variation.

Calibration uncertainties for the reconstruction, identification, and isolation of electrons and muons are propagated as one variation each. These uncertainties are gauged by comparing data to MC prediction in $Z \to ee$ and $Z \to \mu\mu$ events, as detailed in Ref. [118].

8.5. Normalization Uncertainties

The normalization of background processes is subject to various uncertainties. Top-quark production processes are normalized to theoretical predictions, as described in Chapter 3. The uncertainty of the inclusive cross-sections is estimated by varying the renormalization and factorization scales used in the calculation and by incorporating uncertainties from PDFs.

Previous analyses [137] have observed discrepancies between the expected and measured $W + b\bar{b}$ rate. To accommodate the inaccuracy of the predicted $W + b\bar{b}$ rate, a rate uncertainty of 40 % is applied to this process. This adjustment allows the $W + b\bar{b}$ rate to be largely determined during the fit, meaning that the exact size of the rate uncertainty has minimal impact on the precision of the signal measurement. The $W + c(\bar{c})$ process includes contributions from the charge asymmetric $W + c$ and $W + \bar{c}$ processes, as well as the charge symmetric $W + c\bar{c}$ process. Given the uncertainty in the composition of these processes, a separate $W + c(\bar{c})$ rate uncertainty of 20 % is applied in both the positive and negative lepton channels. Additionally, a 20 % uncertainty is applied to the Z+jets and diboson process rates.

8.6. Modeling Uncertainties

Modeling uncertainties arise from the choices made during the production of MC samples. One such choice involves the method used to match matrix element event generation with the parton-shower algorithm. To assess the uncertainty associated with this choice, different settings of the matching procedure are compared. Specifically, the setting `POWHEG:pThard`, which determines how the hardness of the Powheg event is defined in Pythia, is varied from its default value of 0 to 1.

Additionally, the choice of shower algorithm and hadronization model introduces phenomenological uncertainties. These are estimated by comparing the nominal sample with an alternative setup using Powheg +Herwig. For both the matching and shower uncertainties, the impact on the overall acceptance of events in the selection and the differences in the predicted shapes of the processes in the fitted distribution are treated as separate uncertainties. For the $t\bar{t}$ process, the nominal sample is compared to one where the h_{damp} parameter is adjusted to three times the top-quark mass and the difference is used as an uncertainty.

The uncertainty coming from the limited order of considered Feynman diagrams in the hard scattering simulation is estimated by varying the renormalization scale μ_{R} to 0.5 and 2 times its nominal value. The uncertainty coming from the factorization of the PDFs and the matrix-element calculation is evaluated by varying the factorization scale μ_{F} to 0.5 and 2 times its nominal value. Uncertainty of the modeling of the initial-state and final-state shower in PYTHIA is estimated by variation of the parameter `Var3c` of the A14 parton-shower tune. Additionally, the renormalization scale μ_{R} is varied to 0.5 and 2 times its nominal value in the final-state parton-shower calculation to generate an uncertainty. The uncertainty due overlap removal of the $t\bar{t}$ and tW processes is estimated by comparing the nominal sample employing the diagram removal scheme with an alternative sample using the diagram subtraction scheme [82]. Uncertainties of the PDF set are described employing the PDF4LHC15 PDF set with 30 variations [138], which are compared to the central PDF4LHC15 value.

Variations in the multijet process samples, as described in Chapter 4, serve as an uncertainty in the shape predicted by the methods. For the electron multijet process, two variations in the templates are utilized, while a single variation is employed for the muon multijet process. To compensate for discrepancies in the multijet rate between the CRs and the SRs, an additional rate uncertainty of 30 % is applied to each multijet template within the SRs. Furthermore, the variance in the rate of muon multijet between the positive and negative lepton channels is considered as an additional uncertainty. The overall rates of the multijet subprocesses are determined by three free parameters during the fit. One parameter governs the normalization of the muon multijet subprocess `mj` μ, another controls the normalization of the barrel electron subprocess `mj` e, and a third parameter is for the normalization of the end-cap electron subprocess `mj` fe. The adoption of separate normalization factors for the barrel and end-cap electron subprocesses is motivated by potential differences in the modeling of the detector between the barrel and end-cap regions of the ECAL.

9. Binned Maximum Likelihood Fit

In the subsequent stages of the statistical analysis, the measurement of the t-channel cross-sections and R_t is conducted using a maximum likelihood fit method, by comparing the collected data with simulation. The conventional approach for estimating the parameters $\boldsymbol{\theta}$ of a known probability density function $P_{\boldsymbol{\theta}}(x)$ from a given set of data x_i is the maximum likelihood (ML) method. The likelihood function is defined by

$$L(\boldsymbol{\theta}) = \prod_i P_{\boldsymbol{\theta}}(x_i)$$

where $P_{\boldsymbol{\theta}}(x)$ represents the probability of observing the data x_i given the parameters $\boldsymbol{\theta}$. This formulation considers the data to be fixed while the unknown parameters of the probability density function are treated as variables.

Maximizing the likelihood function then yields estimated values of the parameters $\boldsymbol{\theta}$, called ML estimators, for a given set of data. If the number of events in the set of data is itself Poisson distributed the extended likelihood

$$L(\boldsymbol{\theta}) = \frac{e^{-N(\boldsymbol{\theta})}}{n!} \prod_i N(\boldsymbol{\theta}) P_{\boldsymbol{\theta}}(x_i)$$

can be used, where $N(\boldsymbol{\theta})$ is the predicted and n is the measured number of events.

It can be shown that the ML procedure always yields efficient estimators of the parameters in the large sample limit [139], meaning that the uncertainty of the measured parameters is minimal.

In this analysis, the probability density function is not explicitly known in an analytical form. Instead, theoretical predictions are represented through MC simulations. To implement the ML method under these conditions, the data is binned into a histogram. Subsequently, the number of events in each histogram bin follows a Poisson distribution and can be used as input for the ML method. This binned ML method offers an advantage over simpler approaches as it enables the auxiliary measurements characterizing systematic uncertainties to be refined using the data, thus mitigating the influence of the systematic uncertainties on the measurement.

Neglecting both systematic and statistical uncertainties of the MC samples, the predicted number of events depends solely on the signal parameters $\boldsymbol{\mu}$, which parameterize the signal cross-sections and R_t. The likelihood function can thus be expressed as follows:

$$L(\boldsymbol{\mu}) = \prod_i \mathrm{Pois}(n_i | N_i(\boldsymbol{\mu}))$$

Here, n_i represents the count of data events in bin i, while $N_i(\boldsymbol{\mu})$ stands for the predicted number of events in bin i, taking into account the signal parameters $\boldsymbol{\mu}$. The predicted value $N_i(\boldsymbol{\mu})$ can be described in terms of the individual processes as follows:

$$N_i(\boldsymbol{\mu}) = \mu_{tq} S_i^{tq} + \mu_{\bar{t}q} S_i^{\bar{t}q} + \sum_j B_{ij}$$

Here, S_i^{tq} and $S_i^{\bar{t}q}$ denote the expected numbers of tq and $\bar{t}q$ events, respectively, as predicted by the SM for bin i. The signal parameters μ_{tq} and $\mu_{\bar{t}q}$ are defined as factors of the signal event counts. Additionally, B_{ij} is the predicted event count for the jth background process in bin i.

The MC prediction N_i is subject to the uncertainties described in Section 8. Systematic uncertainties are described as auxiliary measurements of nuisance parameters $\boldsymbol{\theta}$, which influence the predicted numbers of events N_i. The auxiliary measurements are included in the likelihood as additional terms constraining the nuisance parameters to their measured values:

$$L(\boldsymbol{\mu}, \boldsymbol{\theta}) = \prod_i \mathrm{Pois}(n_i | N_i(\boldsymbol{\mu}, \boldsymbol{\theta})) \prod_j \mathrm{Gauss}(0 | \mu = \theta_j, \sigma = 1)$$

where $\mathrm{Gauss}(0|\mu = \theta_j, \sigma = 1)$ is the probability density for one auxiliary measurement with the corresponding parameter θ_j.

The parameters θ_j are defined such that their nominal value is 0, and their 1σ uncertainty, inferred from auxiliary measurements, is 1. When θ_j assumes a value of 0, the MC prediction $N_i(\mu, \boldsymbol{\theta})$ remains unaltered and at $\theta_i = \pm 1$, the MC prediction adjusts correspondingly to the upper and lower 1σ bounds of the relevant auxiliary measurement. The MC prediction is interpolated between these values and extrapolated beyond them. For this purpose, each systematic uncertainty's variations are split into the overall normalization change of the templates and the shape change of the template. This split allows the use of different interpolation and extrapolation methods for the two components. For the normalization component N_{norm}, an exponential interpolation and extrapolation are used.

$$N_{\text{norm}} = \begin{cases} \left(\frac{I^+}{I^0}\right)^{\alpha}, & \alpha \geq 0 \\ \left(\frac{I^-}{I^0}\right)^{\alpha}, & \alpha < 0 \end{cases}$$

where I^+ and I^- are the 1σ variations of the template's normalization from the given systematic uncertainty. For small uncertainties, this results in an almost linear behavior, while for large uncertainties, negative yields are prevented through the exponential extrapolation. For the shape, linear interpolation and extrapolation are used.

Additional nuisance parameters γ_i are used to quantify the statistical uncertainty inherent in the MC prediction. These parameters serve as scaling factors applied to the MC prediction. In each bin, a singular parameter characterizes the statistical uncertainty across all processes. To incorporate the magnitude of this statistical uncertainty into the likelihood calculation, Poisson terms $\text{Pois}(\tau_i|\gamma_i\tau_i)$ are introduced, where

$$\tau_i = \left(\frac{N_i^0}{\Delta N_i^0}\right)^2$$

is the effective number of MC events in bin i, calculated from the nominal predicted number of events N_i^0 and its statistical uncertainty ΔN_i^0. These additional terms function as auxiliary measurements for the γ_i factors, specifically addressing the statistical component of the MC prediction.

Finally, the complete likelihood function can be written down:

$$L(\boldsymbol{\mu},\boldsymbol{\theta},\boldsymbol{\gamma}) = \prod_i \text{Pois}(n_i|\gamma_i N_i(\boldsymbol{\mu},\boldsymbol{\theta})) \prod_j \text{Gauss}(0|\mu{=}\theta_j,\sigma{=}1) \prod_k \text{Pois}(\tau_k|\gamma_k\tau_j)$$

Substituting the respective terms the full Likelihood is given by:

$$L(\boldsymbol{\mu},\boldsymbol{\theta},\boldsymbol{\gamma}) = \prod_i \frac{(\gamma_i N_i(\boldsymbol{\mu},\boldsymbol{\theta}))^{n_i} e^{-\gamma_i N_i(\boldsymbol{\mu},\boldsymbol{\theta})}}{n_i!} \prod_j \frac{1}{\sqrt{2\pi}} e^{-\theta_j^2/4} \prod_k \frac{(\gamma_k\tau_k)^{\tau_k} e^{-\gamma_k\tau_k}}{\Gamma(\tau_k+1)}$$

To avoid numerical problems from the likelihood becoming too small, instead of maximizing the likelihood the negative logarithm of the likelihood function $-\log(L(\boldsymbol{\mu},\boldsymbol{\theta},\boldsymbol{\gamma}))$ is minimized.

The uncertainty of the ML estimators is assessed using the graphical method:

$$\log(L(\hat{\theta}^{+u}_{-d})) = \log(L_{\max}) - \frac{1}{2}$$

Here, $\hat{\theta}$ represents the ML estimator for a parameter θ, and $L(\theta)$ denotes the profile likelihood function, defined as the maximum of the likelihood function for a given value of θ. The central 1σ confidence interval of the parameter θ is then given by $[\hat{\theta} + u, \hat{\theta} - d]$.

This approach yields approximations of the central 1σ confidence intervals for the parameters, even in cases where deviations from a strictly Gaussian distribution are present in the log-likelihood function [140].

In practice, the likelihood function is built using the `HistFactory` framework. The minimization is carried out using the `MINUIT` software library and using the `MIGRAD` algorithm. The `MINOS` algorithm is employed for determining uncertainties using the profile likelihood based method described above.

9.1. Signal Parameter Parameterization

Two parameterizations of the signal normalizations are used, one to determine the top-quark and top-antiquark t-channel cross-sections

$$\sigma_t = \mu_t \sigma_t^{\mathrm{SM}} \qquad \sigma_{\bar{t}} = \mu_{\bar{t}} \sigma_{\bar{t}}^{\mathrm{SM}}$$

and another parameterization to determine their ratio R_t and the total t-channel cross-section:

$$\sigma_t = \mu_{\mathrm{tch}} \mu_{R_t} \frac{R_t^{\mathrm{SM}} + 1}{\mu_{R_t} R_t^{\mathrm{SM}} + 1} \sigma_t^{\mathrm{SM}} \qquad \sigma_{\bar{t}} = \mu_{\mathrm{tch}} \frac{R_t^{\mathrm{SM}} + 1}{\mu_{R_t} R_t^{\mathrm{SM}} + 1} \sigma_{\bar{t}}^{\mathrm{SM}}$$

The second parameterization is derived by expressing the signal normalization parameters μ_t and $\mu_{\bar{t}}$ in terms of μ_{R_t} and μ_{tch}. As a first step the parameters μ_{R_t} and μ_{tch} are expressed in terms of μ_t and $\mu_{\bar{t}}$:

$$\mu_{\mathrm{tch}} = \frac{\sigma_t + \sigma_{\bar{t}}}{\sigma_t^{\mathrm{SM}} + \sigma_{\bar{t}}^{\mathrm{SM}}} = \frac{\mu_t \sigma_t^{\mathrm{SM}} + \mu_{\bar{t}} \sigma_{\bar{t}}^{\mathrm{SM}}}{\sigma_t^{\mathrm{SM}} + \sigma_{\bar{t}}^{\mathrm{SM}}} = \frac{\mu_t R_t^{\mathrm{SM}} + \mu_{\bar{t}}}{R_t^{\mathrm{SM}} + 1}$$

$$\mu_{R_t} = \frac{R_t}{R_t^{\mathrm{SM}}} = \frac{\frac{\sigma_t}{\sigma_{\bar{t}}}}{\frac{\sigma_t^{\mathrm{SM}}}{\sigma_{\bar{t}}^{\mathrm{SM}}}} = \frac{\frac{\mu_t \sigma_t^{\mathrm{SM}}}{\mu_{\bar{t}} \sigma_{\bar{t}}^{\mathrm{SM}}}}{\frac{\sigma_t^{\mathrm{SM}}}{\sigma_{\bar{t}}^{\mathrm{SM}}}} = \frac{\mu_t}{\mu_{\bar{t}}}$$

This set of equations can then be solved for μ_t and $\mu_{\bar{t}}$:

$$\mu_{\mathrm{tch}} = \frac{\mu_t R_t^{\mathrm{SM}} + \mu_{\bar{t}}}{R_t^{\mathrm{SM}} + 1} = \frac{\mu_t R_t^{\mathrm{SM}} + \frac{\mu_t}{\mu_{R_t}}}{R_t^{\mathrm{SM}} + 1} = \frac{\mu_t}{\mu_{R_t}} \frac{\mu_{R_t} R_t^{\mathrm{SM}} + 1}{R_t^{\mathrm{SM}} + 1}$$

$$\implies \mu_t = \mu_{\text{tch}} \mu_{R_t} \frac{R_t^{\text{SM}} + 1}{\mu_{R_t} R_t^{\text{SM}} + 1}$$

$$\implies \mu_{\bar{t}} = \mu_{\text{tch}} \frac{R_t^{\text{SM}} + 1}{\mu_{R_t} R_t^{\text{SM}} + 1}$$

These expressions are then incorporated into the likelihood function, resulting in a likelihood function expressed in terms of μ_{R_t} and μ_{tch}.

9.2. Fitted Distributions

It is possible, to combine several regions in a simultaneous fit by using all bins of all input distributions in the considered regions in the likelihood function. In that case, it is important to consider which nuisance parameters are shared between all regions and which nuisance parameters need to be separated between certain regions. In this analysis, the two SRs, SR `plus` and SR `minus`, and the six CRs are fitted simultaneously. The SRs are fitted simultaneously to enable the determination of R_t, while the CRs are used to constrain the multijet normalization. The simultaneous determination of the multijet normalization enables the correct propagation of the multijet normalization uncertainty. Additional CRs to constrain the normalisation of other background processes are not used due to the high constraining power of the SRs.

9.3. Template smoothing

The predicted number of events N_i in the analysis depends on the differences between the nominal MC predictions and the variations associated with each nuisance parameter. Both the nominal template and its variations are subject to statistical uncertainties. These uncertainties are correlated to varying degrees, depending on the methods used to generate the variations. The statistical uncertainty in the difference between the nominal MC predictions and the variations is usually unknown, although there are some exceptions. However, this statistical uncertainty in the templates is not a direct uncertainty of the analysis, but instead introduces deviations in the estimated uncertainties of the measured parameters. It is therefore necessary to implement effective strategies to mitigate its impact on the measurement.

One method to address this is by broadening the bins in the neural network distribution, though this can reduce the measurement's accuracy. Thus, finding an appropriate balance between reducing the template's statistical uncertainty and maintaining the precision of the measurement is crucial. Despite the challenges in ascertaining the statistical uncertainty between templates, it is imperative to lessen its influence. Furthermore, as most systematic uncertainties are expected to display smooth variations in physical parameters and consequently in the neural network output, applying a smoothing algorithm can significantly decrease statistical fluctuations. Although the precision in recovering the shape of the systematic template is limited, smoothing helps facilitate finer binning in the neural network distribution. This, in turn, indirectly enhances the precision of the overall measurement.

For this analysis, a custom smoothing algorithm is utilized, designed to prevent the reduction of the overall size of systematic uncertainties during the smoothing process. This is crucial to avoid underestimating the uncertainties of the measured quantities.

The algorithm comprises two main steps: rebinning to reduce statistical fluctuations, and smoothing to interpolate back to the original binning. In the rebinning step, both the systematic uncertainty template s and the nominal template n are temporarily rebinned by merging adjacent bins, reducing the total number of bins from N_o to N_r. During this process, the rebinned versions of s and n are denoted as $\tilde{s}$ and $\tilde{n}$, respectively. The bin-wise ratios $t_i = s_i/n_i$ and $\tilde{t}_i = \tilde{s}_{j(i)}/\tilde{n}_{j(i)}$ are then calculated, where $i = 1, \ldots, N_\mathrm{o}$ and $j(i)$ identifies the bin in the rebinned templates corresponding to bin i in the original template.

To ensure that the rebinning primarily targets the removal of statistical fluctuations without eliminating shape effects, two rules are implemented:

- Two adjacent bins are only merged if one of them in $\tilde{t}$ has a higher or lower value than both of its neighboring bins. This prevents the merging of bins in cases where t is monotonically increasing or decreasing.
- Bins are not merged if the resulting $\tilde{t}$ would produce three consecutive bins, all having either higher or lower values compared to t. This rule serves to preserve the original shape characteristics of the data.

If, after applying the two aforementioned rules, multiple bin pairs are eligible for merging, the pair chosen is the one where merging results in the smallest value of D, defined as:

$$D = \sup_{j=1,\ldots,N_o} \left(\left| \sum_{i=1}^{j} \tilde{t}_i - t_i \right| \right) . \qquad (9.1)$$

Adjacent bin pairs are merged successively following these criteria until no further eligible bins remain for merging.

Subsequently, the rebinned ratio template $\tilde{t}$ undergoes smoothing. This is executed using a slightly adapted version of the TH1::SMOOTH() algorithm, part of the TH1 histogram class in the ROOT library. The ROOT smoothing algorithm is applied three times consecutively to $\tilde{t}$. It involves successive running medians of 3, 5, and 3, quadratic interpolation, a running mean, and twicing. The specific steps are detailed in Ref. [141]. A modification is made to the algorithm to keep the first and last bin unaltered in the running medians during the first smoothing pass. The final smoothed systematic uncertainty template is then computed by multiplying, bin-wise, with the original nominal template.

9.4. Symmetrization

The next step in preparing the templates for this analysis is symmetrization. This process essentially serves as another means of smoothing the templates. It is based on the assumption that the impacts of a $+1\sigma$ and -1σ variation due to a systematic uncertainty are identical in magnitude but opposite in direction relative to the nominal template. Depending on the nature of the systematic uncertainty, different methods of symmetrization may be employed, or in some cases, it may not be applied at all.

The most commonly used method is two-sided symmetrization. In this approach, the average of the $+1\sigma$ and -1σ template deviations is calculated. This averaged deviation is then both added to and subtracted from the nominal template to create symmetrized variations. This technique is applied to all systematic uncertainties that have two variations, with the exception of JER uncertainties, where the asymmetric behavior is preserved due to its physical relevance.

In situations where only a single variation is available for a systematic uncertainty, an alternative method is employed. Here, the difference between the systematic variation and the nominal template is subtracted from the nominal. This process effectively generates a second, mirrored variation, enabling a symmetrized approach even with a single variation.

Symmetrizing one-sided uncertainties is key to creating a smooth likelihood function for all nuisance parameters. This is important for the optimization algorithm, which depends on accurate gradient calculations of the log-likelihood function.

9.5. Templates for Systematic Uncertainties

Systematic uncertainties have a bigger influence on the measurement's accuracy than statistical uncertainty, particularly due to the extensive amount of data in the SRs. This measurement is more sensitive to the model of systematic uncertainty than previous measurements which used less data. Therefore, a precise and robust handling of systematic uncertainties is crucial for achieving an accurate measurement and reliable uncertainty estimation. This section shows templates for several key systematic uncertainties, illustrating the variations before and after the implementation of symmetrization and smoothing procedures.

The Figures from 9.1 to 9.3 depict the variations in the most impactful systematic uncertainties for μ_t and $\mu_{\bar{t}}$ in the neural network output distribution.

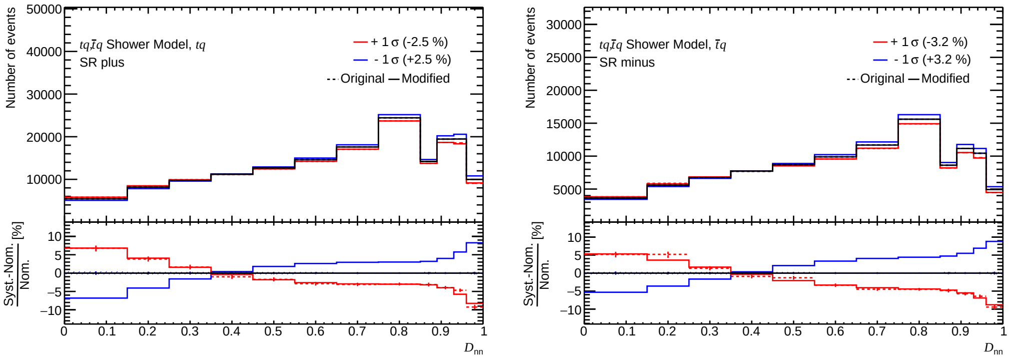

(a) t-channel SR `plus` (b) t-channel SR `minus`

Figure 9.1.: Templates describing the signal shower modeling uncertainty. In the fit the shape and normalization are separated. The original variation is shown with a dashed line and the symmetrized and smoothed up and down variations are shown with continuous lines.

The up and down variations for the JER uncertainty are inherently asymmetric around the nominal template, a characteristic stemming from their construction. This asymmetry in the JER templates is not adjusted through symmetrization. Consequently, the impact of JER uncertainty components on the parameters of interest may also exhibit asymmetry. An example of the variations for the first component of the JER uncertainty is illustrated in Figure 9.4.

Incorporating the asymmetry of uncertainties into the fit can enhance the precision in describing uncertainties, but it may also lead to less predictable behavior in the likelihood function. A potential risk of this approach is the

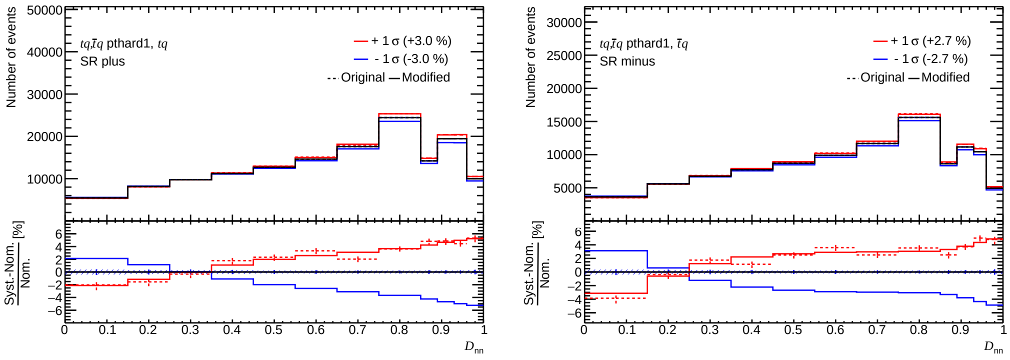

(a) t-channel SR plus (b) t-channel SR minus

Figure 9.2.: Templates describing the signal shower matching uncertainty. In the fit the shape and normalization are separated. The original variation is shown with a dashed line and the symmetrized and smoothed up and down variations are shown with continuous lines.

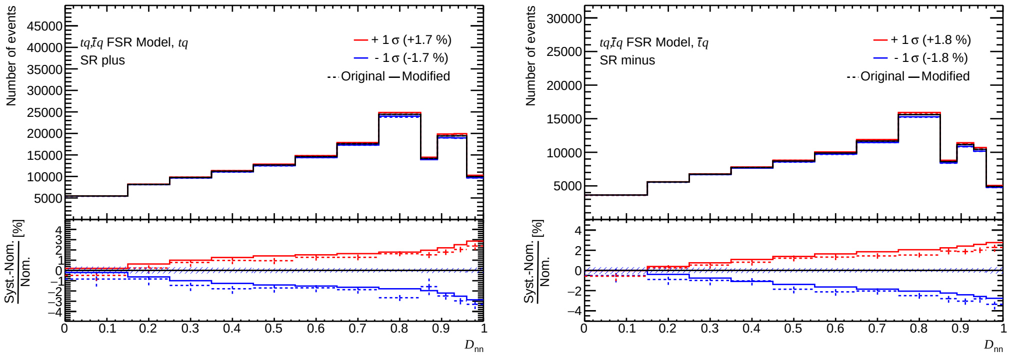

(a) *t*-channel SR `plus` (b) *t*-channel SR `minus`

Figure 9.3.: Templates describing the signal FSR uncertainty. The original variation is shown with a dashed line and the symmetrized and smoothed up and down variations are shown with continuous lines.

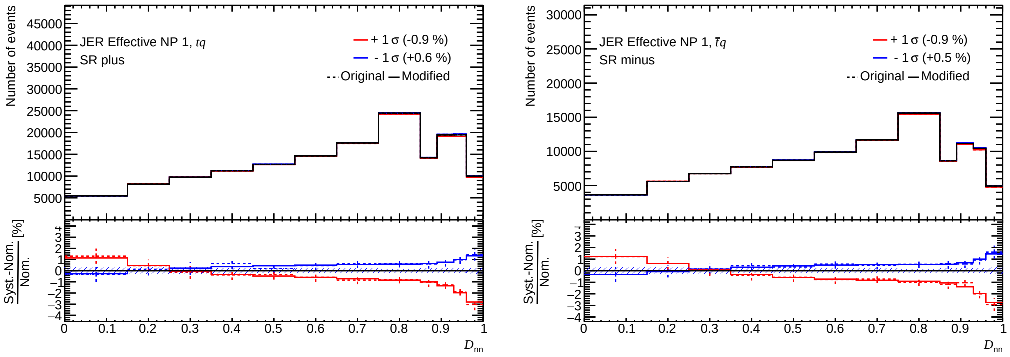

(a) t-channel SR `plus` (b) t-channel SR `minus`

Figure 9.4.: Templates describing the first component of the JER uncertainty for the signal process. The original variation is shown with a dashed line and the symmetrized and smoothed up and down variations are shown with continuous lines.

emergence of additional local maxima in the likelihood, complicating the analysis and interpretation of the results.

9.6. Binning

Selecting the appropriate binning for the neural network distribution in a maximum likelihood fit is a nuanced decision that can significantly impact the analysis. The objective is to choose a binning that optimizes the precision of the measurement, without allowing the statistical uncertainties of the systematic variations and the nominal MC templates to become so large that they impede the measurement.

Finer binning offers several advantages. It leads to improved resolution in the neural network output distribution, providing a detailed and precise representation of the data. This finer granularity can be particularly useful in identifying subtle features or structures. Additionally, finer bins can increase the sensitivity of the analysis to the signal by increasing the shape information available to the fit. This can reduce the correlation of the estimated values of the signal normalization parameters to the estimated values of the nuisance parameters and as such reduce the impact of systematic uncertainties.

However, finer binning is not without drawbacks. It can lead to increased statistical fluctuations, as smaller bins will generally contain fewer events, potentially resulting in less stable fits and a need for more sophisticated smoothing techniques. The complexity in handling systematic uncertainties also increases, as each bin might exhibit unique behavior, complicating their interpretation and treatment. Moreover, finer binning can be computationally intensive in terms of processing time and memory requirements. This is however not a limiting factor here due to the computational resources available.

On the other hand, broader binning reduces the relative impact of statistical fluctuations by accumulating more events in each bin, leading to more stable estimations. This approach simplifies the management of systematic uncertainties, as each bin encompasses a wider range of the distribution, thereby smoothing out localized systematic variations and often reducing the need to rely on smoothing. Broader bins also ease computational demands, making the analysis more manageable, especially when dealing with limited computational resources.

The binning in this analysis was chosen by hand. Finer binning is used at high D_{nn} values to gain sensitivity to the signal process. At lower D_{nn} values broader bins are chosen. This is done to avoid unnecessary and too strong constraints on systematic uncertainties in the fit. The chosen binning allows for the constraint of the $W+$jets background in the SRs without the need for additional CRs. This simplifies the analysis and avoids the question of how to correlate systematic uncertainties to additional CRs. For the electron CRs all data is combined in one bin for each region. This is done due to the low amount of data in these regions and due to big effects of systematic uncertainties of the multijet background on the shape of distributions in the CRs. Finally, for the muon CRs a simple equidistant binning in $\phi(\vec{p}_{\mathrm{T}}^{\mathrm{miss}}, \mu)$ is chosen except for a bigger first bin where a low amount of the data lies.

9.7. Validation of the Fit Procedure using Asimov Data

To ensure objectivity and prevent potential human bias in the analysis results, the measured signal parameters remain blinded until the final stages of the analysis. Moreover, the fitting process can be assessed without relying on any recorded data. For this, Asimov data is generated, wherein the predicted data values in each bin are used as a substitute for the actual data in the fit. By design, Asimov data perfectly aligns with the nominal MC prediction. Consequently, all nuisance parameters are expected to align with their nominal values, and the signal parameters are anticipated to fit to their predefined nominal value of one. Confirming these outcomes serves as an initial test of the fit procedure's stability.

Additionally, the Asimov data is used to determine the expected values of the uncertainties associated with the fit parameters and the individual impacts on the signal parameters. This step allows for understanding the robustness of the fitting method and for anticipating the potential behavior of the actual data in the fit. The expected uncertainties as determined using the Asimov data are +5.8 % and -5.4 % for $\sigma(tq)$, +6.6 % and -6.2 % for $\sigma(\bar{t}q)$, +6.0 % and -5.2 % for $\sigma(tq + \bar{t}q)$, and +2.3 % and -2.2 % for R_t.

9.8. Results

In this section, results of the maximum likelihood fit to data are presented. Figure 9.5 shows the histogram of the neural network output for data and MC prediction, where the nuisance parameters and signal parameters the MC prediction depends on are set to their estimated values. The fit is carried out simultaneously in the two SRs and the six CRs designed to constrain the multijet normalization in the fit, yielding for the first parameterization

$$\sigma(tq) = 137^{+8}_{-8}\,\text{pb}$$

and

$$\sigma(\bar{t}q) = 84^{+6}_{-5}\,\text{pb},$$

and for the second parameterization

$$\sigma(tq + \bar{t}q) = 221^{+13}_{-13}\,\text{pb}$$

and

$$R_t = 1.636^{+0.036}_{-0.034}.$$

The uncertainties correspond to a relative uncertainty of $+5.9\%$ and -5.5% for $\sigma(tq)$, $+6.6\%$ and -6.2% for $\sigma(\bar{t}q)$, $+6.1\%$ and -5.7% for the combined cross-section and $+2.2\%$ and -2.1% for R_t.

The total predicted number of events depends on the values of the nuisance and signal parameters determined in the fit. In Table 9.1 the total predicted number of events for the different processes is shown for the two SRs.

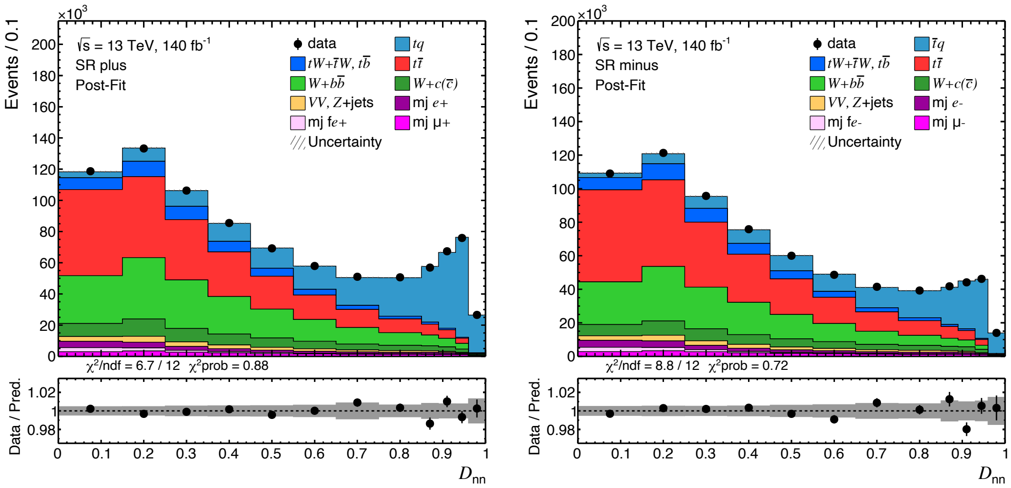

(a) SR `plus`

(b) SR `minus`

Figure 9.5.: Histogram of the neural network output distribution comparing data and the MC prediction, with all nuisance and signal parameters set to their ML estimators. The uncertainty band represents the aggregated MC uncertainty, taking into account correlations among the ML estimators. The bottom plot displays the ratio of observed events to the predicted count for each bin.

Table 9.1.: The yields in the two SRs when setting all fit parameters to their estimated values. All uncertainties applied in the analysis are included accounting for correlations and constraints.

Process	SR `plus`	SR `minus`
tq	169 000 ± 6000	150 ± 150
$\bar{t}q$	90 ± 90	109 000 ± 4000
$tW+\bar{t}W, t\bar{b}+\bar{t}b$	51 000 ± 4000	49 000 ± 4000
$t\bar{t}$	265 000 ± 14 000	265 000 ± 14 000
W+$b\bar{b}$	198 000 ± 21 000	159 000 ± 17 000
W+$c(\bar{c})$	60 000 ± 13 000	49 000 ± 11 000
Z+jets, diboson	21 000 ± 4000	19 000 ± 4000
Multijet	50 000 ± 10 000	50 000 ± 10 000
Total	814 000 ± 2100	698 800 ± 2000
Observed	814 185	698 845

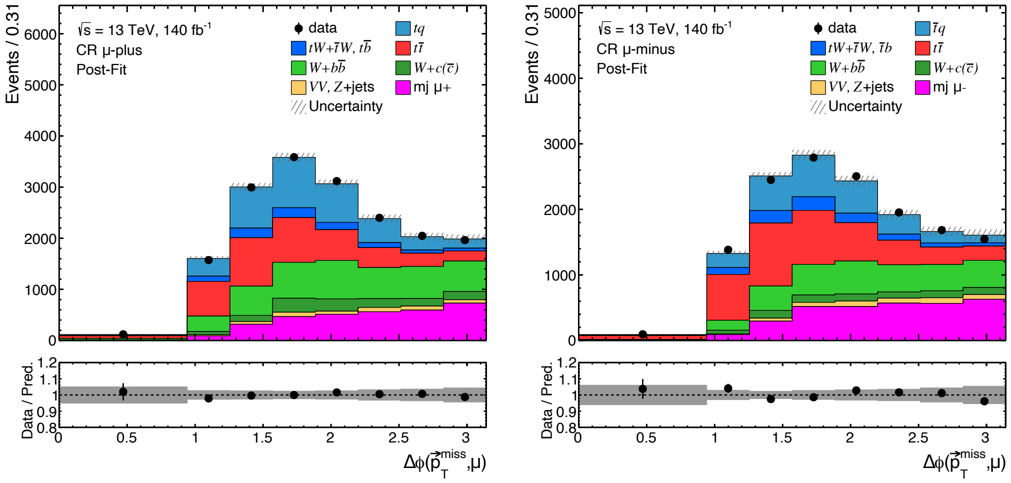

(a) CR μ-`plus`

(b) CR μ-`minus`

Figure 9.6.: Histogram of the muon CR distribution comparing data and simulation, with all nuisance and signal parameters set to their ML estimators. The uncertainty band represents the aggregated MC uncertainty, taking into account correlations among the ML estimators. The bottom plot displays the ratio of observed events to the predicted count for each bin.

9.8.1. Nuisance Parameters

The ML estimators for the nuisance parameters, along with their uncertainties, provide insights into the fit quality. When the values of nuisance parameters determined in the fit exhibit uncertainties less than one, it suggests the data in the analysis does not agree with the variability allowed by the auxiliary measurement. Consequently, the parameters can be constrained in the fit. Such constraints typically denote a reduction in uncertainty, which is favorable. However, there are scenarios where constraints might not be desired. For instance, the constraint of the shower uncertainty is one such scenario. Its uncertainty is determined based on the difference between two fixed generator configurations. A significant constraint in this context might not be meaningful, since the uncertainty is not well-defined in the sense of it describing an auxiliary measurement to begin with.

To mitigate the effects of constraining the shower uncertainty and possibly underestimating its impact on the measurement, its normalization and shape contributions are separated and assigned to distinct nuisance parameters. While the shape component experiences a pull and constraint, the normalization com-

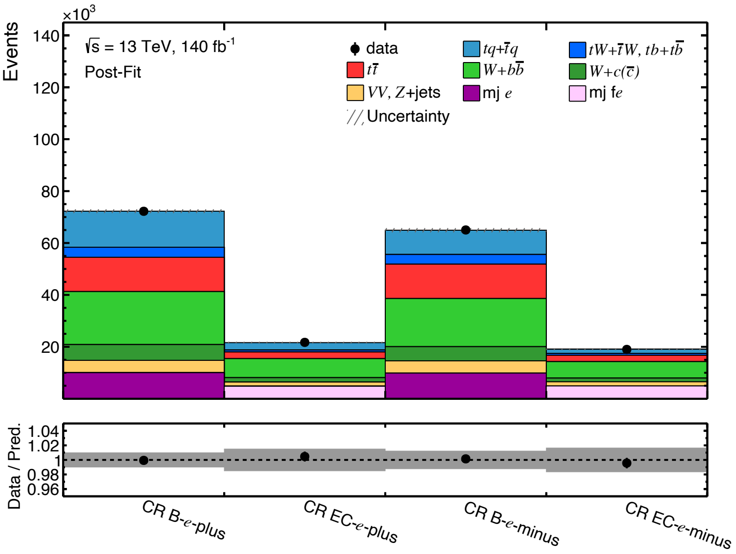

Figure 9.7.: Yields in the electron CRs comparing data and simulation, with all fit parameters set to their ML estimators. The uncertainty band represents the aggregated MC uncertainty, taking into account correlations among the ML estimators. The bottom plot displays the ratio of observed events to the predicted count for each bin.

ponent of the uncertainty remains largely unaffected. As will be discussed later, the normalization component has a considerably larger impact on the measured signal parameters. The uncertainty is further split into its SR and CR components. The same procedure is applied to the shower matching uncertainty.

The ML estimators of the nuisance parameters describing modeling of MC processes are shown in Figure 9.8. Several uncertainties associated with the rates of the W+jets processes exhibit notable pulls and constraints. The $W + b\bar{b}$ process has an assigned rate uncertainty of 40 %, which is expected to be constrained in the measurement. The uncertainty is described by separate nuisance parameters in the positive and negative lepton channel. This results in a post-fit rate uncertainty of 12 %. The pulls indicate an increased rate of 15 % for the positive lepton channel and 21 % for the negative lepton channel.

For the $W + c(\bar{c})$ rate in the positive channel, there is a rate increase of 2 % with no strong constraint observed. Conversely, in the negative channel, the rate decreases by 10 %, again without a significant constraint. Considering the scale uncertainties, the $W + b\bar{b}$ process exhibits a pull of -0.32 for the μ_R scale uncertainty, with a constraint to 62 %. For the μ_F scale uncertainty of the same

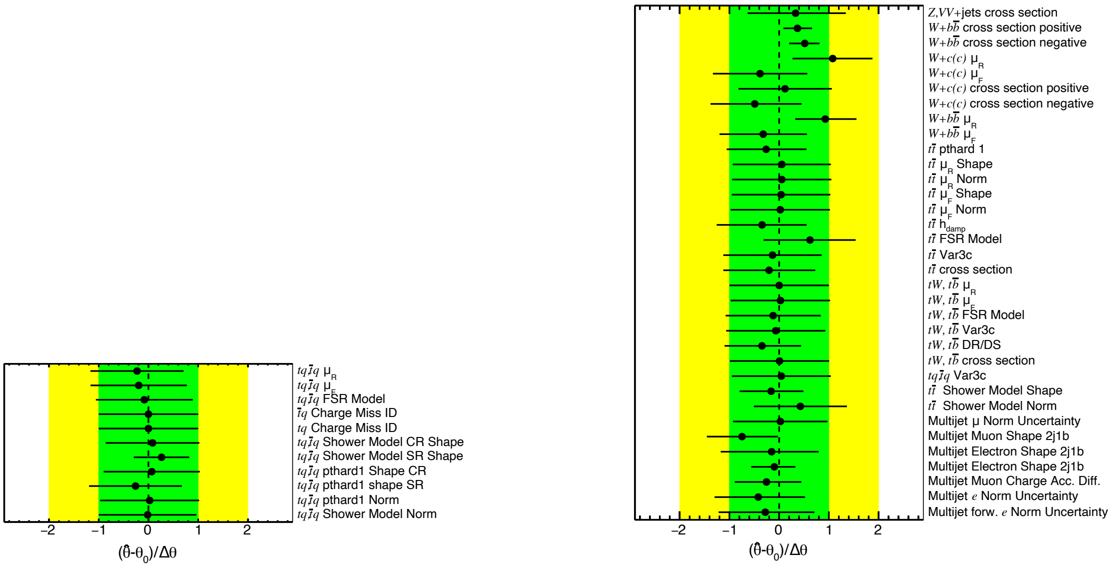

(a) Signal modeling

(b) Background modeling

Figure 9.8.: ML estimators and their uncertainties for the nuisance parameters describing modeling uncertainties.

process, there's a pull of +0.92 and a constraint to 88 %. For the $W + c(\bar{c})$ process, the μ_R scale uncertainty sees a pull of +1.08 and a constraint to 81 %, while the μ_F scale uncertainty experiences a pull of -0.38 and a notable constraint of 95 %.

For the $t\bar{t}$ process, the rate undergoes a slight decrease of 0.8 %, accompanied by a minor constraint to 93 %. Focusing on the h_{damp} uncertainty, a pull of -0.34 is observed with a constraint to 90 %. The FSR Model uncertainty presents a pull of 0.62 and a constraint to 92 %. For the shower model, the normalization uncertainty shows a pull of 0.43 with a constraint to 94 %, while the shape uncertainty records a pull of -0.16, and a constraint to 64 %. The $t\bar{t}$ pthard uncertainty is characterized by a pull of -0.26 and a constraint of 80 %.

The ML estimators of the nuisance parameters describing PDF, JES and JER uncertainties are shown in Figure 9.9. Due to the asymmetric nature of the JER uncertainties the templates of the $+1\sigma$ and -1σ variations are not symmetric in this case. Nuisance parameters that are pulled significantly and correspond to an asymmetric systematic uncertainty can experience an under-constraint where their uncertainty decreases relative to their uncertainty in the auxiliary measurement. This effect is caused by the non-linear impact of the nuisance parameter on the templates, in this case. Here, three of the JER nuisance parameters are

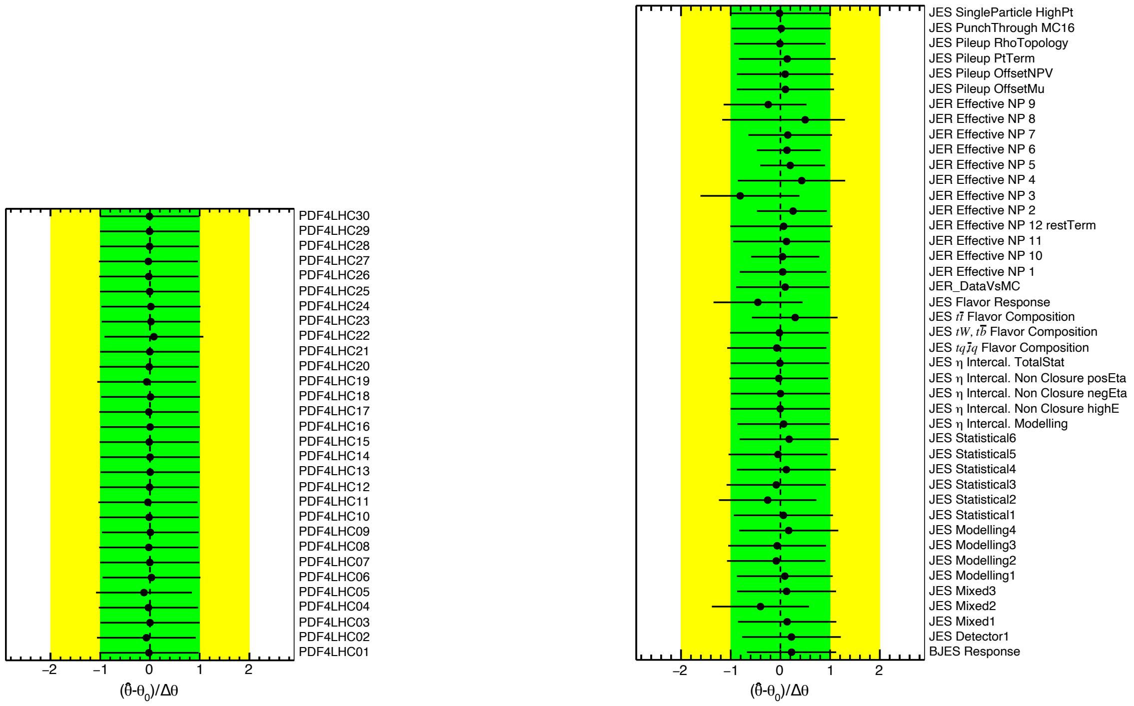

(a) PDF uncertainties

(b) JES and JER uncertainties

Figure 9.9.: ML estimators and their uncertainties for the nuisance parameters describing PDF uncertainties in the left plot and JES and JER uncertainties in the right plot.

pulled and show a subsequent under-constraint. The profile likelihood function of these parameters is evaluated at a range of points to verify the likelihood does not exhibits jumps.

The ML estimators of the nuisance parameters describing the luminosity and lepton uncertainties are shown in Figure 9.10. The luminosity nuisance parameter is neither constrained nor pulled and the lepton scale factor uncertainties only show minor pulls and no strong constraints.

The values and uncertainties of the γ factors, the nuisance parameters describing the statistical uncertainty of the MC samples are shown in Figure 9.11.

Finally, the ML estimators of the nuisance parameters and signal parameters can be applied to the MC prediction to compare the agreement of measured data to MC data in the neural network input distributions. The uncertainty in this case is calculated using the correlation between the fitted parameters. Since

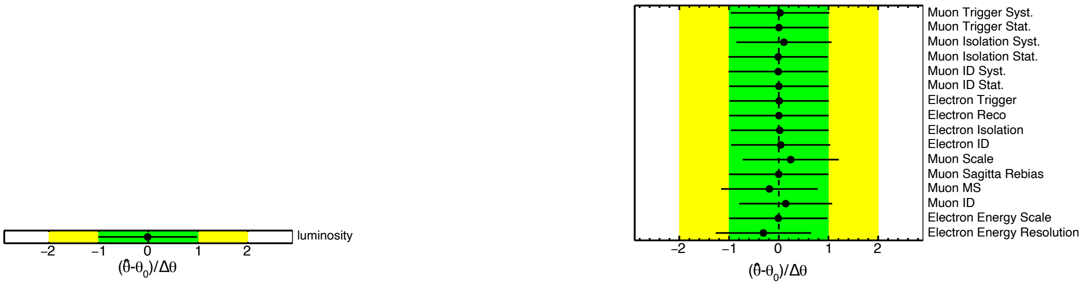

(a) Luminosity uncertainty

(b) Lepton uncertainties

Figure 9.10.: ML estimators and their uncertainties for the nuisance parameters describing luminosity uncertainty in the left plot and lepton uncertainties in the right plot.

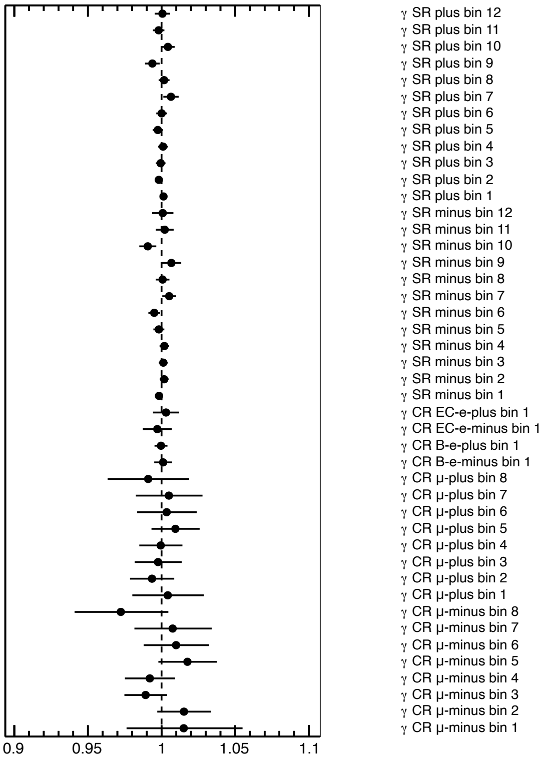

Figure 9.11.: ML estimators and their uncertainties for the nuisance parameters γ describing the statistical uncertainty of the simulation.

the parameters are determined for the fit to the D_{nn} distributions, applying the resulting parameters in other distributions does not guarantee a good agreement between measured data and simulation. This discrepancy arises because the correlations and constraints on the nuisance parameters might vary if the fit were performed directly using the input variables.

Nevertheless, it can be insightful to check how the agreement in the input variables of the neural network is affected by the values, constraints and correlations of the parameters determined in the fit. The Figures 9.12 to 9.14 showcase the total MC prediction compared to data for each input variable to the neural network in the SR `plus`. The corresponding comparisons for the SR `minus` are given in Appendix A.

The post-fit agreement for most neural network input variables is satisfactory, as indicated by the χ^2 test outlined in Section 7.1. However, the distributions for $|\eta(\ell)|$ and $|\Delta p_{\mathrm{T}}(\ell, j)|$ exhibit p-values below 5 %. It is important to interpret these results within the context of the assumed correlations among nuisance parameters, which are derived from the fit to the D_{nn} distributions. Additionally, it should be noted that the bin values of the MC prediction in the post-fit plots are often highly correlated, a factor not visually represented in the plots but accounted for in the χ^2 test. This correlation can result in high p-values for distributions with apparent simultaneous discrepancies between the simulation and data across multiple adjacent bins, and low p-values where the agreement between data and MC prediction is good in each individual bin.

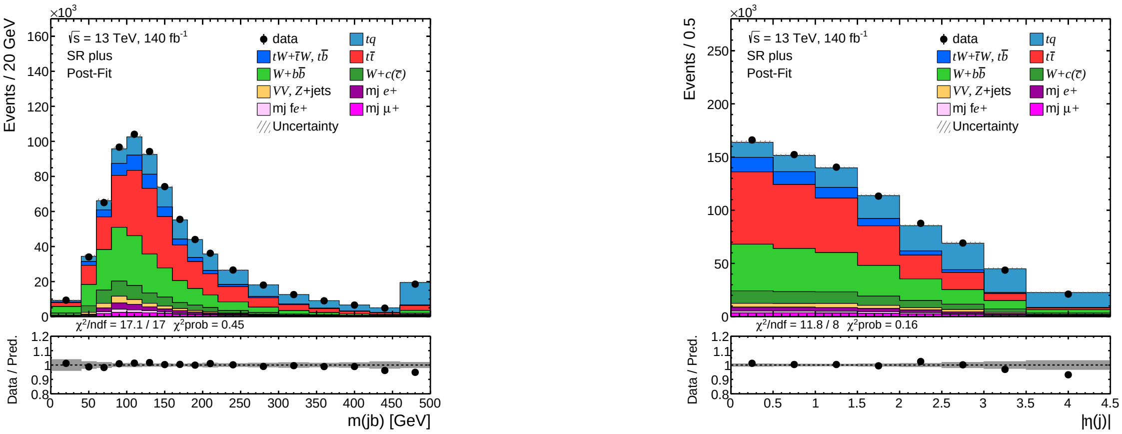

(a) m(jb) (b) $|\eta(j)|$

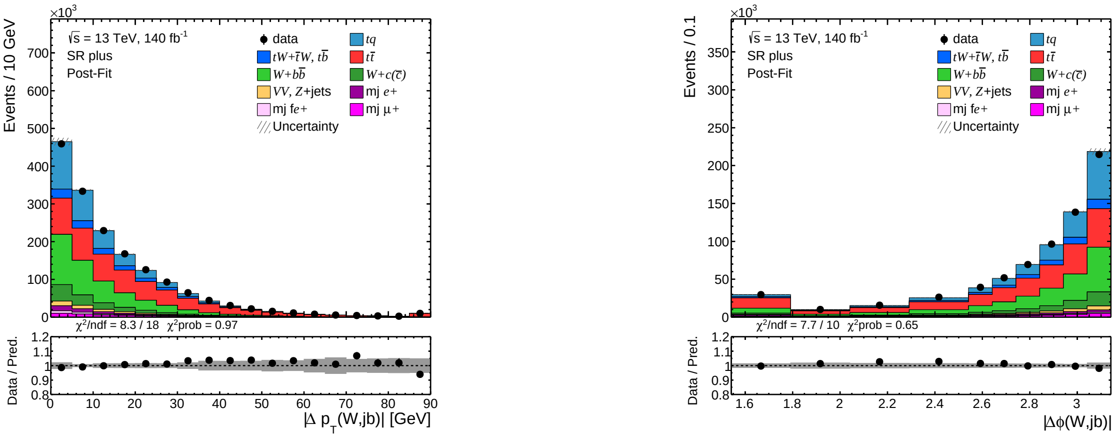

(c) $|\Delta p_{\mathrm{T}}(W, jb)|$ (d) $|\Delta\phi(W, jb)|$

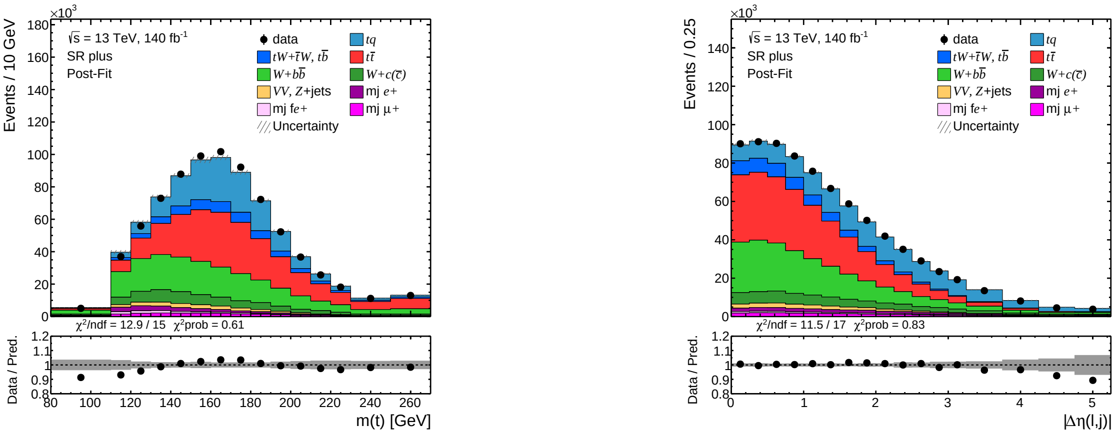

(e) $m(t)$ (f) $|\Delta\eta(\ell, j)|$

Figure 9.12.: Distributions of the first six input variables of the neural network comparing data and simulation in the SR `plus`. All nuisance and signal parameters are set to their ML estimators.

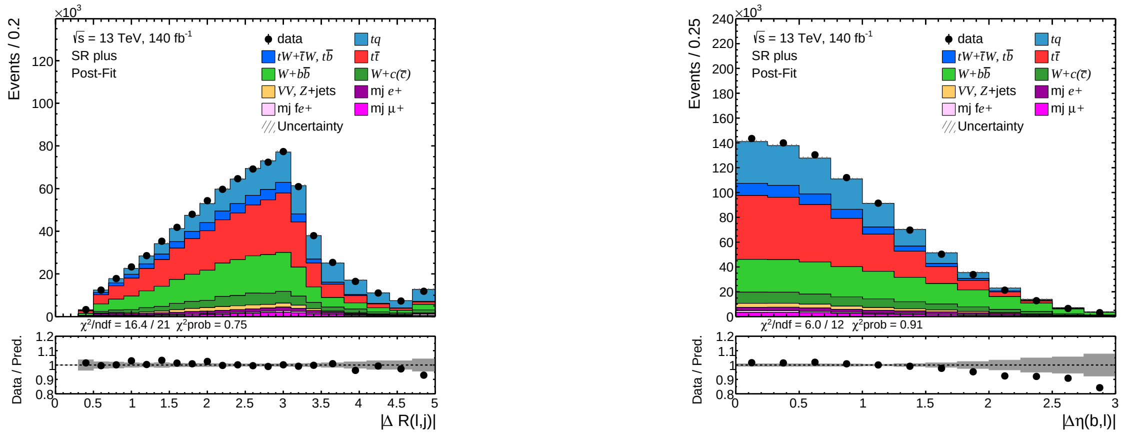

(a) $\Delta R(\ell, j)$ (b) $|\Delta\eta(b, \ell)|$

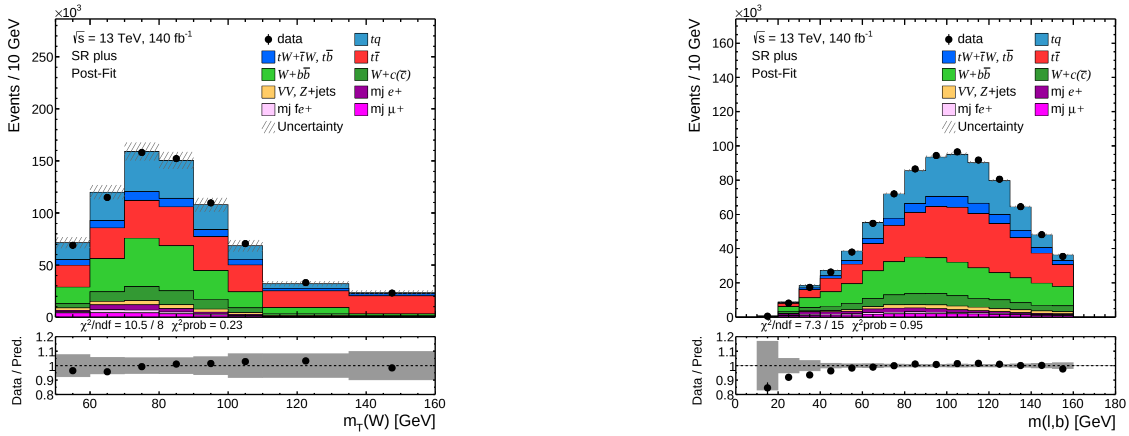

(c) $m_{\mathrm{T}}(W)$ (d) $m(\ell b)$

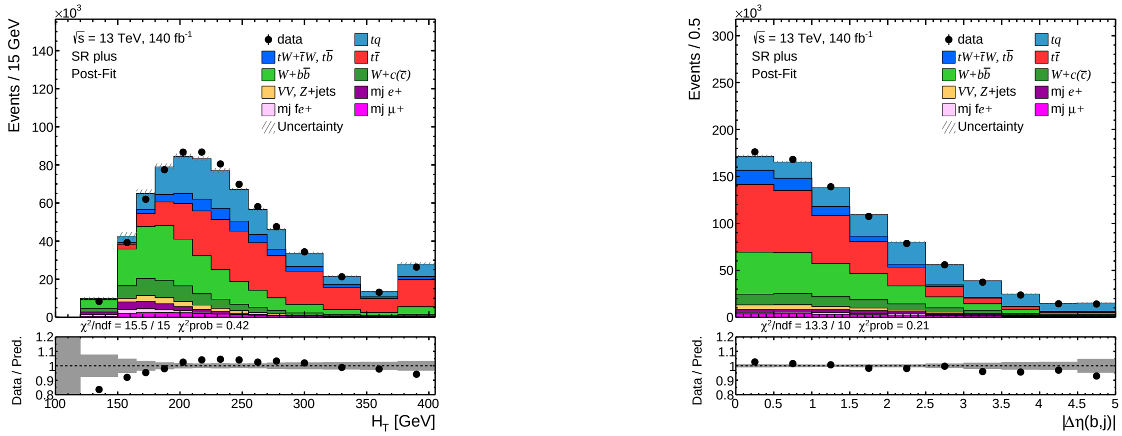

(e) H_{T} (f) $|\Delta\eta(b, j)|$

Figure 9.13.: Distributions of the seventh to twelfth input variable of the neural network comparing data and simulation in the SR `plus`. All nuisance and signal parameters are set to their ML estimators.

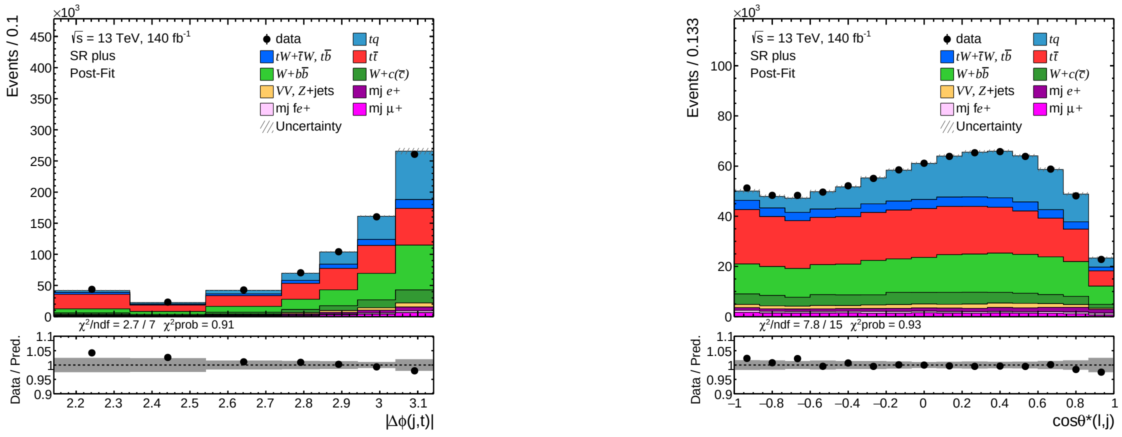

(a) $|\Delta\phi(j,t)|$

(b) $\cos\theta^*(\ell,j)$

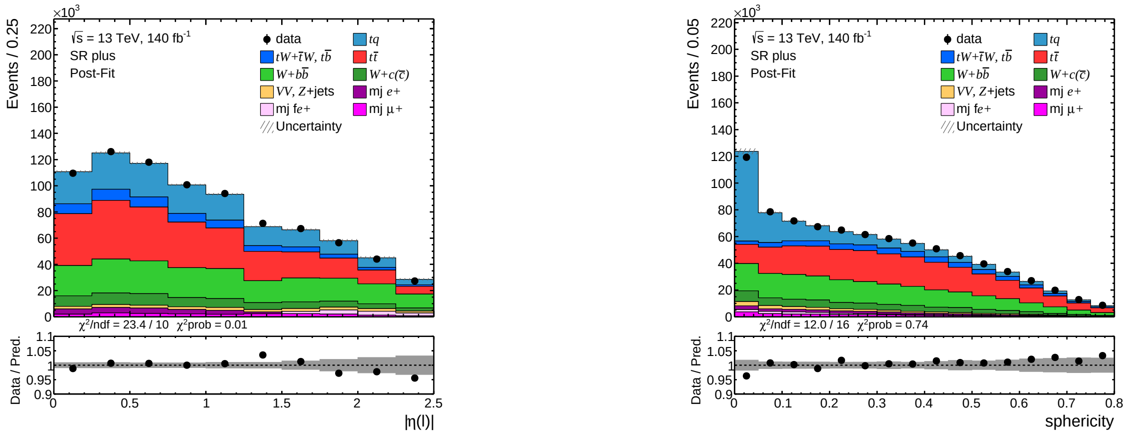

(c) $|\eta(\ell)|$

(d) sphericity

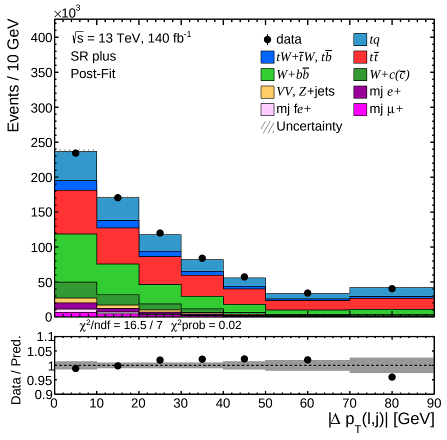

(e) $|\Delta p_{\mathrm{T}}(\ell,j)|$

Figure 9.14.: Distributions of the last five input variables of the neural network comparing data and simulation in the SR `plus`. All nuisance and signal parameters are set to their ML estimators.

9.8.2. Correlation of Fit Parameters

The fitting procedure estimates all parameters of the likelihood function. During this minimization process, the covariance matrix, which describes the linear correlation between the estimated values, is determined. Figure 9.15 displays the correlations for the parameter set where at least one correlation coefficient exceeds 0.3.

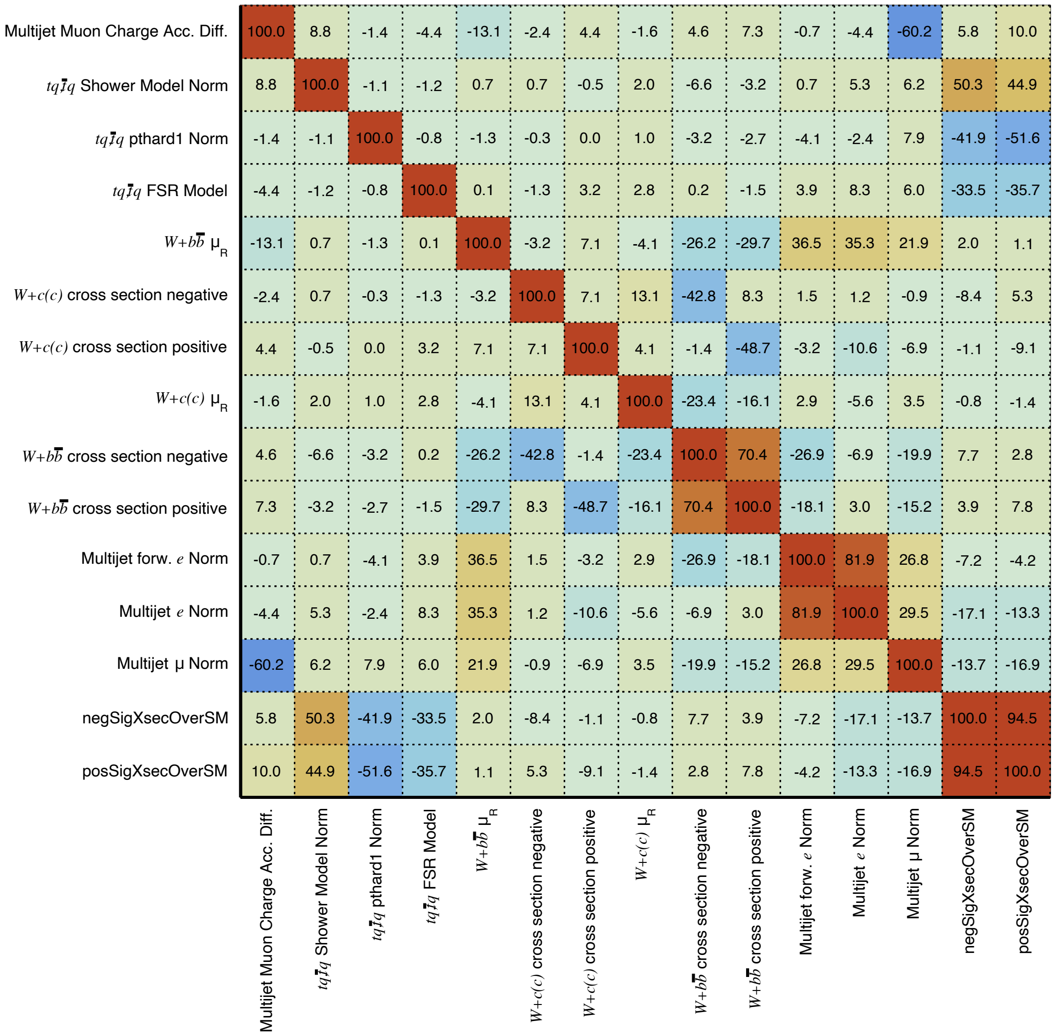

	Multijet Muon Charge Acc. Diff.	$tq\bar{t}q$ Shower Model Norm	$tq\bar{t}q$ pthard1 Norm	$tq\bar{t}q$ FSR Model	$W{+}b\bar{b}$ μ_R	$W{+}c(c)$ cross section negative	$W{+}c(c)$ cross section positive	$W{+}c(c)$ μ_R	$W{+}b\bar{b}$ cross section negative	$W{+}b\bar{b}$ cross section positive	Multijet forw. e Norm	Multijet e Norm	Multijet μ Norm	negSigXsecOverSM	posSigXsecOverSM
Multijet Muon Charge Acc. Diff.	100.0	8.8	-1.4	-4.4	-13.1	-2.4	4.4	-1.6	4.6	7.3	-0.7	-4.4	-60.2	5.8	10.0
$tq\bar{t}q$ Shower Model Norm	8.8	100.0	-1.1	-1.2	0.7	0.7	-0.5	2.0	-6.6	-3.2	0.7	5.3	6.2	50.3	44.9
$tq\bar{t}q$ pthard1 Norm	-1.4	-1.1	100.0	-0.8	-1.3	-0.3	0.0	1.0	-3.2	-2.7	-4.1	-2.4	7.9	-41.9	-51.6
$tq\bar{t}q$ FSR Model	-4.4	-1.2	-0.8	100.0	0.1	-1.3	3.2	2.8	0.2	-1.5	3.9	8.3	6.0	-33.5	-35.7
$W{+}b\bar{b}$ μ_R	-13.1	0.7	-1.3	0.1	100.0	-3.2	7.1	-4.1	-26.2	-29.7	36.5	35.3	21.9	2.0	1.1
$W{+}c(c)$ cross section negative	-2.4	0.7	-0.3	-1.3	-3.2	100.0	7.1	13.1	-42.8	8.3	1.5	1.2	-0.9	-8.4	5.3
$W{+}c(c)$ cross section positive	4.4	-0.5	0.0	3.2	7.1	7.1	100.0	4.1	-1.4	-48.7	-3.2	-10.6	-6.9	-1.1	-9.1
$W{+}c(c)$ μ_R	-1.6	2.0	1.0	2.8	-4.1	13.1	4.1	100.0	-23.4	-16.1	2.9	-5.6	3.5	-0.8	-1.4
$W{+}b\bar{b}$ cross section negative	4.6	-6.6	-3.2	0.2	-26.2	-42.8	-1.4	-23.4	100.0	70.4	-26.9	-6.9	-19.9	7.7	2.8
$W{+}b\bar{b}$ cross section positive	7.3	-3.2	-2.7	-1.5	-29.7	8.3	-48.7	-16.1	70.4	100.0	-18.1	3.0	-15.2	3.9	7.8
Multijet forw. e Norm	-0.7	0.7	-4.1	3.9	36.5	1.5	-3.2	2.9	-26.9	-18.1	100.0	81.9	26.8	-7.2	-4.2
Multijet e Norm	-4.4	5.3	-2.4	8.3	35.3	1.2	-10.6	-5.6	-6.9	3.0	81.9	100.0	29.5	-17.1	-13.3
Multijet μ Norm	-60.2	6.2	7.9	6.0	21.9	-0.9	-6.9	3.5	-19.9	-15.2	26.8	29.5	100.0	-13.7	-16.9
negSigXsecOverSM	5.8	50.3	-41.9	-33.5	2.0	-8.4	-1.1	-0.8	7.7	3.9	-7.2	-17.1	-13.7	100.0	94.5
posSigXsecOverSM	10.0	44.9	-51.6	-35.7	1.1	5.3	-9.1	-1.4	2.8	7.8	-4.2	-13.3	-16.9	94.5	100.0

Figure 9.15.: The correlation matrix for the fit to the inclusive cross-sections expressed in percentages. The signal parameters are denoted as posSigXsecOverSM for $\sigma(tq)$ and negSigXsecOverSM for $\sigma(\bar{t}q)$.

Many systematic uncertainties influence both the positive and negative signal parameters, leading to a significant correlation between them. The correlation coefficient, determined by the Hesse algorithm during the maximization process, is found to be 95 %. This coefficient, along with the values and uncertainties of the signal parameters, enables the calculation of values and uncertainties for an alternative parametrization using μ_{R_t} and μ_{tch}. However, as the correlation coefficient represents only the linear correlation between the parameters, the direct determination of uncertainties through the profile likelihood method is more precise. Therefore, this calculation mainly serves as a cross-check to ensure the consistency of results across both parametrizations in cases of high parameter correlation. These two approaches – using the correlation coefficient and the profile likelihood method – yield results that are in agreement, thus validating the consistency of the parametrizations.

Furthermore, the correlation coefficient between μ_{R_t} and μ_{tch} is determined to be $-28\,\%$. This indicates that the correlation between signal parameters is substantially reduced in the second parametrization. From this perspective, the parametrization using μ_{R_t} and μ_{tch} proves more advantageous than the first one. It allows for the precise measurement of one parameter, while many uncertainties predominantly affect the other, reducing the correlation of the two signal parameters.

9.8.3. Stability of the Measurement

The measurement utilizes the comprehensive dataset from the full Run 2 period, spanning 2015-2018. To ensure the robustness of the results, it is beneficial to perform the analysis on subsets of the data, partitioned according to the periods in which they were recorded. This method allows for the verification of the consistency of the results across different time-frames. Such a temporal analysis is particularly valuable in identifying and addressing any systematic uncertainties that may have been present exclusively during certain periods. Therefore, this comparison not only serves as a check for consistency but also as a diagnostic tool for potential unaccounted systematic errors. The dataset is divided into three subsets: mc16a, which includes data from 2015 and 2016; mc16d, which includes data from 2017; and mc16e, which includes data from 2018.

The differences in the signal parameters relative to the nominal fit are illustrated in Figure 9.16 for μ_{tq} and $\mu_{\bar{t}q}$ and Figure 9.17 for $\mu_{tq+\bar{t}q}$ and μ_{R_t}. The fits are executed for each subset, and the signal parameters are compared using both parametrizations. This approach helps in assessing the temporal stability of the

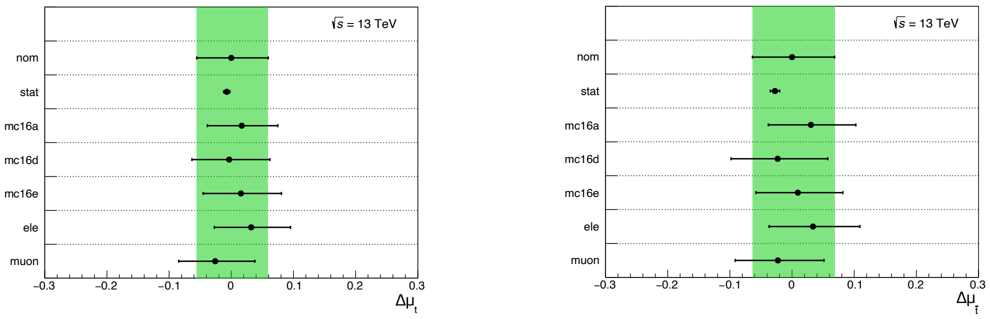

(a) μ_{tq}

(b) $\mu_{\bar{t}q}$

Figure 9.16.: Differences in fitted signal parameters μ_{tq} and $\mu_{\bar{t}q}$ for different subdatasets across the time periods mc16a (2015+2016), mc16d (2017) and mc16e (2018) of data collection. The nominal measurement is labeled *nom* and the fit with only statistical uncertainty *stat*.

measurement and in identifying any deviations that might suggest the presence of time-dependent systematic effects.

An additional method for testing stability is to divide the dataset based on the type of selected lepton in the events, creating subsets of either muon or electron events. This approach is beneficial, as the detection efficiencies and systematic uncertainties often vary between muon and electron events. Consistent results from these subsets further validate the measurement's reliability.

Moreover, for comparative purposes, the signal parameters obtained from a fit that includes only statistical uncertainties are also presented in the plots. This fit, which excludes systematic uncertainties, shows agreement with the nominal fit, providing further confirmation of the analysis's robustness. These stability tests, by dissecting the dataset into different temporal and physical subsets, provide a comprehensive check on the measurement's reliability.

9.8.4. Analysis of Systematic Uncertainties

To understand how the precision of the measurement result is impacted by uncertainties different measures are compared. The impact of a group of uncertainties is determined by repeating the fit fixing the nuisance parameters contained in the group to their nominal value. This leads to a reduced uncertainty σ_{red} on the signal parameter since the group of uncertainties is effectively removed. The impact is determined by subtracting the squared uncertainties from each

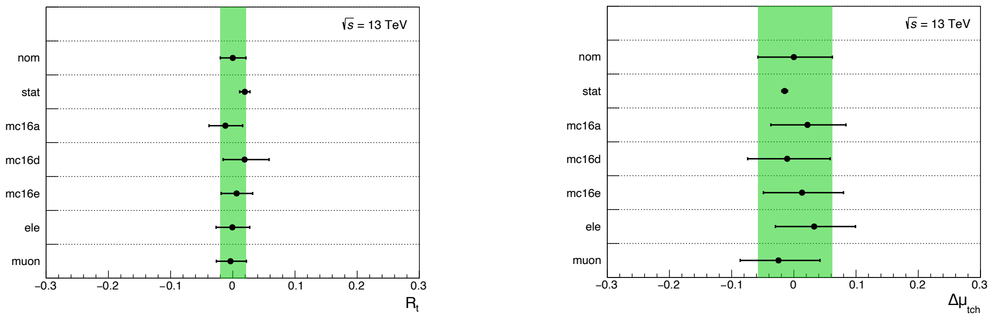

(a) μ_{R_t}

(b) $\mu_{tq+\bar{t}q}$

Figure 9.17.: Differences in fitted signal parameters μ_{tq} and $\mu_{\bar{t}q}$ for different sub-datasets across the time periods mc16a (2015+2016), mc16d (2017) and mc16e (2018) of data collection. The nominal measurement is labeled *nom* and the fit with only statistical uncertainty *stat*.

other:

$$\Delta\sigma = \sqrt{\sigma_{\mathrm{nom}}^2 - \sigma_{\mathrm{red}}^2}$$

The impact of different groups of uncertainties on the uncertainty of the signal parameter is summarized in Table 9.2.

Table 9.2.: The impact of different groups of systematic uncertainties on $\sigma(tq)$, $\sigma(\bar{t}q)$, $\sigma(tq+\bar{t}q)$ and R_t given in %.

Uncertainty group	$\frac{\Delta\sigma(tq)}{\sigma(tq)}$	$\frac{\Delta\sigma(\bar{t}q)}{\sigma(\bar{t}q)}$	$\frac{\Delta\sigma(tq+\bar{t}q)}{\sigma(tq+\bar{t}q)}$	$\frac{\Delta R_t}{R_t}$
Data statistical	$+0.4$ / -0.4	$+0.5$ / -0.5	$+0.3$ / -0.3	$+0.6$ / -0.6
Signal modelling	$+4.9$ / -4.5	$+5.2$ / -4.7	$+5.0$ / -4.6	$+0.9$ / -0.9
Background modelling	$+1.8$ / -1.6	$+2.1$ / -1.9	$+1.8$ / -1.6	$+1.5$ / -1.4
MC statistical	$+1.1$ / -1.0	$+1.4$ / -1.3	$+1.2$ / -1.1	$+0.8$ / -0.8
PDFs	$+0.4$ / -0.4	$+1.2$ / -1.0	$+0.7$ / -0.6	$+0.9$ / -0.8
Jets	$+2.2$ / -2.0	$+3.0$ / -2.7	$+2.5$ / -2.3	$+1.0$ / -0.9
b-tagging	$+1.6$ / -1.5	$+1.7$ / -1.5	$+1.6$ / -1.5	$+0.2$ / -0.1
Leptons	$+1.1$ / -1.0	$+1.1$ / -1.0	$+1.1$ / -1.0	$+0.1$ / -0.1
Luminosity	$+0.9$ / -0.8	$+0.9$ / -0.9	$+0.9$ / -0.8	< 0.1
Total	$+5.9$ / -5.5	$+6.6$ / -6.2	$+6.1$ / -5.7	$+2.2$ / -2.1

Systematic uncertainties are ranked based on their impact on the signal parameter, as illustrated in Figures 9.18 and 9.19. To determine the impact of

Table 9.3.: The impact of the eight most significant systematic uncertainties on $\sigma(tq)$, $\sigma(\bar{t}q)$, and $\sigma(tq + \bar{t}q)$ is presented in percentages. The sequence of the uncertainties is determined by their impact on $\sigma(tq + \bar{t}q)$.

Systematic uncertainty	$\frac{\Delta\sigma(tq)}{\sigma(tq)}$	$\frac{\Delta\sigma(\bar{t}q)}{\sigma(\bar{t}q)}$	$\frac{\Delta\sigma(tq+\bar{t}q)}{\sigma(tq+\bar{t}q)}$
tq matching scale definition, rate	-2.9 / +3.0	-2.6 / +2.7	-2.8 / +2.9
tq parton shower, rate	+2.6 / -2.5	+3.3 / -3.1	+2.9 / -2.7
tq final-state radiation	-2.0 / +2.1	-2.1 / +2.2	-2.0 / +2.1
tq matching scale definition, shape	-1.5 / +1.6	-1.2 / +1.2	-1.4 / +1.4
JES η intercalibration modelling	-1.1 / +1.2	-1.5 / +1.5	-1.3 / +1.3
b-tagging NP B1	+1.0 / -0.9	+1.0 / -1.0	+1.0 / -1.0
b-tagging NP B0	+1.0 / -0.9	+1.0 / -1.0	+1.0 / -1.0
barrel electron multijet, rate	+0.9 / -1.1	+0.8 / -0.8	+0.8 / -0.9

each systematic uncertainty on the signal parameter, the corresponding nuisance parameter is varied by 1σ. The likelihood function is then maximized with respect to all other parameters, and the deviation of the signal parameter from its nominal fit value is assessed. Both pre-fit impacts (where nuisance parameters are adjusted by their pre-fit uncertainty) and post-fit impacts (adjusted by post-fit uncertainty) are presented. The cross-section measurements are most impacted by signal modeling uncertainties, the pthard1 uncertainty and the shower model uncertainty. In both cases the normalization components of these uncertainties are the ones that have a high impact on the signal. These nuisance parameters obtain fitted values close to their nominal value in the fit, indicating a low

Table 9.4.: The impact of the eight most important systematic uncertainties on R_t in %.

Systematic uncertainty	$\Delta R_t / R_t$
$W^- + c(\bar{c})$ cross-section	+0.81 / -0.78
tq parton shower, rate	-0.67 / +0.65
$W^+ + c(\bar{c})$ cross-section	-0.46 / +0.46
PDF eigenvector 09	-0.45 / +0.46
MC statistical uncertainty SR `minus` bin 10	+0.41 / -0.40
JES η intercalibration modelling	+0.37 / -0.38
tq matching scale definition, shape	-0.36 / +0.38
PDF eigenvector 05	+0.37 / -0.35

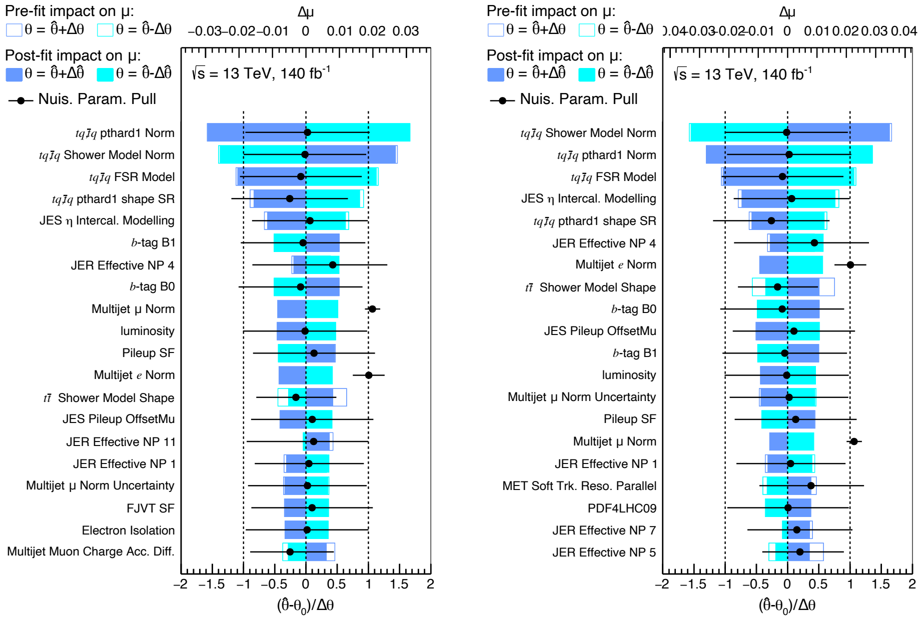

Figure 9.18.: Systematic uncertainties are ranked based on their impact on the signal parameters. The left panel shows the impact on top-quark production and the right on top-antiquark production. The upper axis corresponds to the impact on the signal, with pre-fit values represented by unfilled bars and post-fit values by filled bars. The lower axis corresponds to the pulls and constraints of the nuisance parameters, depicted by black points and error bars.

change in the signal parameter values. High impacting detector uncertainties are the JES η intercalibration modeling uncertainty, b-tagging uncertainties and JER components.

For R_t the $W + c(\bar{c})$ rate uncertainty and signal shower model uncertainty have the biggest impact. Also, PDF uncertainties and MC statistical uncertainties have significant impacts on R_t. The difference in which systematic uncertainties are most impacting for the cross-sections and R_t comes from a cancellation in R_t. Many uncertainties have a similar and correlated impact on the positive and negative cross-section leading to a strongly reduced impact on their ratio R_t.

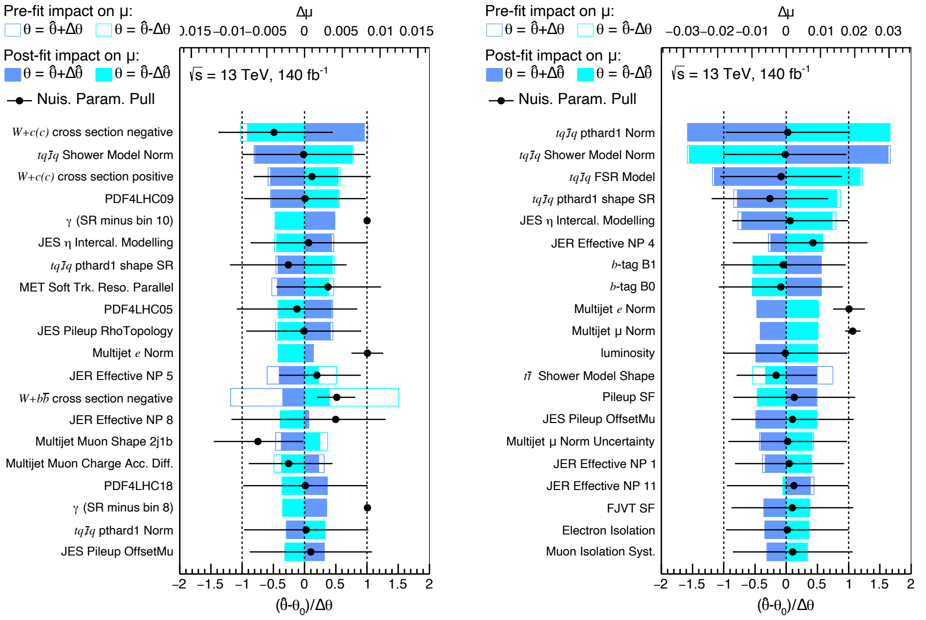

Figure 9.19.: Systematic uncertainties are ranked based on their impact on the signal parameters. The left panel shows the impact on μ_{R_t} and the right on the total cross-section of the t-channel production. The upper axis corresponds to the impact, with pre-fit values represented by unfilled bars and post-fit values by filled bars. The lower axis corresponds to the pulls and constraints of the nuisance parameters, depicted by black points and error bars

9.8.5. Mass Dependence

The templates for single-top-quark processes are influenced by the assumed top-quark mass, which affects the cross-section, acceptance, and the distribution shapes used in the fit. To assess the impact of top-quark mass variations on the measured signal parameter, the fit is repeated with templates generated for different top-quark masses. Alternative samples for all top-quark production processes are created, assuming top-quark masses of 171 GeV and 174 GeV.

In this mass-dependence study, all uncertainties are re-evaluated with the varied top quark mass, except for modeling uncertainties defined by different MC generators. Figure 9.20 compares the distributions of the reconstructed top quark mass across different signal process samples. The peak of the reconstructed top-quark mass distribution shifts to higher or lower values depending on the assumed mass. Additionally, many NN input variables are also affected by the top-quark mass, thereby influencing the NN distribution.

The resulting measured cross-sections are presented in Table 9.5. The effect of the top-quark mass is quantified by fitting a linear function to the measured cross-sections as a function of the top-quark mass and determining the slope.

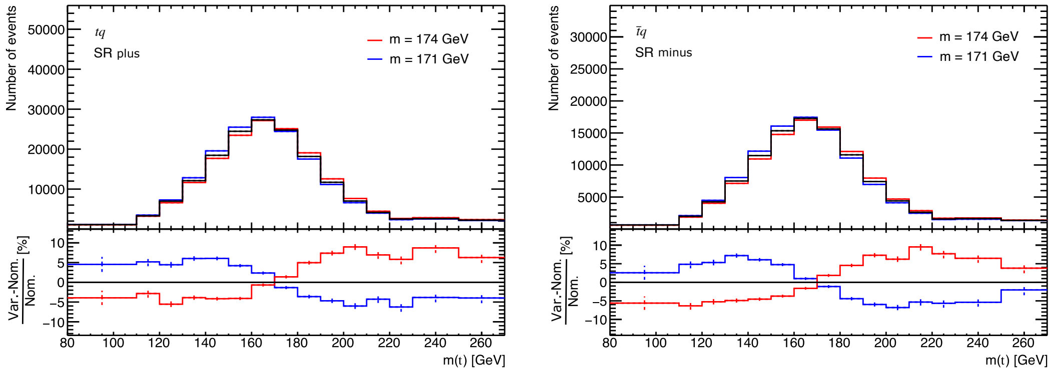

Figure 9.20.: Comparison of $m(t)$ for the nominal and the two mass variations for the signal.

Table 9.5.: The measured cross-section of the t-channel top quark and top antiquark process for different top masses.

Top Mass/GeV	$\sigma(tq)/\text{pb}$	$\sigma(\bar{t}q)/\text{pb}$
171.0	139.8	85.5
172.5	137.5	84.0
174.0	135.4	83.1

The resulting measured cross-sections are illustrated in Figure 9.21. To quantify the effect of the top quark mass, a linear function $f(\Delta m_t) = a \cdot \Delta m_t$ is fitted to the measured cross-sections as a function of the top quark mass, and the slope a is determined.

The fitted parameters, or the slopes, are found to be $a = -1.50\,\text{pb}\,\text{GeV}^{-1}$ for $\sigma(tq)$, $a = -0.85\,\text{pb}\,\text{GeV}^{-1}$ for $\sigma(\bar{t}q)$, and $a = -2.35\,\text{pb}\,\text{GeV}^{-1}$ for $\sigma(tq + \bar{t}q)$. For R_t, the effect of the top quark mass is found to be negligible.

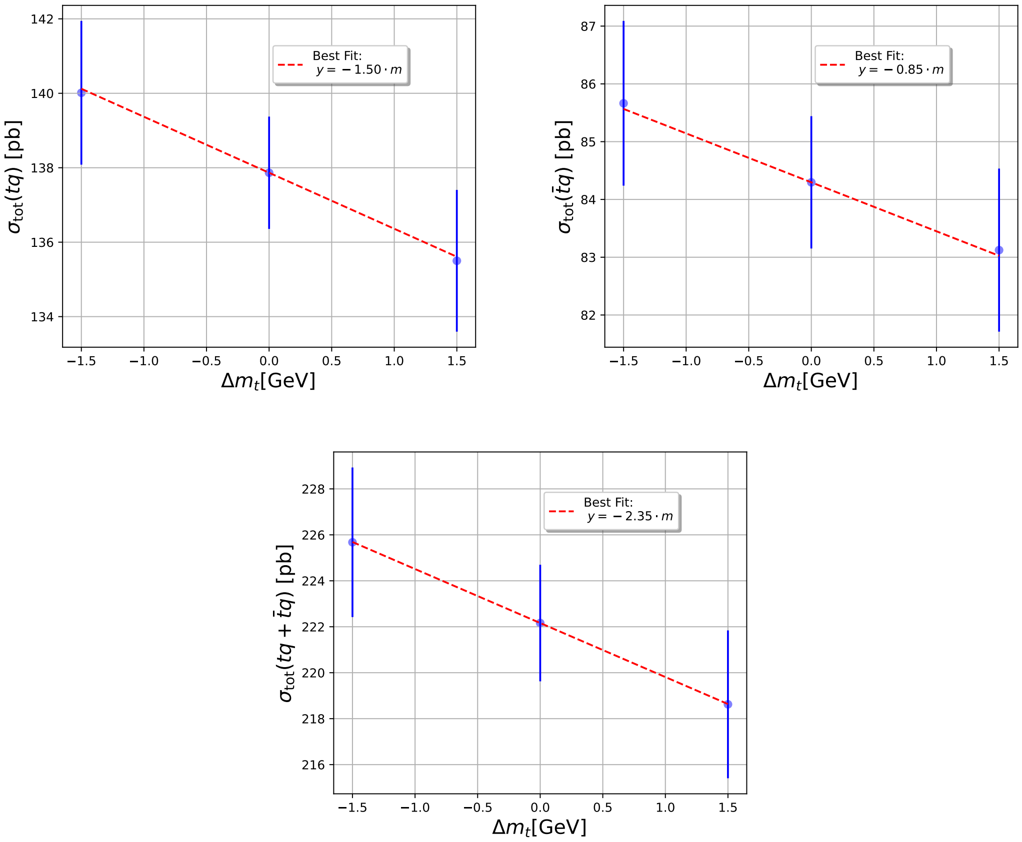

Figure 9.21.: Measured cross-sections for different assumed top masses. Vertical bars indicate the impact of the MC statistical uncertainty on the cross-section.

9.8.6. Goodness of Fit

The high statistical precision of this analysis necessitates a comprehensive description and study of the systematic uncertainties affecting the measurement. Beyond the studies already presented on the setup, behavior of the likelihood function, and the optimization method, it's also possible to directly evaluate the fit quality using a goodness-of-fit test.

To achieve this, a test statistic is formulated utilizing the saturated model [142]. In this approach, an alternative likelihood function is designed with a free parameter for each bin. These parameters adjust the predictions such that the saturated model precisely matches the data after the fitting process. As a result, this model acts as an optimal standard for comparing against the actual likelihood, providing a measure of its accuracy in fitting the data.

According to Neyman and Pearson [143], the most effective test statistic for comparing two hypotheses is the likelihood ratio. When there is a high number of events in each bin, this ratio is approximately χ^2 distributed. Thus, the saturated model is fitted to the data, and the likelihood ratio relative to the nominal maximum likelihood is computed. This likelihood ratio is then interpreted as a χ^2 value to deduce a corresponding p-value.

$$\chi^2 = -2\ln\left(\frac{\mathcal{L}_{\text{nom}}}{\mathcal{L}_{\text{sat}}}\right)$$

The derived χ^2 value results in a p-value of 76 %, indicating that the used likelihood model is compatible with the saturated model.

9.8.7. $|V_{tb}|$ Measurement

The t-channel production of single top quarks is facilitated through the Wtb vertex, a process that could be influenced by new physics. To accommodate this possibility, a form factor f_{LV}, representing a potential non-standard gauge coupling at the Wtb vertex, is introduced, as detailed in Ref. [144]. In the SM, f_{LV} assumes a value of 1.

The cross-section of the t-channel process is proportional to $|f_{\text{LV}} \cdot V_{tb}|^2$, where V_{tb} denotes the corresponding element of the CKM matrix. This analysis does not consider right-handed form factors, thereby assuming that the Wtb interaction is exclusively a left-handed weak coupling, as predicted by the SM.

The methodology employed in this analysis closely mirrors that of the first direct measurement of $|V_{tb}|$, as presented in [145]. An important aspect of measuring $|f_{\text{LV}} V_{tb}|$ in single top-quark production is its independence from the assumed number of quark generations and the unitarity of the CKM matrix. This investigation primarily operates under the assumption that $|V_{tb}|^2$ greatly exceeds $|V_{td}|^2 + |V_{ts}|^2$, implying that the top quark predominantly decays into a b-quark and a W boson ($\mathcal{B}(t \to bW) = 1$). To determine the value of $|f_{\text{LV}} \cdot V_{tb}|$, the experimentally observed t-channel single top-quark production cross-section is divided by the theory prediction of $214.2 \pm 3.4(\text{scale} + \text{PDF}) \pm 1.8(\Delta m_t)$ pb [78]. The calculated value is

$$|f_{\text{LV}} \cdot V_{tb}| \quad = \quad 1.015 \pm 0.031. \tag{9.2}$$

Using this value a 95 % confidence interval can be calculated. For deriving this limit, it is assumed that $|V_{tb}|^2$'s likelihood curve is Gaussian, centered around the measured value, and a uniform prior for $|V_{tb}|^2$ is utilized, set to one within [0, 1] and zero elsewhere, as illustrated in Figure 9.22. The limit of $|V_{tb}|$ can than be calculated by numerically determining the limit l in the equation

$$p_{\mathrm{CL}} = \int_l^1 \mathrm{d}x p(x)$$

where $p_{\mathrm{CL}} = 95\,\%$ is the desired confidence level, $p(x)$ is the probability density of $|V_{tb}|$. The lower limit for $|V_{tb}|$ is established:

$$|V_{tb}| > 0.95$$

at the 95 % confidence level. Theoretically, variations in $|f_{\mathrm{LV}} \cdot V_{tb}|$ can also impact

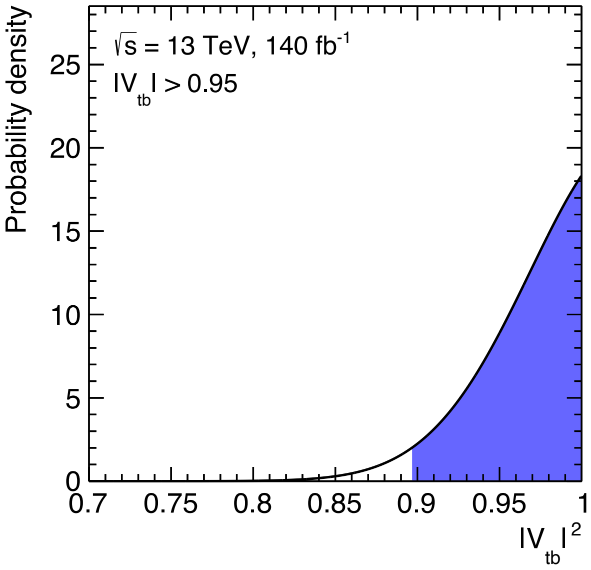

Figure 9.22.: Limit plot illustrating the 95% CL limit on $|V_{tb}|$, when constrained to the range [0,1] as stipulated by the SM and $f_{\mathrm{LV}} = 1$. The determined limit is $|V_{tb}| > 0.95$.

Wt and s-channel production, although their effects are minimal and do not significantly alter the t-channel fit result. Assuming $|f_{\mathrm{LV}} \cdot V_{tb}| = 0.9$ for Wt and s-channel productions yields a total cross-section of 220^{+13}_{-12} pb, sustaining the $|V_{tb}| > 0.95$ limit.

In comparison to the Run 1 combination of ATLAS and CMS, which measured $|f_{\mathrm{LV}} \cdot V_{tb}| = 1.02 \pm 0.04(\text{meas.}) \pm 0.02(\text{theo.})$ [146], the determination presented in this analysis achieves a relative uncertainty that is significantly reduced. Furthermore, a combined analysis of all available measurements from the Tevatron and the LHC prior to this study found a value of 1.014 ± 0.029 [14]. The inclusion of the measurement detailed in this study is expected to further reduce the uncertainty in future combined analyses.

10. Conclusion

In this thesis, the inclusive t-channel single top-quark production cross-sections are measured, along with the ratio of the quark and antiquark cross-section, denoted as R_t. The full Run 2 dataset of $140\,\text{fb}^{-1}$ collected at $13\,\text{TeV}$ with the ATLAS detector at the LHC is used. The measurement represents a direct measurement of the CKM matrix element $|V_{tb}|$ and contributes to the study of the electroweak Wtb vertex. It also relates to the composition of the proton, with R_t being sensitive to the initial state composition.

The event selection focuses on events featuring one lepton, two jets of which exactly one is b-tagged, and missing transverse momentum, which aligns with the signal signature of the t-channel process. This approach effectively reduces the main background contributions, such as the $t\bar{t}$, W+jets, and multijet processes, achieving a signal fraction post-selection of 30 %.

A neural network is utilized to distinguish the signal from the background by combining various kinematic distributions. Systematic uncertainties, arising from both detector and modeling sources, are accounted for throughout the analysis. A binned maximum likelihood fit is utilized to measure the cross-sections and R_t, employing profile likelihood techniques to determine the uncertainties of the measurements. Several studies are conducted analyzing the robustness and consistency of the fit.

The fit is carried out simultaneously in the two SRs and six CRs used to constrain the multijet background normalization in the fit, yielding the following results:

$$\sigma(tq) = 137^{+8}_{-8}\,\text{pb}, \quad \sigma(\bar{t}q) = 84^{+6}_{-5}\,\text{pb}$$

$$\sigma(tq + \bar{t}q) = 221^{+13}_{-13}\,\text{pb} \quad \text{and} \quad R_t = 1.636^{+0.036}_{-0.034}$$

The uncertainties correspond to a relative uncertainty of $+5.9\%$ and -5.5% for $\sigma(tq)$, $+6.6\%$ and -6.2% for $\sigma(\bar{t}q)$, $+6.1\%$ and -5.7% for the combined cross-section and $+2.2\%$ and -2.1% for R_t.

These measurements constitute the first ATLAS measurement of the t-channel cross-section using the full Run 2 dataset. The uncertainties are predominantly systematic, with the most significant impact arising from signal modeling uncertainties for the cross-section measurements and both signal and background modeling uncertainties for R_t.

The measurement is interpreted as a direct measurement of the CKM matrix element $|V_{tb}|$ yielding

$$|f_{\mathrm{LV}} \cdot V_{tb}| \quad = \quad 1.015 \pm 0.031. \tag{10.1}$$

From this a 95 % CL limit of $|V_{tb}|$ is determined as

$$|V_{tb}| > 0.95.$$

This measurement provides a foundation for subsequent interpretations, such as setting constraints on the CKM matrix by considering the effects of $|V_{td}|$ and $|V_{ts}|$, comparing the measured R_t with various theoretical predictions provided by PDFs, and limiting parameters in effective field theory models that describe phenomena beyond the SM.

Future studies are anticipated to extend this analysis to both differential and fiducial cross-section measurements. Additionally, this measurement could be replicated using the forthcoming Run 3 dataset, which is recorded at a center-of-mass energy of 13.6 TeV. While the t-channel cross-section is expected to increase at this higher energy, the $t\bar{t}$ background process exhibits an even more significant increase in cross-section. Given that the measurement is predominantly influenced by systematic uncertainties, a substantial improvement in precision through increased center-of-mass energy or larger data volume is not anticipated. Nevertheless, advancements in the modeling of parton shower simulations and overall MC event generation could enhance the precision of future measurements.

A. Neural network input variable distributions

The Figures A.1 to A.3 show the shapes of the signal process and the main background processes for each variable in MC compared to the data in the negative signal region.

The Figures A.4 to A.6 showcase the total MC prediction compared to data for each input variable to the neural network in the negative signal region.

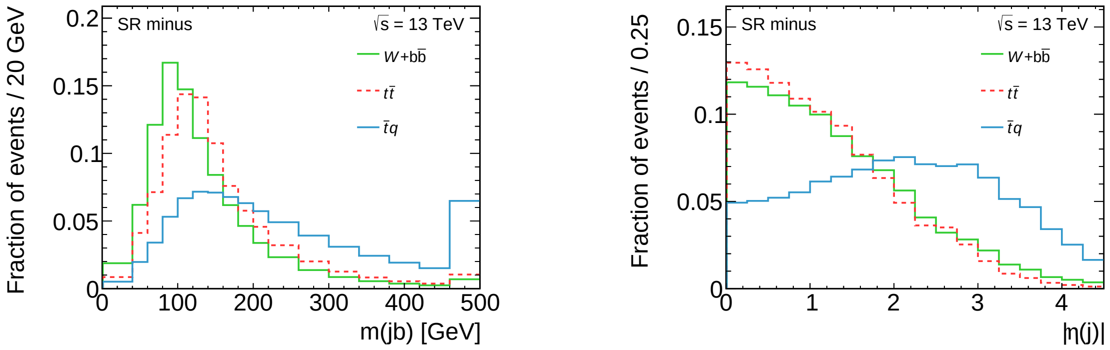

(a) m(jb) (b) $|\eta(j)|$

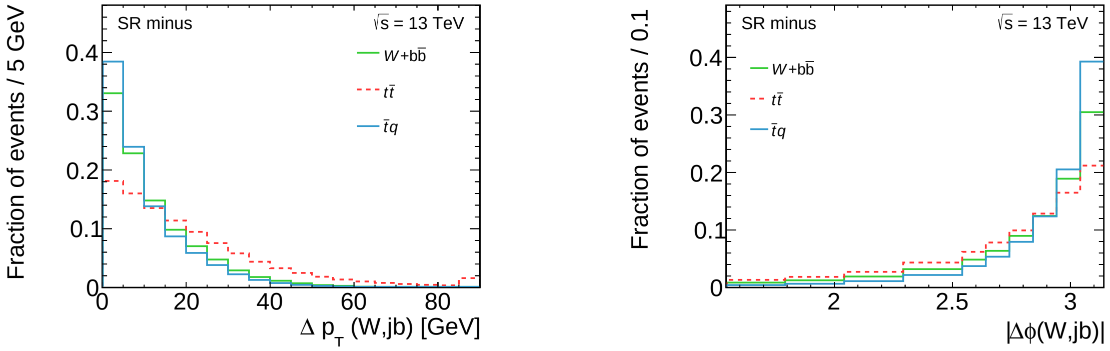

(c) $|\Delta p_{\mathrm{T}}(W, jb)|$ (d) $|\Delta\phi(W, jb)|$

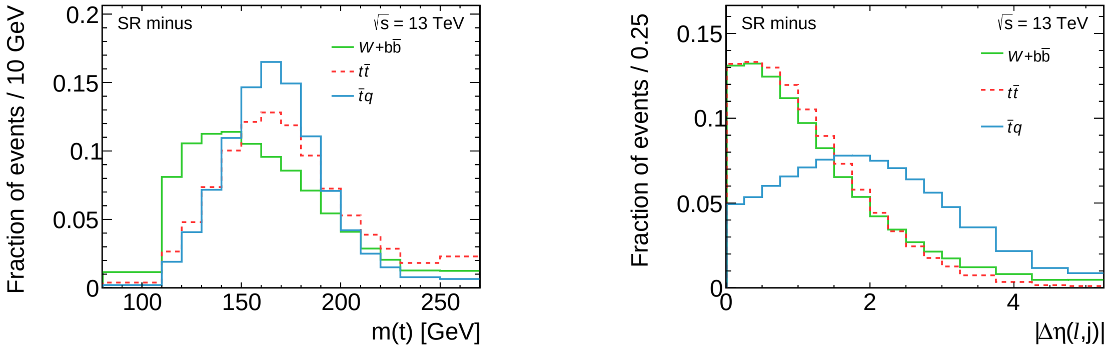

(e) $m(t)$ (f) $|\Delta\eta(\ell, j)|$

Figure A.1.: Shapes of the first six neural network input variable distributions for the signal process and the main background processes in the SR `minus`.

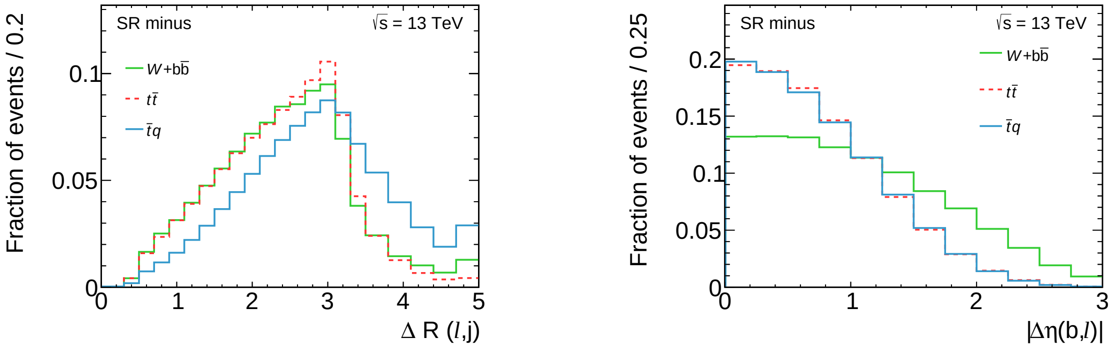

(a) $\Delta R(\ell, j)$ (b) $|\Delta\eta(b, \ell)|$

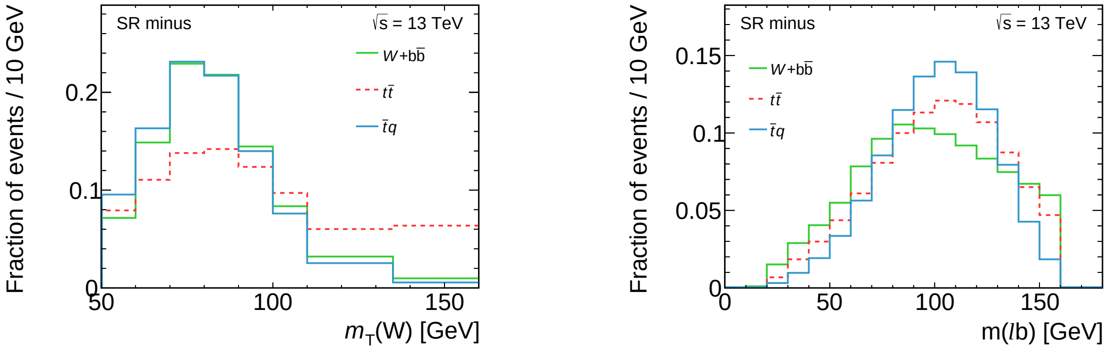

(c) $m_{\mathrm{T}}(W)$ (d) $m(\ell b)$

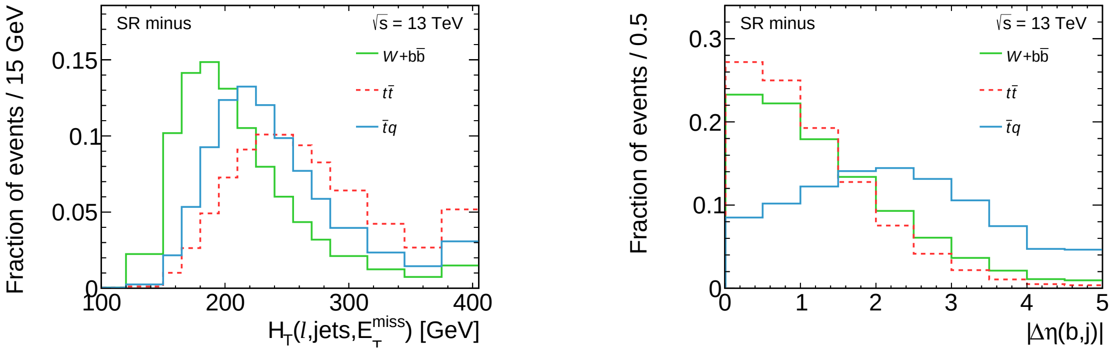

(e) H_{T} (f) $|\Delta\eta(b, j)|$

Figure A.2.: Shapes of the seventh to twelfth neural network input variable distribution for the signal process and the main background processes in the SR `minus`.

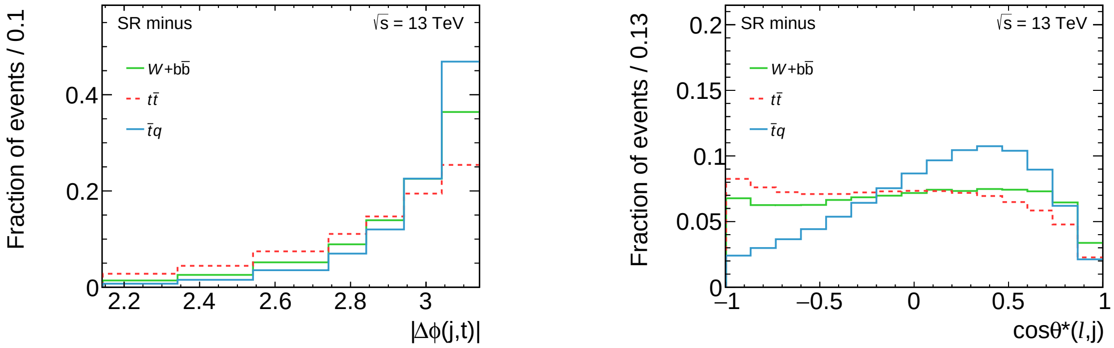

(a) $|\Delta\phi(j,t)|$ (b) $\cos\theta^*(\ell,j)$

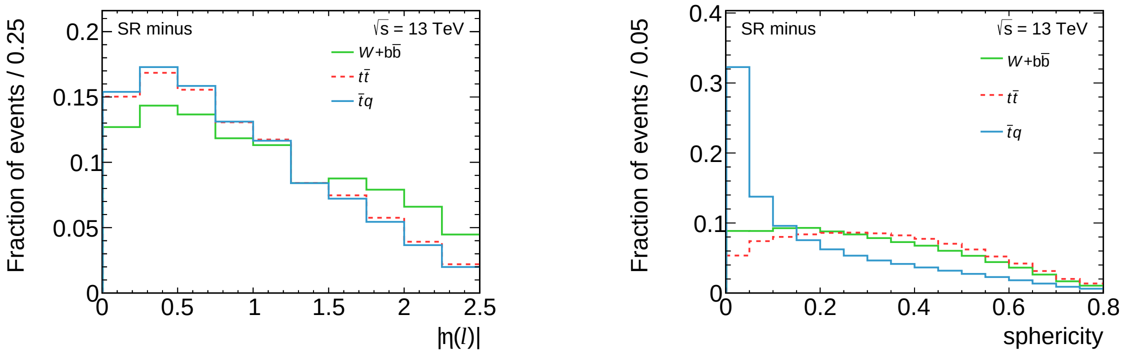

(c) $|\eta(\ell)|$ (d) sphericity

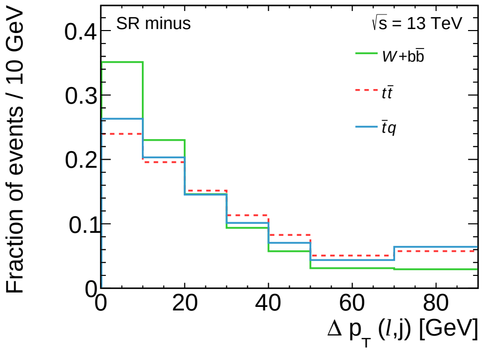

(e) $|\Delta p_{\mathrm{T}}(\ell,j)|$

Figure A.3.: Shapes of the last five neural network input variable distributions for the signal process and the main background processes in the SR `minus`.

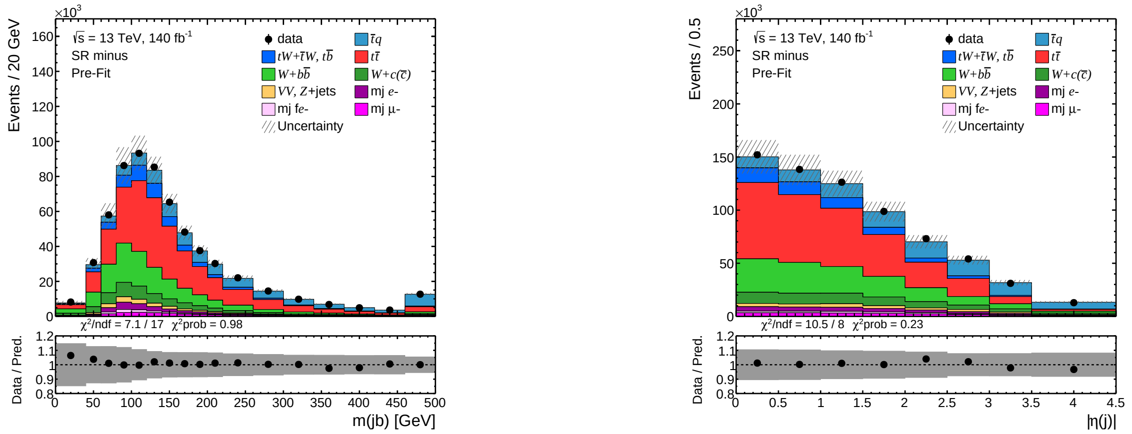

(a) m(jb) (b) $|\eta(j)|$

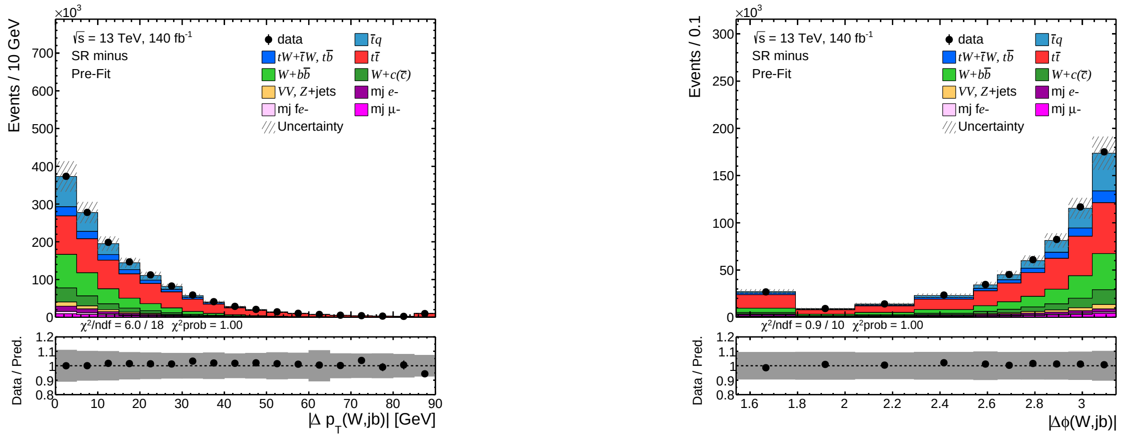

(c) $|\Delta p_{\mathrm{T}}(W, jb)|$ (d) $|\Delta\phi(W, jb)|$

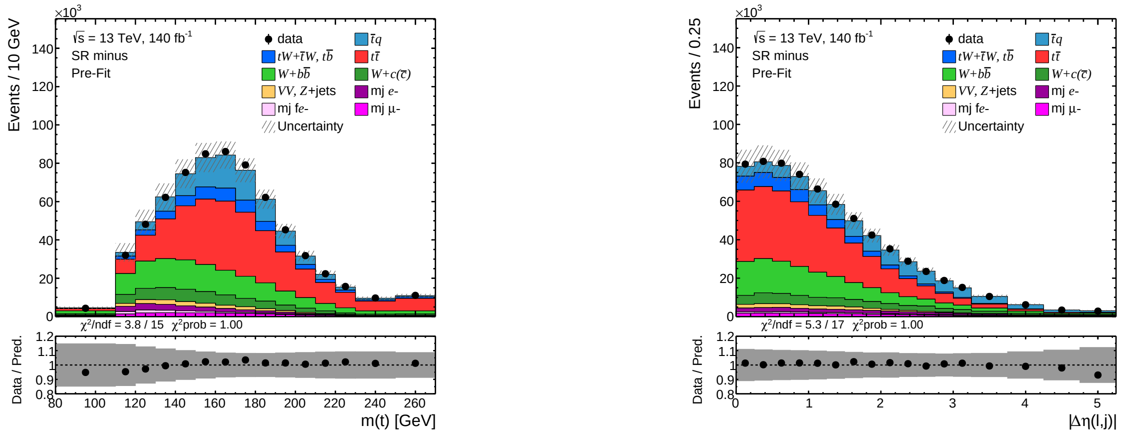

(e) $m(t)$ (f) $|\Delta\eta(\ell, j)|$

Figure A.4.: Distributions of the first six input variables of the neural network, comparing data and simulation in the SR `minus`.

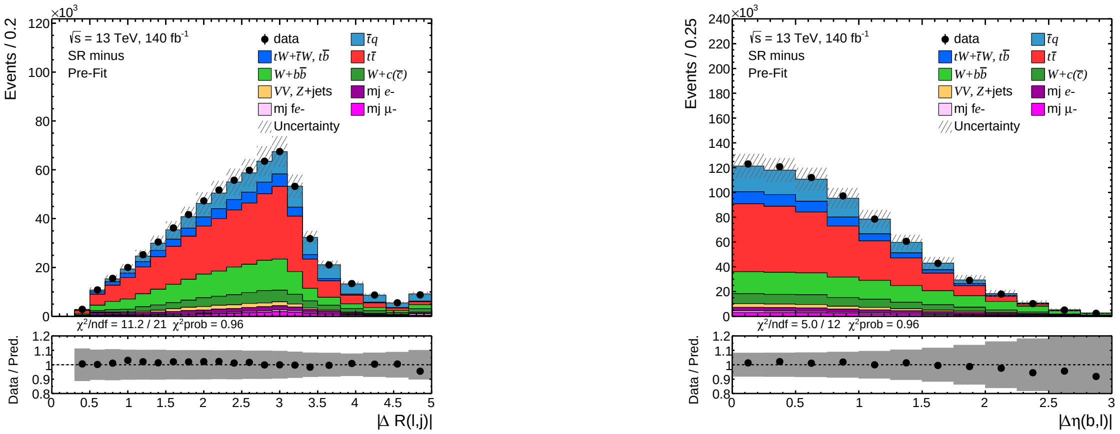

(a) $\Delta R(\ell, j)$ (b) $|\Delta\eta(b, \ell)|$

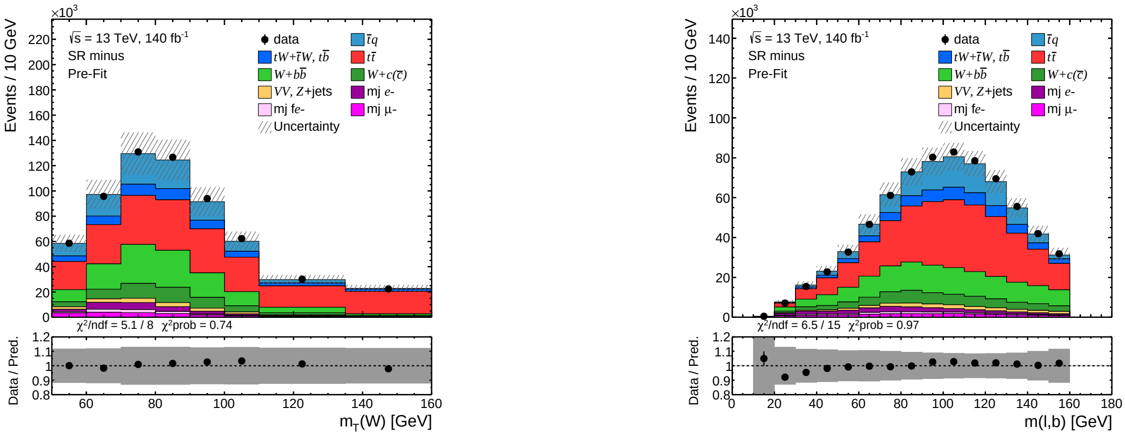

(c) $m_{\mathrm{T}}(W)$ (d) $m(\ell b)$

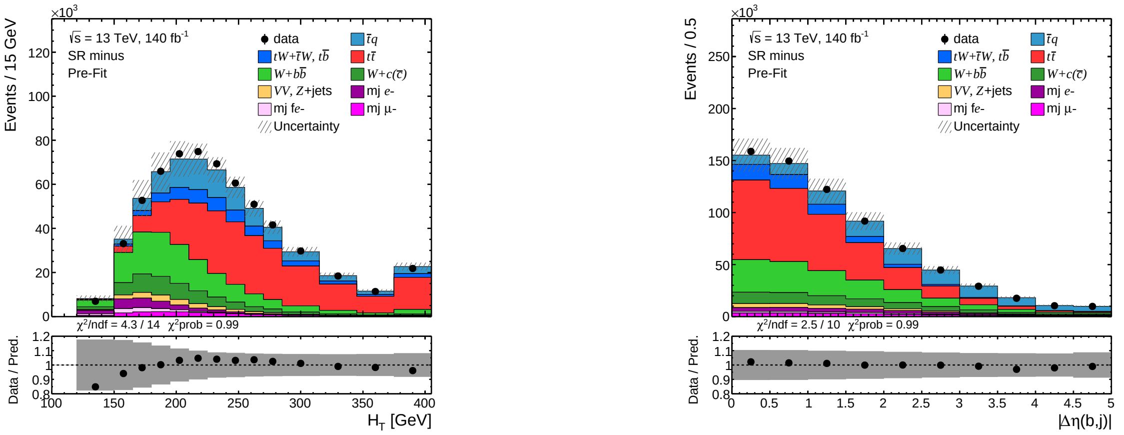

(e) H_{T} (f) $|\Delta\eta(b, j)|$

Figure A.5.: Distributions of the seventh to twelfth input variable of the neural network, comparing data and simulation in the SR `minus`.

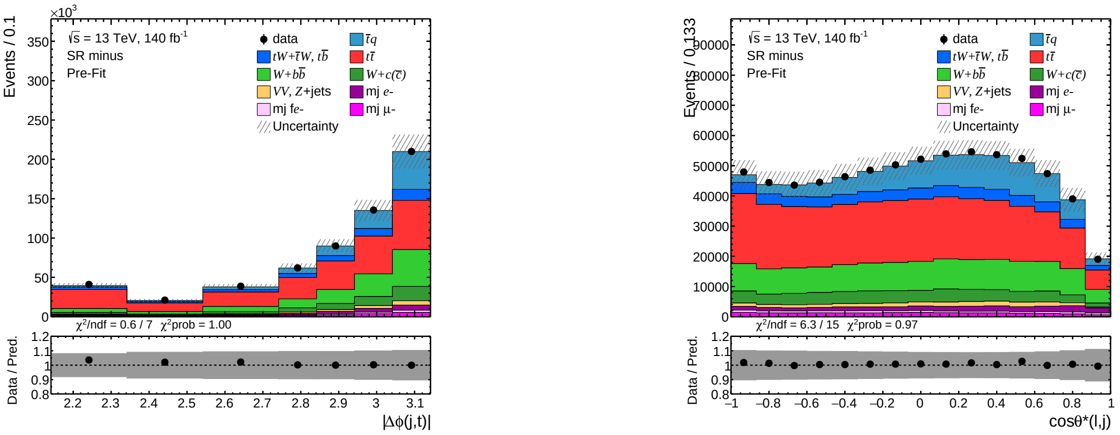

(a) $|\Delta\phi(j,t)|$

(b) $\cos\theta^*(\ell,j)$

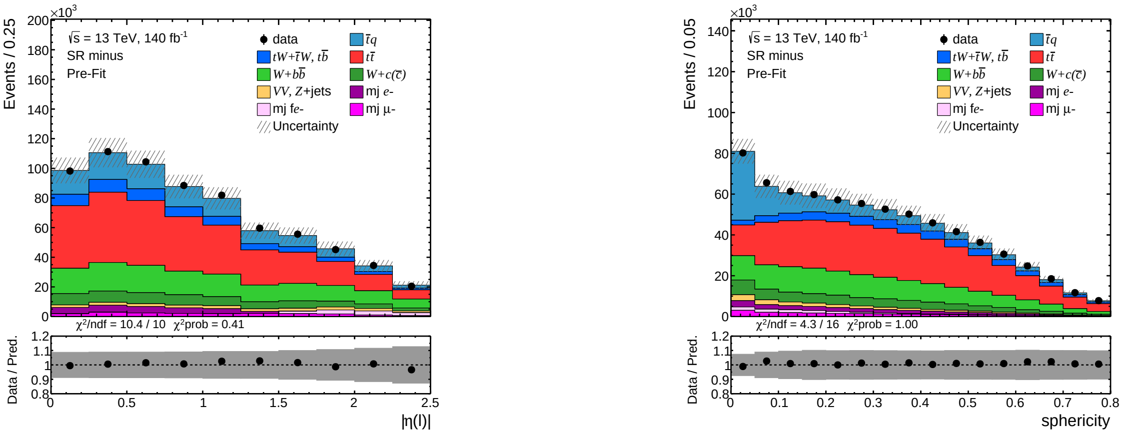

(c) $|\eta(\ell)|$

(d) sphericity

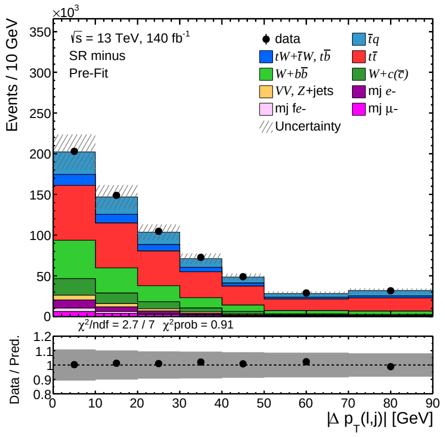

(e) $|\Delta p_{\mathrm{T}}(\ell,j)|$

Figure A.6.: Distributions of the last five input variable of the neural network, comparing data and simulation in the SR `minus`.

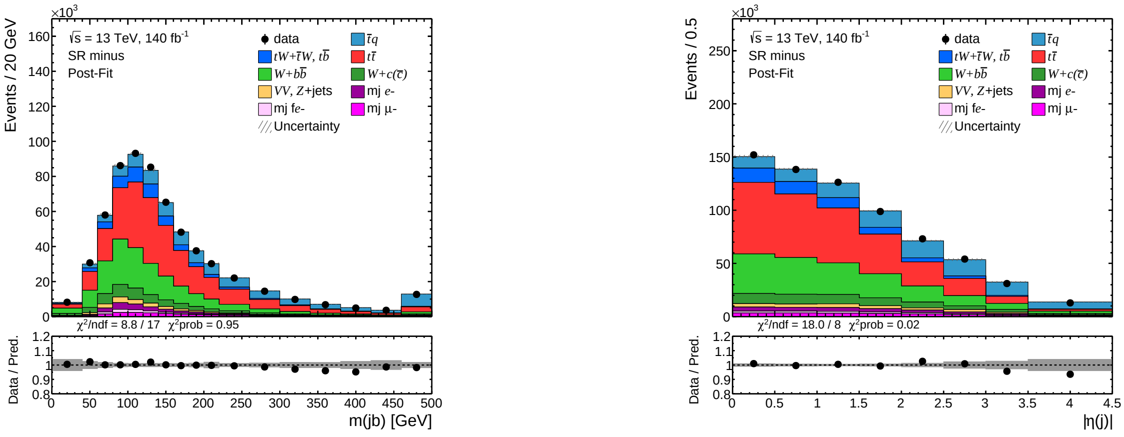

(a) $\mathrm{m}(jb)$

(b) $|\eta(j)|$

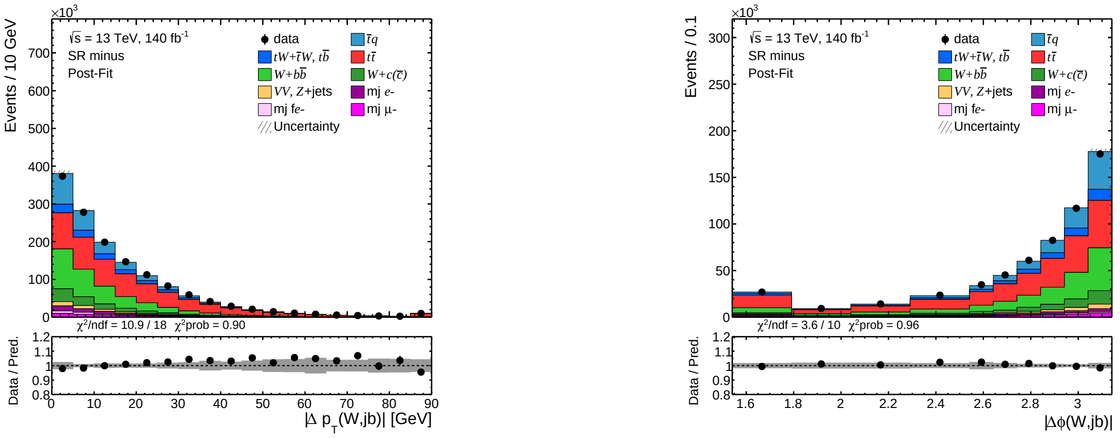

(c) $|\Delta p_{\mathrm{T}}(W, jb)|$

(d) $|\Delta\phi(W, jb)|$

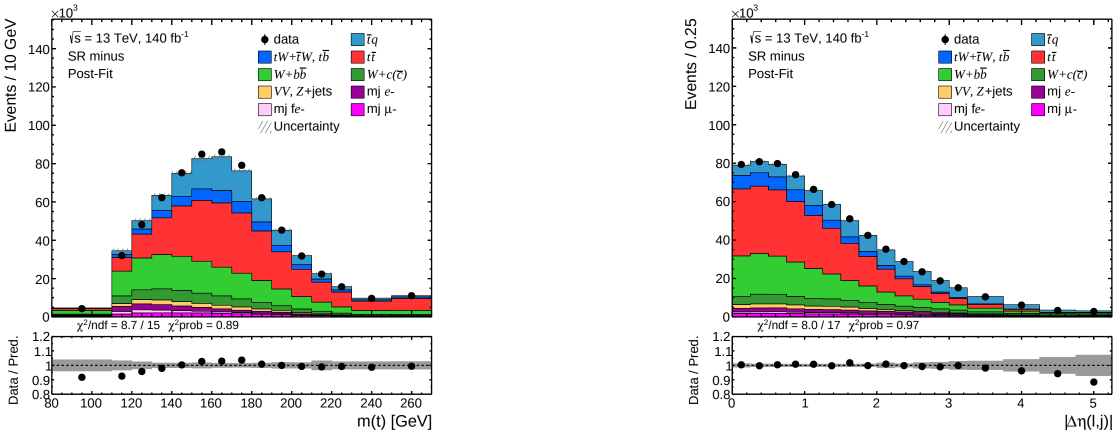

(e) $m(t)$

(f) $|\Delta\eta(\ell, j)|$

Figure A.7.: Distributions of the first six input variables of the neural network, comparing data and simulation in the SR `minus`. All nuisance and signal parameters are set to their ML estimators.

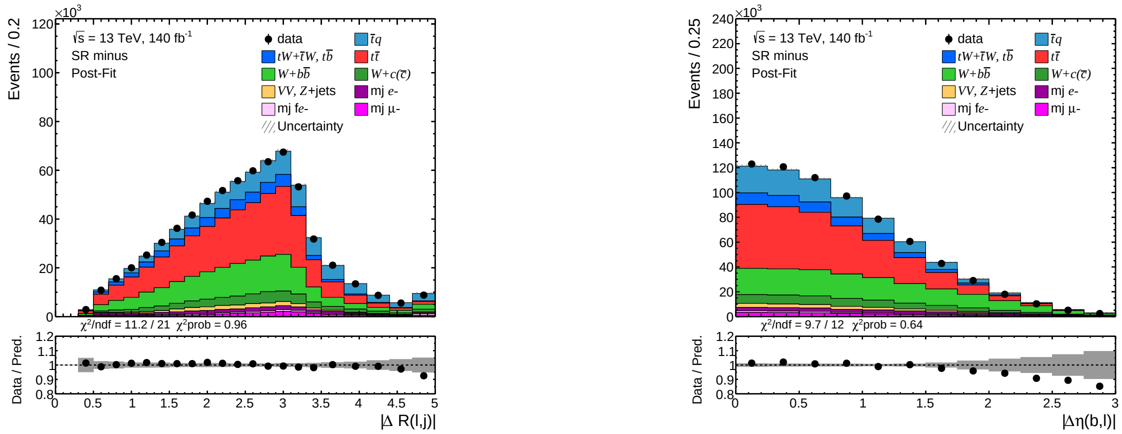

(a) $\Delta R(\ell, j)$ (b) $|\Delta\eta(b, \ell)|$

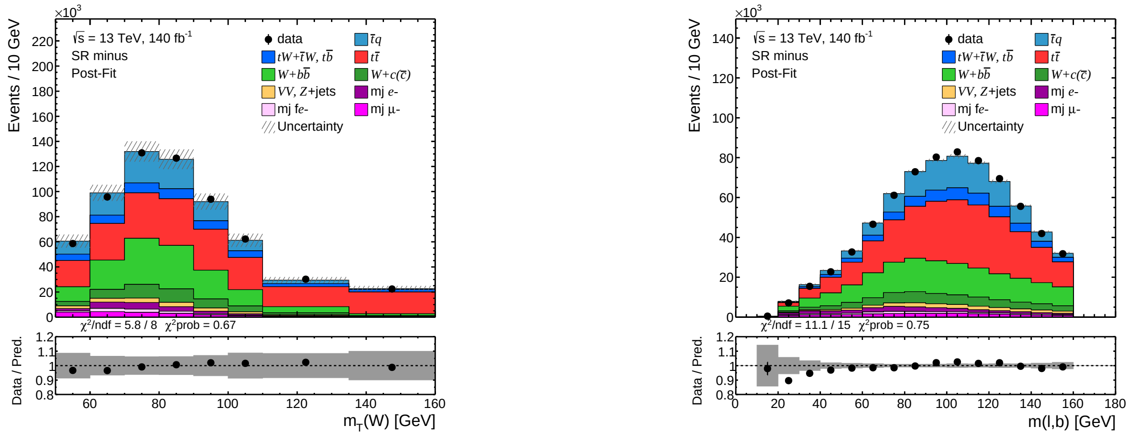

(c) $m_{\mathrm{T}}(W)$ (d) $m(\ell b)$

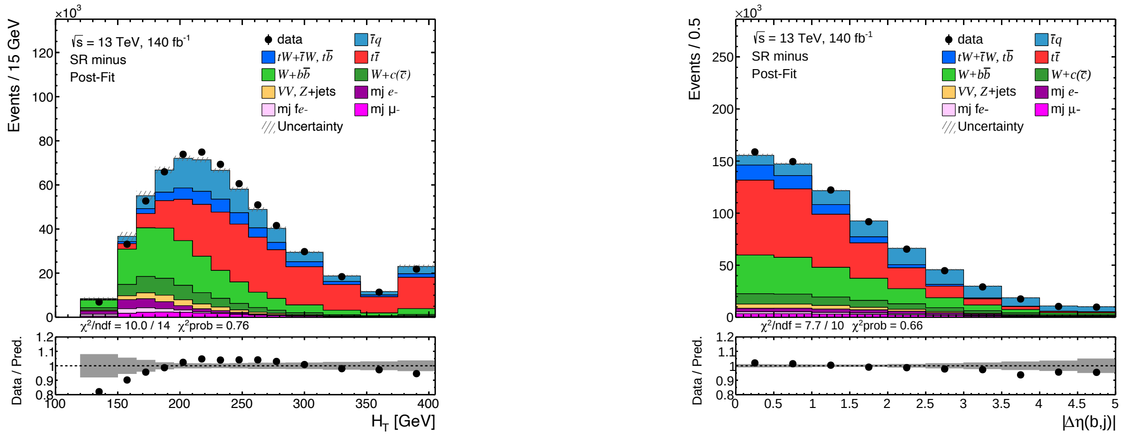

(e) H_{T} (f) $|\Delta\eta(b, j)|$

Figure A.8.: Distributions of the seventh to twelfth input variable of the neural network, comparing data and simulation in the SR `minus`. All nuisance and signal parameters are set to their ML estimators.

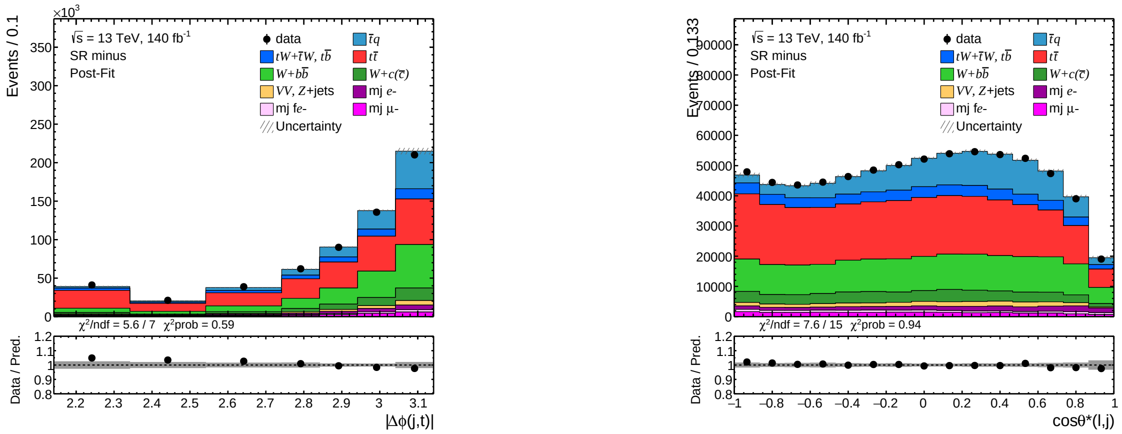

(a) $|\Delta\phi(j,t)|$ (b) $\cos\theta^*(\ell,j)$

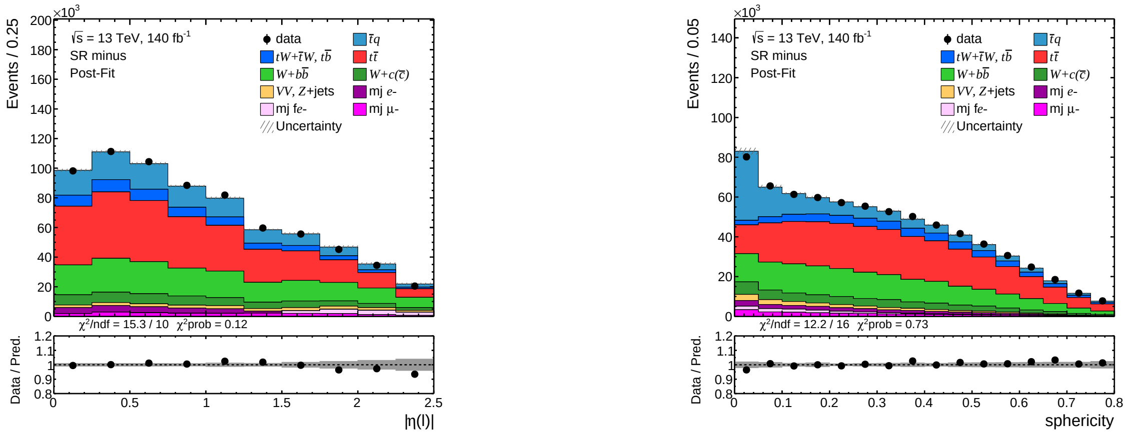

(c) $|\eta(\ell)|$ (d) sphericity

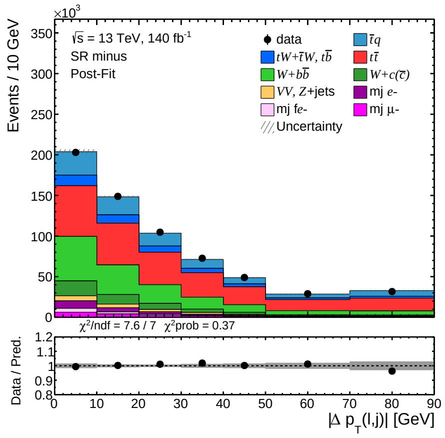

(e) $|\Delta p_{\mathrm{T}}(\ell,j)|$

Figure A.9.: Distributions of the last five input variable of the neural network, comparing data and simulation in the SR `minus`. All nuisance and signal parameters are set to their ML estimators.

Bibliography

[1] S. L. Glashow. “Partial Symmetries of Weak Interactions.” In: *Nucl. Phys.* 22 (1961), pp. 579–588. DOI: `10.1016/0029-5582(61)90469-2`.

[2] S. Weinberg. “A Model of Leptons.” In: *Phys. Rev. Lett.* 19 (1967), pp. 1264–1266. DOI: `10.1103/PhysRevLett.19.1264`.

[3] A. Salam. “Weak and Electromagnetic Interactions.” In: *Conf. Proc. C* 680519 (1968), pp. 367–377. DOI: `10.1142/9789812795915_0034`.

[4] M. Y. Han and Y. Nambu. “Three Triplet Model with Double SU(3) Symmetry.” In: *Phys. Rev.* 139 (1965). Ed. by T. Eguchi, B1006–B1010. DOI: `10.1103/PhysRev.139.B1006`.

[5] M. Gell-Mann. “A Schematic Model of Baryons and Mesons.” In: *Phys. Lett.* 8 (1964), pp. 214–215. DOI: `10.1016/S0031-9163(64)92001-3`.

[6] D. Griffiths. *Introduction to elementary particles*. 2008. ISBN: 978-3-527-40601-2.

[7] S. Pokorski. *GAUGE FIELD THEORIES*. Cambridge University Press, Jan. 2005. ISBN: 978-0-511-03780-1, 978-0-521-47816-8.

[8] M. E. Peskin and D. V. Schroeder. *An Introduction to quantum field theory*. Reading, USA: Addison-Wesley, 1995. ISBN: 978-0-201-50397-5.

[9] Wikipedia contributors. *Standard Model of Elementary Particles — Wikipedia, The Free Encyclopedia*. [Online; accessed 27-11-2023]. 2023.

[10] E. Noether. “Invariante Variationsprobleme.” ger. In: *Nachrichten von der Gesellschaft der Wissenschaften zu Göttingen, Mathematisch-Physikalische Klasse* 1918 (1918), pp. 235–257.

[11] P. A. M. Dirac. “The quantum theory of the electron.” In: *Proc. Roy. Soc. Lond. A* 117 (1928), pp. 610–624. DOI: `10.1098/rspa.1928.0023`.

[12] N. Cabibbo. “Unitary Symmetry and Leptonic Decays.” In: *Phys. Rev. Lett.* 10 (1963), pp. 531–533. DOI: `10.1103/PhysRevLett.10.531`.

[13] M. Kobayashi and T. Maskawa. “CP Violation in the Renormalizable Theory of Weak Interaction.” In: *Prog. Theor. Phys.* 49 (1973), pp. 652–657. DOI: `10.1143/PTP.49.652`.

[14] R. L. Workman et al. "Review of Particle Physics." In: *PTEP* 2022 (2022), p. 083C01. DOI: `10.1093/ptep/ptac097`.

[15] A. Einstein. "The foundation of the general theory of relativity." In: *Annalen Phys.* 49.7 (1916). Ed. by J.-P. Hsu and D. Fine, pp. 769–822. DOI: `10.1002/andp.19163540702`.

[16] E. Anderson. "The Problem of Time in Quantum Gravity." In: (Sept. 2010). arXiv: `1009.2157 [gr-qc]`.

[17] P. Zyla et al. "Review of Particle Physics." In: *PTEP* 2020.8 (2020). and 2021 update, p. 083C01. DOI: `10.1093/ptep/ptaa104`.

[18] S. Weinberg. "A Model of Leptons." In: *Phys. Rev. Lett.* 19 (21 Nov. 1967), pp. 1264–1266. DOI: `10.1103/PhysRevLett.19.1264`.

[19] G. Arnison et al. "Experimental Observation of Isolated Large Transverse Energy Electrons with Associated Missing Energy at $\sqrt{s} = 540$ GeV." In: *Phys. Lett. B* 122 (1983), pp. 103–116. DOI: `10.1016/0370-2693(83)91177-2`.

[20] M. Banner et al. "Observation of Single Isolated Electrons of High Transverse Momentum in Events with Missing Transverse Energy at the CERN anti-p p Collider." In: *Phys. Lett. B* 122 (1983), pp. 476–485. DOI: `10.1016/0370-2693(83)91605-2`.

[21] S. W. Herb et al. "Observation of a Dimuon Resonance at 9.5-GeV in 400-GeV Proton-Nucleus Collisions." In: *Phys. Rev. Lett.* 39 (1977), pp. 252–255. DOI: `10.1103/PhysRevLett.39.252`.

[22] S. Abachi et al. "Observation of the top quark." In: *Phys. Rev. Lett.* 74 (1995), pp. 2632–2637. DOI: `10.1103/PhysRevLett.74.2632`. arXiv: `hep-ex/9503003`.

[23] F. Abe et al. "Observation of top quark production in $\bar{p}p$ collisions." In: *Phys. Rev. Lett.* 74 (1995), pp. 2626–2631. DOI: `10.1103/PhysRevLett.74.2626`. arXiv: `hep-ex/9503002`.

[24] F. Englert and R. Brout. "Broken Symmetry and the Mass of Gauge Vector Mesons." In: *Phys. Rev. Lett.* 13 (1964). Ed. by J. C. Taylor, pp. 321–323. DOI: `10.1103/PhysRevLett.13.321`.

[25] P. W. Higgs. "Broken Symmetries and the Masses of Gauge Bosons." In: *Phys. Rev. Lett.* 13 (1964). Ed. by J. C. Taylor, pp. 508–509. DOI: `10.1103/PhysRevLett.13.508`.

[26] G. S. Guralnik, C. R. Hagen, and T. W. B. Kibble. "Global Conservation Laws and Massless Particles." In: *Phys. Rev. Lett.* 13 (1964). Ed. by J. C. Taylor, pp. 585–587. DOI: `10.1103/PhysRevLett.13.585`.

[27] G. Aad et al. "Observation of a new particle in the search for the Standard Model Higgs boson with the ATLAS detector at the LHC." In: *Phys. Lett. B* 716 (2012), pp. 1–29. DOI: `10.1016/j.physletb.2012.08.020`. arXiv: `1207.7214 [hep-ex]`.

[28] S. Chatrchyan et al. "Observation of a New Boson at a Mass of 125 GeV with the CMS Experiment at the LHC." In: *Phys. Lett. B* 716 (2012), pp. 30–61. DOI: `10.1016/j.physletb.2012.08.021`. arXiv: `1207.7235 [hep-ex]`.

[29] LHCTopWG. *LHCTopWG Summary Plots*. [Online; accessed 22-12-2023]. 2023.

[30] DO Collaboration, V. Abazov et al. "Model-independent measurement of t-channel single top quark production in $p\bar{p}$ collisions at $\sqrt{s} = 1.96$ TeV." In: *Phys. Lett. B* 705 (2011), pp. 313–319. DOI: `10.1016/j.physletb.2011.10.035`. arXiv: `1105.2788 [hep-ex]`.

[31] T. Aaltonen et al. "Observation of Single Top Quark Production and Measurement of |Vtb| with CDF." In: *Phys. Rev.* D82 (2010), p. 112005. DOI: `10.1103/PhysRevD.82.112005`. arXiv: `1004.1181`.

[32] G. Aad et al. "Measurement of t-channel single-top-quark production in pp collisions at $\sqrt{s} = 5.02$ TeV with the ATLAS detector." In: (Oct. 2023). arXiv: `2310.01518 [hep-ex]`.

[33] G. Aad et al. "Comprehensive measurements of t-channel single top-quark production cross sections at $\sqrt{s} = 7$ TeV with the ATLAS detector." In: *Phys. Rev. D* 90.11 (2014), p. 112006. DOI: `10.1103/PhysRevD.90.112006`. arXiv: `1406.7844 [hep-ex]`.

[34] S. Chatrchyan et al. "Measurement of the Single-Top-Quark t-Channel Cross Section in pp Collisions at $\sqrt{s} = 7$ TeV." In: *JHEP* 12 (2012), p. 035. DOI: `10.1007/JHEP12(2012)035`. arXiv: `1209.4533 [hep-ex]`.

[35] M. Aaboud et al. "Fiducial, total and differential cross-section measurements of t-channel single top-quark production in pp collisions at 8 TeV using data collected by the ATLAS detector." In: *Eur. Phys. J. C* 77.8 (2017), p. 531. DOI: `10.1140/epjc/s10052-017-5061-9`. arXiv: `1702.02859 [hep-ex]`.

[36] V. Khachatryan et al. "Measurement of the t-channel single-top-quark production cross section and of the $\mid V_{tb} \mid$ CKM matrix element in pp collisions at $\sqrt{s}$= 8 TeV." In: *JHEP* 06 (2014), p. 090. DOI: `10.1007/JHEP06(2014)090`. arXiv: `1403.7366 [hep-ex]`.

[37] M. Aaboud, G. Aad, B. Abbott, J. Abdallah, O. Abdinov, B. Abeloos, R. Aben, O. S. AbouZeid, N. L. Abraham, and et al. "Measurement of the inclusive cross-sections of single top-quark and top-antiquark t-channel production in pp collisions at $\sqrt{s} = 13$ TeV with the ATLAS detector." In: *Journal of High Energy Physics* 2017.4 (Apr. 2017). ISSN: 1029-8479. DOI: `10.1007/jhep04(2017)086`.

[38] A. Sirunyan, A. Tumasyan, W. Adam, F. Ambrogi, E. Asilar, T. Bergauer, J. Brandstetter, M. Dragicevic, J. Erö, A. Escalante Del Valle, and et al. "Measurement of the single top quark and antiquark production cross sections in the t channel and their ratio in proton-proton collisions at s=13TeV." In: *Physics Letters B* 800 (Jan. 2020), p. 135042. ISSN: 0370-2693. DOI: `10.1016/j.physletb.2019.135042`.

[39] R. D. Ball et al. "Parton distributions from high-precision collider data." In: *Eur. Phys. J. C* 77.10 (2017), p. 663. DOI: `10.1140/epjc/s10052-017-5199-5`. arXiv: `1706.00428 [hep-ph]`.

[40] T. Sjöstrand, S. Ask, J. R. Christiansen, R. Corke, N. Desai, P. Ilten, S. Mrenna, S. Prestel, C. O. Rasmussen, and P. Z. Skands. "An Introduction to PYTHIA 8.2." In: *Comput. Phys. Commun.* 191 (2015), pp. 159–177. DOI: `10.1016/j.cpc.2015.01.024`. arXiv: `1410.3012 [hep-ph]`.

[41] S. Höche, F. Krauss, M. Schönherr, and F. Siegert. "A critical appraisal of NLO+PS matching methods." In: *JHEP* 09 (2012), p. 049. DOI: `10.1007/JHEP09(2012)049`. arXiv: `1111.1220 [hep-ph]`.

[42] D. Amati and G. Veneziano. "Preconfinement as a Property of Perturbative QCD." In: *Phys. Lett. B* 83 (1979), pp. 87–92. DOI: `10.1016/0370-2693(79)90896-7`.

[43] D. J. Lange. "The EvtGen particle decay simulation package." In: *Nucl. Instrum. Meth. A* 462 (2001), p. 152. DOI: `10.1016/S0168-9002(01)00089-4`.

[44] M. Beckingham, M. Duehrssen, E. Schmidt, M. Shapiro, M. Venturi, J. Virzi, I. Vivarelli, M. Werner, S. Yamamoto, and T. Yamanaka. "The simulation principle and performance of the ATLAS fast calorimeter simulation FastCaloSim." In: (Oct. 2010).

[45] R. Brun, F. Bruyant, F. Carminati, S. Giani, M. Maire, A. McPherson, G. Patrick, and L. Urban. "GEANT Detector Description and Simulation Tool." In: (Oct. 1994). DOI: `10.17181/CERN.MUHF.DMJ1`.

[46] W. Bernreuther. "Top quark physics at the LHC." In: *J. Phys. G* 35 (2008), p. 083001. DOI: `10.1088/0954-3899/35/8/083001`. arXiv: `0805.1333 [hep-ph]`.

[47] C. F. Uhlemann and N. Kauer. "Narrow-width approximation accuracy." In: *Nucl. Phys. B* 814 (2009), pp. 195–211. DOI: `10.1016/j.nuclphysb.2009.01.022`. arXiv: `0807.4112 [hep-ph]`.

[48] M. Beneke et al. "Top quark physics." In: *Workshop on Standard Model Physics (and more) at the LHC (First Plenary Meeting)*. Mar. 2000, pp. 419–529. DOI: `10.5170/CERN-2000-004.419`. arXiv: `hep-ph/0003033`.

[49] A. Heinson, A. S. Belyaev, and E. E. Boos. "Single top quarks at the Fermilab Tevatron." In: *Phys. Rev. D* 56 (1997), pp. 3114–3128. DOI: `10.1103/PhysRevD.56.3114`. arXiv: `hep-ph/9612424`.

[50] "LHC Machine." In: *JINST* 3 (2008). Ed. by L. Evans and P. Bryant, S08001. DOI: `10.1088/1748-0221/3/08/S08001`.

[51] F. C. G. D. s. Marcastel. "CERN's Accelerator Complex." 2013.

[52] G. Aad et al. "The ATLAS Experiment at the CERN Large Hadron Collider." In: *JINST* 3 (2008), S08003. DOI: `10.1088/1748-0221/3/08/S08003`.

[53] T. C. Collaboration, S. Chatrchyan, G. Hmayakyan, V. Khachatryan, A. M. Sirunyan, W. Adam, T. Bauer, T. Bergauer, H. Bergauer, M. Dragicevic, J. Erö, M. Friedl, R. Frühwirth, V. M. Ghete, P. Glaser, C. Hartl, N. Hoermann, J. Hrubec, S. Hänsel, M. Jeitler, K. Kastner, M. Krammer, I. M. de Abril, M. Markytan, I. Mikulec, and B. Neuherz. "The CMS experiment at the CERN LHC." In: *Journal of Instrumentation* 3.08 (Aug. 2008), S08004. DOI: `10.1088/1748-0221/3/08/S08004`.

[54] T. L. Collaboration, A. A. A. Jr, L. M. A. Filho, A. F. Barbosa, I. Bediaga, G. Cernicchiaro, G. Guerrer, H. P. L. Jr, A. A. Machado, J. Magnin, F. Marujo, J. M. de Miranda, A. Reis, A. Santos, A. Toledo, K. Akiba, S. Amato, B. de Paula, L. de Paula, T. da Silva, M. Gandelman, J. H. Lopes, B. Maréchal, D. Moraes, and E. Polycarpo. "The LHCb Detector at the LHC." In: *Journal of Instrumentation* 3.08 (Aug. 2008), S08005. DOI: `10.1088/1748-0221/3/08/S08005`.

[55] T. A. Collaboration, K. Aamodt, A. A. Quintana, R. Achenbach, S. Acounis, D. Adamová, C. Adler, M. Aggarwal, F. Agnese, G. A. Rinella, Z. Ahammed, A. Ahmad, N. Ahmad, S. Ahmad, A. Akindinov, P. Akishin, D. Aleksandrov, B. Alessandro, R. Alfaro, G. Alfarone, A. Alici, J. Alme, T. Alt, S. Altinpinar, W. Amend, and C. Andrei. "The ALICE experiment at the CERN LHC." In: *Journal of Instrumentation* 3.08 (Aug. 2008), S08002. DOI: `10.1088/1748-0221/3/08/S08002`.

[56] M. Aleksa et al. "Measurement of the ATLAS solenoid magnetic field." In: *JINST* 3 (2008), P04003. DOI: `10.1088/1748-0221/3/04/P04003`.

[57] F. Miano. "The design and performance of the ATLAS Inner Detector trigger for Run 2 LHC collisions at $\sqrt{s} = 13$ TeV." In: *PoS* ICHEP2016 (2016), p. 856. DOI: `10.22323/1.282.0856`.

[58] Y. Takubo. "ATLAS IBL operational experience." In: *PoS* Vertex2016 (2017), p. 004. DOI: `10.22323/1.287.0004`.

[59] A. Abdesselam et al. "The barrel modules of the ATLAS semiconductor tracker." In: *Nucl. Instrum. Meth. A* 568 (2006), pp. 642–671. DOI: `10.1016/j.nima.2006.08.036`.

[60] A. Abdesselam et al. "The ATLAS semiconductor tracker end-cap module." In: *Nucl. Instrum. Meth. A* 575 (2007), pp. 353–389. DOI: `10.1016/j.nima.2007.02.019`.

[61] G. Aad et al. "Operation and performance of the ATLAS semiconductor tracker." In: *JINST* 9 (2014), P08009. DOI: `10.1088/1748-0221/9/08/P08009`. arXiv: `1404.7473 [hep-ex]`.

[62] G. Aad et al. "Alignment of the ATLAS Inner Detector in Run-2." In: *Eur. Phys. J. C* 80.12 (2020), p. 1194. DOI: `10.1140/epjc/s10052-020-08700-6`. arXiv: `2007.07624 [hep-ex]`.

[63] G. Aad et al. "Operation of the ATLAS trigger system in Run 2." In: *JINST* 15.10 (2020), P10004. DOI: `10.1088/1748-0221/15/10/P10004`. arXiv: `2007.12539 [physics.ins-det]`.

[64] G. Aad et al. "Luminosity determination in pp collisions at $\sqrt{s} = 13$ TeV using the ATLAS detector at the LHC." In: *Eur. Phys. J. C* 83.10 (2023), p. 982. DOI: `10.1140/epjc/s10052-023-11747-w`. arXiv: `2212.09379 [hep-ex]`.

[65] ATLAS. *Public ATLAS Plots*. [Online; accessed 11-12-2023]. 2023.

[66] G. Aad et al. "ATLAS data quality operations and performance for 2015–2018 data-taking." In: *JINST* 15.04 (2020), P04003. DOI: `10.1088/1748-0221/15/04/P04003`. arXiv: `1911.04632 [physics.ins-det]`.

[67] P. Nason. "A new method for combining NLO QCD with shower Monte Carlo algorithms." In: *JHEP* 11 (2004), p. 040. DOI: `10.1088/1126-6708/2004/11/040`. arXiv: `hep-ph/0409146`.

[68] S. Frixione, G. Ridolfi, and P. Nason. "A positive-weight next-to-leading-order Monte Carlo for heavy flavour hadroproduction." In: *JHEP* 09 (2007), p. 126. DOI: `10.1088/1126-6708/2007/09/126`. arXiv: `0707.3088 [hep-ph]`.

[69] S. Frixione, P. Nason, and C. Oleari. "Matching NLO QCD computations with parton shower simulations: the POWHEG method." In: *JHEP* 11 (2007), p. 070. DOI: `10.1088/1126-6708/2007/11/070`. arXiv: `0709.2092 [hep-ph]`.

[70] S. Alioli, P. Nason, C. Oleari, and E. Re. "NLO single-top production matched with shower in POWHEG: s- and t-channel contributions." In: *JHEP* 09 (2009), p. 111. DOI: `10.1088/1126-6708/2009/09/111`. arXiv: `0907.4076 [hep-ph]`.

[71] S. Alioli, P. Nason, C. Oleari, and E. Re. "A general framework for implementing NLO calculations in shower Monte Carlo programs: the POWHEG BOX." In: *JHEP* 06 (2010), p. 043. DOI: `10.1007/JHEP06(2010)043`. arXiv: `1002.2581 [hep-ph]`.

[72] E. Re. "Single-top Wt-channel production matched with parton showers using the POWHEG method." In: *Eur. Phys. J. C* 71 (2011), p. 1547. DOI: `10.1140/epjc/s10052-011-1547-z`. arXiv: `1009.2450 [hep-ph]`.

[73] R. Frederix, E. Re, and P. Torrielli. "Single-top t-channel hadroproduction in the four-flavour scheme with POWHEG and aMC@NLO." In: *JHEP* 09 (2012), p. 130. DOI: `10.1007/JHEP09(2012)130`. arXiv: `1207.5391 [hep-ph]`.

[74] R. D. Ball et al. "Parton distributions for the LHC Run II." In: *JHEP* 04 (2015), p. 040. DOI: `10.1007/JHEP04(2015)040`. arXiv: `1410.8849 [hep-ph]`.

[75] T. Sjostrand, S. Mrenna, and P. Z. Skands. "A Brief Introduction to PYTHIA 8.1." In: *Comput. Phys. Commun.* 178 (2008), pp. 852–867. DOI: `10.1016/j.cpc.2008.01.036`. arXiv: `0710.3820 [hep-ph]`.

[76] ATLAS Collaboration. *ATLAS Pythia 8 tunes to 7 TeV data*. ATL-PHYS-PUB-2014-021. 2014.

[77] R. D. Ball, V. Bertone, S. Carrazza, C. S. Deans, L. Del Debbio, et al. "Parton distributions with LHC data." In: *Nucl. Phys. B* 867 (2013), pp. 244–289. DOI: `10.1016/j.nuclphysb.2012.10.003`. arXiv: `1207.1303 [hep-ph]`.

[78] J. Campbell, T. Neumann, and Z. Sullivan. "Single-top-quark production in the t-channel at NNLO." In: *JHEP* 02 (2021), p. 040. DOI: `10.1007/JHEP02(2021)040`. arXiv: `2012.01574 [hep-ph]`.

[79] S. Frixione, E. Laenen, P. Motylinski, and B. R. Webber. "Angular correlations of lepton pairs from vector boson and top quark decays in Monte Carlo simulations." In: *JHEP* 0704 (2007), p. 081. DOI: `10.1088/1126-6708/2007/04/081`. arXiv: `hep-ph/0702198`.

[80] P. Artoisenet, R. Frederix, O. Mattelaer, and R. Rietkerk. “Automatic spin-entangled decays of heavy resonances in Monte Carlo simulations.” In: *JHEP* 1303 (2013), p. 015. DOI: `10.1007/JHEP03(2013)015`. arXiv: `1212.3460 [hep-ph]`.

[81] S. Agostinelli et al. “GEANT4–a simulation toolkit.” In: *Nucl. Instrum. Meth. A* 506 (2003), pp. 250–303. DOI: `10.1016/S0168-9002(03)01368-8`.

[82] S. Frixione, E. Laenen, P. Motylinski, B. R. Webber, and C. D. White. “Single-top hadroproduction in association with a W boson.” In: *JHEP* 0807 (2008), p. 029. DOI: `10.1088/1126-6708/2008/07/029`. arXiv: `0805.3067 [hep-ph]`.

[83] ATLAS Collaboration. *Studies on top-quark Monte Carlo modelling for Top2016*. ATL-PHYS-PUB-2016-020. 2016.

[84] N. Kidonakis and N. Yamanaka. “Higher-order corrections for tW production at high-energy hadron colliders.” In: *JHEP* 05 (2021), p. 278. DOI: `10.1007/JHEP05(2021)278`. arXiv: `2102.11300 [hep-ph]`.

[85] The NNPDF Collaboration, R. D. Ball, et al. “Parton distributions for the LHC run II.” In: *JHEP* 04 (2015), p. 040. DOI: `10.1007/JHEP04(2015)040`. arXiv: `1410.8849 [hep-ph]`.

[86] M. Aliev, H. Lacker, U. Langenfeld, S. Moch, P. Uwer, and M. Wiedermann. “HATHOR – HAdronic Top and Heavy quarks crOss section calculatoR.” In: *Comput. Phys. Commun.* 182 (2011), pp. 1034–1046. DOI: `10.1016/j.cpc.2010.12.040`. arXiv: `1007.1327 [hep-ph]`.

[87] P. Kant, O. M. Kind, T. Kintscher, T. Lohse, T. Martini, S. Mölbitz, P. Rieck, and P. Uwer. “HatHor for single top-quark production: Updated predictions and uncertainty estimates for single top-quark production in hadronic collisions.” In: *Comput. Phys. Commun.* 191 (2015), pp. 74–89. DOI: `10.1016/j.cpc.2015.02.001`. arXiv: `1406.4403 [hep-ph]`.

[88] M. Czakon and A. Mitov. “Top++: A program for the calculation of the top-pair cross-section at hadron colliders.” In: *Comput. Phys. Commun.* 185 (2014), p. 2930. DOI: `10.1016/j.cpc.2014.06.021`. arXiv: `1112.5675 [hep-ph]`.

[89] M. Bahr et al. “Herwig++ Physics and Manual.” In: *Eur. Phys. J. C* 58 (2008), pp. 639–707. DOI: `10.1140/epjc/s10052-008-0798-9`. arXiv: `0803.0883 [hep-ph]`.

[90] J. Bellm et al. “Herwig 7.0/Herwig++ 3.0 release note.” In: *Eur. Phys. J. C* 76.4 (2016), p. 196. DOI: `10.1140/epjc/s10052-016-4018-8`. arXiv: `1512.01178 [hep-ph]`.

[91] E. Bothmann et al. "Event generation with Sherpa 2.2." In: *SciPost Phys.* 7.3 (2019), p. 034. DOI: `10.21468/SciPostPhys.7.3.034`. arXiv: `1905.09127 [hep-ph]`.

[92] T. Gleisberg and S. Höche. "Comix, a new matrix element generator." In: *JHEP* 0812 (2008), p. 039. DOI: `10.1088/1126-6708/2008/12/039`. arXiv: `0808.3674 [hep-ph]`.

[93] F. Buccioni, J.-N. Lang, J. M. Lindert, P. Maierhöfer, S. Pozzorini, H. Zhang, and M. F. Zoller. "OpenLoops 2." In: *Eur. Phys. J. C* 79.10 (2019), p. 866. DOI: `10.1140/epjc/s10052-019-7306-2`. arXiv: `1907.13071 [hep-ph]`.

[94] F. Cascioli, P. Maierhofer, and S. Pozzorini. "Scattering Amplitudes with Open Loops." In: *Phys. Rev. Lett.* 108 (2012), p. 111601. DOI: `10.1103/PhysRevLett.108.111601`. arXiv: `1111.5206 [hep-ph]`.

[95] A. Denner, S. Dittmaier, and L. Hofer. "COLLIER: A fortran-based complex one-loop library in extended regularizations." In: *Comput. Phys. Commun.* 212 (2017), pp. 220–238. DOI: `10.1016/j.cpc.2016.10.013`. arXiv: `1604.06792 [hep-ph]`.

[96] S. Schumann and F. Krauss. "A Parton shower algorithm based on Catani-Seymour dipole factorisation." In: *JHEP* 0803 (2008), p. 038. DOI: `10.1088/1126-6708/2008/03/038`. arXiv: `0709.1027 [hep-ph]`.

[97] S. Höche, F. Krauss, M. Schönherr, and F. Siegert. "QCD matrix elements + parton showers. The NLO case." In: *JHEP* 04 (2013), p. 027. DOI: `10.1007/JHEP04(2013)027`. arXiv: `1207.5030 [hep-ph]`.

[98] S. Catani, F. Krauss, B. R. Webber, and R. Kuhn. "QCD Matrix Elements + Parton Showers." In: *JHEP* 11 (2001), p. 063. DOI: `10.1088/1126-6708/2001/11/063`. arXiv: `hep-ph/0109231`.

[99] S. Höche, F. Krauss, S. Schumann, and F. Siegert. "QCD matrix elements and truncated showers." In: *JHEP* 05 (2009), p. 053. DOI: `10.1088/1126-6708/2009/05/053`. arXiv: `0903.1219 [hep-ph]`.

[100] C. Anastasiou, L. J. Dixon, K. Melnikov, and F. Petriello. "High precision QCD at hadron colliders: Electroweak gauge boson rapidity distributions at next-to-next-to leading order." In: *Phys. Rev. D* 69 (2004), p. 094008. DOI: `10.1103/PhysRevD.69.094008`. arXiv: `hep-ph/0312266`.

[101] T. Gleisberg, S. Höche, F. Krauss, M. Schönherr, S. Schumann, F. Siegert, and W. J. "Event generation with SHERPA 1.1." In: *JHEP* 02 (2009), p. 007. DOI: `10.1088/1126-6708/2009/02/007`. arXiv: `0811.4622 [hep-ph]`.

[102] "Estimation of non-prompt and fake lepton backgrounds in final states with top quarks produced in proton-proton collisions at \sqrts=8~TeV with the ATLAS detector." In: (Oct. 2014).

[103] T. Cornelissen, M. Elsing, I. Gavrilenko, W. Liebig, E. Moyse, and A. Salzburger. "The new ATLAS track reconstruction (NEWT)." In: *J. Phys. Conf. Ser.* 119 (2008). Ed. by R. Sobie, R. Tafirout, and J. Thomson, p. 032014. DOI: `10.1088/1742-6596/119/3/032014`.

[104] A. Salzburger. "Optimisation of the ATLAS Track Reconstruction Software for Run-2." In: *J. Phys. Conf. Ser.* 664.7 (2015), p. 072042. DOI: `10.1088/1742-6596/664/7/072042`.

[105] R. Fruhwirth. "Application of Kalman filtering to track and vertex fitting." In: *Nucl. Instrum. Meth. A* 262 (1987), pp. 444–450. DOI: `10.1016/0168-9002(87)90887-4`.

[106] M. Aaboud et al. "Performance of the ATLAS Track Reconstruction Algorithms in Dense Environments in LHC Run 2." In: *Eur. Phys. J. C* 77.10 (2017), p. 673. DOI: `10.1140/epjc/s10052-017-5225-7`. arXiv: `1704.07983 [hep-ex]`.

[107] M. Aaboud et al. "Reconstruction of primary vertices at the ATLAS experiment in Run 1 proton–proton collisions at the LHC." In: *Eur. Phys. J. C* 77.5 (2017), p. 332. DOI: `10.1140/epjc/s10052-017-4887-5`. arXiv: `1611.10235 [physics.ins-det]`.

[108] "Vertex Reconstruction Performance of the ATLAS Detector at $\sqrt{s} = 13\,\mathrm{TeV}$'." In: (2015).

[109] G. Aad et al. "Topological cell clustering in the ATLAS calorimeters and its performance in LHC Run 1." In: *Eur. Phys. J. C* 77 (2017), p. 490. DOI: `10.1140/epjc/s10052-017-5004-5`. arXiv: `1603.02934 [hep-ex]`.

[110] M. Aaboud et al. "Jet reconstruction and performance using particle flow with the ATLAS Detector." In: *Eur. Phys. J. C* 77.7 (2017), p. 466. DOI: `10.1140/epjc/s10052-017-5031-2`. arXiv: `1703.10485 [hep-ex]`.

[111] M. Cacciari, G. P. Salam, and G. Soyez. "The anti-k_t jet clustering algorithm." In: *JHEP* 04 (2008), p. 063. DOI: `10.1088/1126-6708/2008/04/063`. arXiv: `0802.1189 [hep-ph]`.

[112] "Tagging and suppression of pileup jets." In: (May 2014).

[113] ATLAS Collaboration. "Identification and rejection of pile-up jets at high pseudorapidity with the ATLAS detector." In: *Eur. Phys. J. C* 77 (2017), p. 580. DOI: `10.1140/epjc/s10052-017-5081-5`. arXiv: `1705.02211 [hep-ex]`.

[114] G. Aad et al. "Jet energy scale and resolution measured in proton–proton collisions at $\sqrt{s} = 13$ TeV with the ATLAS detector." In: *Eur. Phys. J. C* 81.8 (2021), p. 689. DOI: `10.1140/epjc/s10052-021-09402-3`. arXiv: `2007.02645 [hep-ex]`.

[115] G. Aad et al. "Electron and photon performance measurements with the ATLAS detector using the 2015–2017 LHC proton-proton collision data." In: *JINST* 14.12 (2019), P12006. DOI: `10.1088/1748-0221/14/12/P12006`. arXiv: `1908.00005 [hep-ex]`.

[116] M. Aaboud et al. "Electron and photon energy calibration with the ATLAS detector using 2015–2016 LHC proton-proton collision data." In: *JINST* 14.03 (2019), P03017. DOI: `10.1088/1748-0221/14/03/P03017`. arXiv: `1812.03848 [hep-ex]`.

[117] G. Aad et al. "Electron and photon energy calibration with the ATLAS detector using LHC Run 1 data." In: *Eur. Phys. J. C* 74.10 (2014), p. 3071. DOI: `10.1140/epjc/s10052-014-3071-4`. arXiv: `1407.5063 [hep-ex]`.

[118] M. Aaboud et al. "Electron reconstruction and identification in the ATLAS experiment using the 2015 and 2016 LHC proton-proton collision data at $\sqrt{s}$ = 13 TeV." In: *Eur. Phys. J. C* 79.8 (2019), p. 639. DOI: `10.1140/epjc/s10052-019-7140-6`. arXiv: `1902.04655 [physics.ins-det]`.

[119] M. Aaboud et al. "Evidence for the associated production of the Higgs boson and a top quark pair with the ATLAS detector." In: *Phys. Rev. D* 97.7 (2018), p. 072003. DOI: `10.1103/PhysRevD.97.072003`. arXiv: `1712.08891 [hep-ex]`.

[120] G. Aad et al. "Muon reconstruction and identification efficiency in ATLAS using the full Run 2 pp collision data set at $\sqrt{s} = 13$ TeV." In: *Eur. Phys. J. C* 81.7 (2021), p. 578. DOI: `10.1140/epjc/s10052-021-09233-2`. arXiv: `2012.00578 [hep-ex]`.

[121] G. Aad et al. "Muon reconstruction performance of the ATLAS detector in proton–proton collision data at $\sqrt{s}$ =13 TeV." In: *Eur. Phys. J. C* 76.5 (2016), p. 292. DOI: `10.1140/epjc/s10052-016-4120-y`. arXiv: `1603.05598 [hep-ex]`.

[122] "Optimisation and performance studies of the ATLAS b-tagging algorithms for the 2017-18 LHC run." In: (July 2017).

[123] "Secondary vertex finding for jet flavour identification with the ATLAS detector." In: (June 2017).

[124] "Topological *b*-hadron decay reconstruction and identification of *b*-jets with the JetFitter package in the ATLAS experiment at the LHC." In: (2018).

[125] ATLAS Collaboration. "ATLAS *b*-jet identification performance and efficiency measurement with $t\bar{t}$ events in pp collisions at $\sqrt{s} = 13\,\text{TeV}$." In: *Eur. Phys. J. C* 79 (2019), p. 970. DOI: `10.1140/epjc/s10052-019-7450-8`. arXiv: `1907.05120 [hep-ex]`.

[126] ATLAS Collaboration. *Identification of Jets Containing b-Hadrons with Recurrent Neural Networks at the ATLAS Experiment*. ATL-PHYS-PUB-2017-003. 2017.

[127] M. Aaboud et al. "Performance of missing transverse momentum reconstruction with the ATLAS detector using proton-proton collisions at $\sqrt{s}$ = 13 TeV." In: *Eur. Phys. J. C* 78.11 (2018), p. 903. DOI: `10.1140/epjc/s10052-018-6288-9`. arXiv: `1802.08168 [hep-ex]`.

[128] T. Chwalek. "Messung der W -Boson-Helizitätsanteile in Top-Quark-Zerfällen mit dem CDF II Experiment und Studien zu einer frühen Messung des $t\bar{t}$ -Wirkungsquerschnitts mit dem CMS Experiment." PhD thesis. Karlsruhe U., 2010. DOI: `10.2172/1369264`.

[129] M. Feindt and U. Kerzel. "The NeuroBayes neural network package." In: *Nucl. Instrum. Meth. A* 559 (2006). Ed. by J. Blumlein, W. Friebel, T. Naumann, T. Riemann, P. Wegner, and D. Perret-Gallix, pp. 190–194. DOI: `10.1016/j.nima.2005.11.166`.

[130] M. Feindt. "A Neural Bayesian Estimator for Conditional Probability Densities." In: (Feb. 2004). arXiv: `physics/0402093`.

[131] B. P. Roe, H.-J. Yang, J. Zhu, Y. Liu, I. Stancu, and G. McGregor. "Boosted decision trees, an alternative to artificial neural networks." In: *Nucl. Instrum. Meth. A* 543.2-3 (2005), pp. 577–584. DOI: `10.1016/j.nima.2004.12.018`. arXiv: `physics/0408124`.

[132] B. Richard H., L. Peihuang, N. Jorge, and Z. Ciyou. "A Limited Memory Algorithm for Bound Constrained Optimization." In: *SIAM J. Sci. Comput.* 16.5 (2006), pp. 1190–1208. DOI: `10.1137/0916069`.

[133] G. Aad et al. "ATLAS b-jet identification performance and efficiency measurement with $t\bar{t}$ events in pp collisions at $\sqrt{s} = 13$ TeV." In: *Eur. Phys. J. C* 79.11 (2019), p. 970. DOI: `10.1140/epjc/s10052-019-7450-8`. arXiv: `1907.05120 [hep-ex]`.

[134] G. Aad et al. "Measurement of the c-jet mistagging efficiency in $t\bar{t}$ events using pp collision data at $\sqrt{s} = 13$ TeV collected with the ATLAS detector." In: *Eur. Phys. J. C* 82.1 (2022), p. 95. DOI: `10.1140/epjc/s10052-021-09843-w`. arXiv: `2109.10627 [hep-ex]`.

[135] G. Aad et al. "Calibration of the light-flavour jet mistagging efficiency of the b-tagging algorithms with Z+jets events using 139 fb^{-1} of ATLAS proton–proton collision data at $\sqrt{s} = 13$ TeV." In: *Eur. Phys. J. C* 83.8 (2023), p. 728. DOI: `10.1140/epjc/s10052-023-11736-z`. arXiv: `2301.06319 [hep-ex]`.

[136] M. Aaboud et al. "Performance of the ATLAS Trigger System in 2015." In: *Eur. Phys. J. C* 77.5 (2017), p. 317. DOI: `10.1140/epjc/s10052-017-4852-3`. arXiv: `1611.09661 [hep-ex]`.

[137] G. Aad et al. "Search for flavour-changing neutral-current interactions of a top quark and a gluon in pp collisions at $\sqrt{s} = 13$ TeV with the ATLAS detector." In: *Eur. Phys. J. C* 82.4 (2022), p. 334. DOI: `10.1140/epjc/s10052-022-10182-7`. arXiv: `2112.01302 [hep-ex]`.

[138] J. Butterworth et al. "PDF4LHC recommendations for LHC Run II." In: *J. Phys. G* 43 (2016), p. 023001. DOI: `10.1088/0954-3899/43/2/023001`. arXiv: `1510.03865 [hep-ph]`.

[139] J. O. Berger. "Statistical decision theory and bayesian analysis." In: *Springer Series in Statistics* (1985). DOI: `10.1007/978-1-4757-4286-2`.

[140] G. Cowan. *Statistical data analysis*. 1998. ISBN: 978-0-19-850156-5.

[141] *Proceedings of the 1974 CERN School of Computing: Godøysund, Norway 11 - 24 Aug 1974. 3rd CERN School of Computing*. CERN. Geneva: CERN, 1974. DOI: `10.5170/CERN-1974-023`.

[142] R. D. Cousins. "Generalization of chisquare goodness-of-fit test for binned data using saturated models, with application to histograms." In: (Mar. 2013).

[143] J. Neyman and E. S. Pearson. "On the Problem of the Most Efficient Tests of Statistical Hypotheses." In: *Phil. Trans. Roy. Soc. Lond. A* 231.694-706 (1933), pp. 289–337. DOI: `10.1098/rsta.1933.0009`.

[144] G. L. Kane, G. A. Ladinsky, and C. P. Yuan. "Using the Top Quark for Testing Standard Model Polarization and CP Predictions." In: *Phys. Rev. D* 45 (1992), pp. 124–141. DOI: `10.1103/PhysRevD.45.124`.

[145] V. M. Abazov et al. "Evidence for production of single top quarks and first direct measurement of |Vtb|." In: *Phys. Rev. Lett.* 98 (2007), p. 181802. DOI: `10.1103/PhysRevLett.98.181802`. arXiv: `hep-ex/0612052`.

[146] M. Aaboud et al. "Combinations of single-top-quark production cross-section measurements and $|f_{LV}V_{tb}|$ determinations at $\sqrt{s} = 7$ and 8 TeV with the ATLAS and CMS experiments." In: *JHEP* 05 (2019), p. 088. DOI: `10.1007/JHEP05(2019)088`. arXiv: `1902.07158 [hep-ex]`.

Acknowledgments

I want to thank my supervisor, Prof. Dr. Wagner, for his invaluable guidance, mentorship, and expertise. I am also grateful to the entire t-channel analysis team for their collaboration in this analysis.

My appreciation extends to my many colleagues and peers in the Wuppertal particle physics group. Their collaboration and camaraderie have greatly enriched this experience, and working alongside such talented and dedicated individuals has been a big motivation. In particular, I want to thank Oliver for teaming up with me to study physics.

I would also like to express my deepest gratitude to my family, whose unwavering support has been instrumental in enabling me to undertake this journey.